Plasma Physics Reports, Vol. 26, No. 11, 2000, pp. 917–930. Translated from Fizika Plazmy, Vol. 26, No. 11, 2000, pp. 979–992.

Investigation of the H-Mode during ECRH in the T-10 Tokamak

V. V. Alikaev, A. A. Borshchegovskiĭ, V. A. Vershkov, V. V. Volkov, A. V. Gorshkov, Yu. V. Gott, S. A. Grashin, M. M. Dremin, L. G. Eliseev, Yu. V. Esipchuk, V. A. Zhuravlev, A. M. Kakurin, G. S. Kirnev, N. A. Kirneva, A. Ya. Kislov, D. A. Kislov, I. V. Klimanov, V. A. Kochin, V. A. Krupin, S. V. Krylov, A. V. Melnikov, T. B. Myalton, A. Yu. Novikov, G. E. Notkin, Yu. D. Pavlov, V. V. Piterskiĭ, V. I. Poznyak, I. N. Roĭ, P. V. Savrukhin, V. V. Sannikov, S. V. Soldatov, M. M. Stepanenko, A. V. Sushkov, K. N. Tarasyan, V. M. Trukhin, E. V. Trukhina, L. N. Khimchenko, V. V. Chistyakov, and D. A. Shelukhin

Nuclear Fusion Institute, Russian Research Centre Kurchatov Institute, pl. Kurchatova 1, Moscow, 123182 Russia

Received March 15, 2000; in final form, May 23, 2000

Abstract—An improved confinement regime with an external transport barrier (H-mode) is obtained during electron-cyclotron resonance heating of a plasma in the T-10 tokamak. A characteristic feature of this regime is a spontaneous density growth accompanied by a drop in the intensity of D_α line and an increase in β_p by a factor of ~1.6. The threshold power for the L–H transition is close to that predicted by the ITER scaling. The best characteristics of the H-mode are achieved with decreasing q_L to 2.2. It is shown that the external transport barrier arises for electrons, whereas the heat transport barrier insignificantly contributes to improved confinement.

1. INTRODUCTION. EXPERIMENTAL CONDITIONS

During electron-cyclotron resonance heating (ECRH) in the T-10 tokamak, a regime of improved confinement was obtained (Fig. 1) with features resembling those observed in the regime with an external transport barrier (H-mode) [1].

This regime was investigated over a wide range of toroidal magnetic fields from B_T = 2.42 T (on-axis microwave power deposition) to B_T = 2.14 T [the electron-cyclotron resonance (ECR) is shifted by 19 cm toward higher magnetic fields ($\rho_{ECR} \simeq r_{ECR}/a_L = 0.65$)]. To clarify the main features of the H-mode, the plasma density was varied from $\bar{n}_e = 1.2 \times 10^{19}$ to 2.6×10^{19} m^{-3} (in the L-phase). The value of q_L varied from q_L = 2.2 to 4.1 (which corresponded to a change in the plasma current I_p from 330 to180 kA at B_T = 2.42 T). The microwave power absorbed in the plasma attained P_{ab} = 0.8 MW. Note that microwaves (second ECR harmonic, X-mode) were launched into the plasma at an angle of $\psi = 21°$ to the direction of the major radius R. All experiments were carried out with the electron-cyclotron current drive I_{CD} in the direction of the plasma current (co-CD). At high currents (I_p > 180 kA), I_{CD} comprised a small fraction of I_p, so that its influence on the processes under study was negligible.

In the experiments under discussion, the limiter radius was a_L = 30 cm.

2. MAIN FEATURES OF THE OBSERVED MODE OF IMPROVED PLASMA CONFINEMENT (H-MODE)

1. As is seen from Fig. 1, the transition to improved confinement ($t_{L–H} \simeq$ 500 ms) manifests itself as a spontaneous growth in the plasma density accompanied by a decrease in the intensity $I_{D\alpha}$ of the D_α line in various plasma cross sections, including the limiter cross section. In the best regimes, the plasma density $\bar{n}_e$ nearly doubled by the end of the microwave pulse when the gas-puffing valve in the feedback system was switched off completely. The intensity $I_{D\alpha}$ fell by a factor of 3 to 4 (Fig. 1), indicating a substantial decrease in the inward neutral flux ($\Gamma_{IN} = k_\alpha I_{D\alpha}$, where $k_\alpha \approx$ const).

Figure 2 shows the profiles of the plasma density $n_e(r)$ and its gradient grad(n_e). These data demonstrate that the density gradient increases predominantly in the region $r \geq 20$ cm. Therefore, we may conclude that an external transport barrier arises near the limiter.

2. After the L–H transition, the plasma-density growth is accompanied by an increase in the plasma energy. This is evident from Fig. 1, which shows the time behavior of the value $\beta + l_i/2$ (together with calculated values of $(l_i/2)_{calc}$ and the value of β_p derived from diamagnetic measurements).

An assessment of the improvement in the energy confinement time in the H-mode (compared to the L-mode) can be made using the data presented in the table for several pulses with nearly the same parameters (B_T = 2.42 T, I_p = 330 kA, and q_L = 2.2).

1063-780X/00/2611-0917$20.00 © 2000 MAIK "Nauka/Interperiodica"

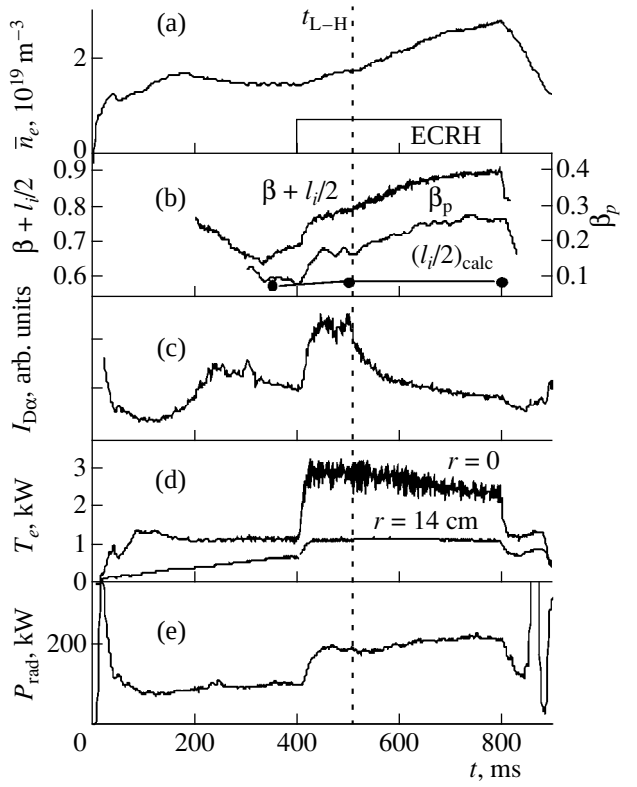

Fig. 1. Time evolutions of (a) the mean plasma density $\bar{n}_e$; (b) quantities $\beta + l_i/2$ (data from the plasma equilibrium) and β_p (diamagnetic measurements) (here and below, the scale for $(l_i/2)_{calc}$ is the same as for $\beta + l_i/2$); (c) intensity of the D_α line; (d) electron temperature T_e; and (e) radiation power P_{rad} in the regime with the L–H transition (shot no. 26 154, B_T = 2.42 T, I_p = 330 kA, q_L = 2.2, and P_{ab} = 750 kW); t_{L-H} is the instant of the L–H transition.

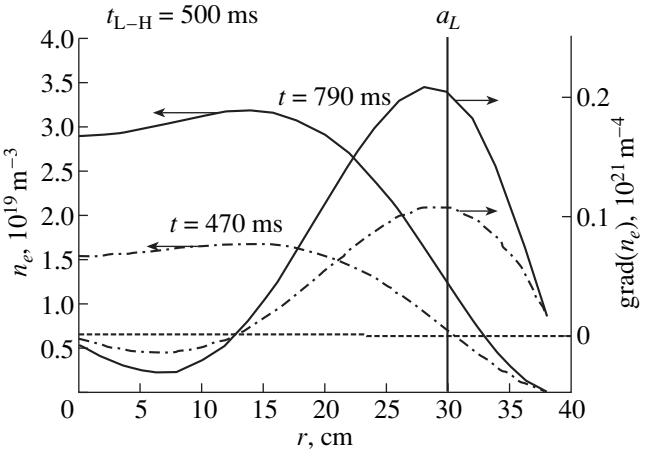

Fig. 2. Profiles of the density $n_e(r)$ and density gradient grad(n_e) in the L-phase (t = 470 ms) and at the end of the microwave pulse in the H-phase (t = 790 ms).

The values of β_p shown in the table were determined in different ways:

(i) β_{dia} was obtained from diamagnetic measurements;

(ii) β_{eq} was obtained from the data on the plasma equilibrium (with taking into account the calculated value of l_i); and

(iii) β_{kin} was obtained from the T_e, T_i, and n_e profiles.

Based on these data, we can characterize the improvement of confinement in the H-mode by the enhancement factor

$$H_L = \frac{\tau_E^H}{\tau_E^L} \simeq \frac{\beta_p^H}{\beta_p^L} \simeq 1.6 \pm 0.1.$$

As was shown in [2], the experimental value of the energy confinement time τ_E^{exp} in the L-mode regimes in the T-10 tokamak turned out to be ~30–40% lower than that predicted by the ITER-89-P scaling ($(\tau_E)_{IT-89}$), compared with the latter for $\bar{n}_e \approx 3–4 \times 10^{19}$ m^{-3}, and exceeded $(\tau_E)_{IT-89}$ at higher densities. In high-current low-density regimes (I_p = 300 kA and $\bar{n}_e \simeq 1.5 \times 10^{19}$ m^{-3}), the energy confinement time is $\tau_E^{exp} \simeq$ 12–13 ms, which is about one-half of $(\tau_E)_{IT-89}$.

3. As will be shown below (see Sections 5 and 6), the L–H transition is accompanied by the generation of an electric field in a narrow layer ($\Delta_H \simeq 2$ cm) near the limiter and by a decrease in the amplitude of turbulent fluctuations.

4. The plasma-density growth in the H-mode cannot be explained by an increase in the impurity flux into the plasma. The intensity of the C_{III} line in the limiter cross section, $I^L_{C_{III}}$, remains almost unchanged after the L–H transition. An insignificant increase in the radiation power P_{rad} (Fig. 1) in the H-phase may be explained by the increase in the plasma density.

There is no evidence of a substantial accumulation of impurities in the plasma core in the H-mode. The intensity of X-ray emission and the increase in the intensity of continuum correlate with the plasma-density growth.

3. THRESHOLD POWER FOR THE L–H TRANSITION

To determine the threshold power P_{th}^{LH} for the L–H transition, we carried out experiments in which the heating microwave power was gradually elevated in the regime with B_T = 2.42 T (on-axis heating), I_p = 330 kA (q_L = 2.2), and $\bar{n}_e = 1.5 \times 10^{19}$ m^{-3} (before the L–H transition).

The results of this series of experiments are presented in Fig. 3 as the dependence of the enhancement

Table

Shot no.	L-phase			H-phase			$H_L = \beta^H/\beta^L$		
	β_{eq}	β_{dia}	β_{kin}	β_{eq}	β_{dia}	β_{kin}	eq	dia	kin
26154	0.200	0.167	0.168	0.310	0.267	0.267	1.55	1.59	1.60
26308	0.160	0.149	0.168	0.266	0.250	0.273	1.66	1.62	1.68
26319	0.160	–	–	0.260	–	–	1.63	–	–
26321	0.167	0.158	0.14	0.260	0.247	0.281	1.56	1.56	2
26322	0.170	0.172	–	0.270	0.265	–	1.59	1.54	–

factor $H_L = \beta_p^H/\beta_p^L$ on the total heating power $P_{tot} = P_{ab} + P_{OH}$, where P_{OH} is the Ohmic heating power. As P_{tot} decreases, the value of H_L drops, approaching unity near $P_{tot} = P_{th}^{LH} \simeq 600$ kW. Thus, in typical regimes with the maximum ECRH power, P_{tot} exceeds the threshold power P_{th}^{LH} by ~70%. The threshold power $P_{th}^{LH} = 600$ kW is close to that predicted by the ITER scaling [3]:

$$P_{th}^{ITER} = 2.84\ \mathrm{M}^{-1}\ B_T^{0.82} n_e^{0.58} R a^{0.81},$$

where B_T is expressed in T; a and R, in m; and n_e, in units of 10^{20} m^{-3}.

In these estimates, the radiation power P_{rad} (which is ~170 kW in the regimes under discussion) was not taken into account, because the radial profile of P_{rad} was not measured in the T-10 tokamak. We believe that accurately taking P_{rad} into account might only slightly decrease the threshold power for the L–H transition in T-10.

4. DOMAIN OF EXISTENCE OF THE H-MODE (GENERAL FEATURES)

4.1. Dependence on q_L

It is seen from Fig. 4 that, for on-axis heating (B_T = 2.42 T), the H-mode is observed over a wide range of plasma currents I_p (i.e., q_L). As I_p decreases (q_L increases), the enhancement factor H_L in the H-mode falls and, for $q_L > 4$ ($I_p \le 180$ kA), the L–H transition does not occur.

We note that a similar tendency (Fig. 4) toward the improvement of plasma confinement in the H-mode (i.e., an increase in the factor H_L with decreasing q_L) was also observed for off-axis heating (B_T = 2.14 T). In this case, the largest value of H_L was also attained at low values of the safety factor (at $q_L \approx 2$, other parameters being the same).

These results should be regarded not as an enhanced (in comparison with the L-mode) dependence of τ_E on I_p in the H-mode but as the fact that the threshold power P_{th}^{LH} increases as q_L increases. Such a dependence was not observed in other devices (the ITER scaling for P_{th}^{LH} does not contain any dependence on q_L). Apparently, this may be explained as a specific feature of T-10 regimes: the rate of effective electron transport at the edge is proportional to the safety factor squared ($(\chi_l)_{eff} \sim q^2$), which leads to a narrowing of the T_e profile; a decrease in the temperature gradient ∇T_e at the edge; and, as a consequence, an increase in P_{th}^{LH} with increasing q_L.

4.2. Dependence on the Density

It follows from Fig. 5 that, as the plasma density $\bar{n}_e$ increases, the factor H_L characterizing the increase in the energy confinement time τ_E in the H-mode decreases.

In the main regime with $q_L = 2.2$ (I_p = 330 kA) and B_T = 2.42 T, the L–H transition is no longer observed for $\bar{n}_e \ge 3.4 \times 10^{19}$ m^{-3} (Fig. 5). The fact that the L–H transition disappears as the density increases may apparently be explained by the increase in the threshold

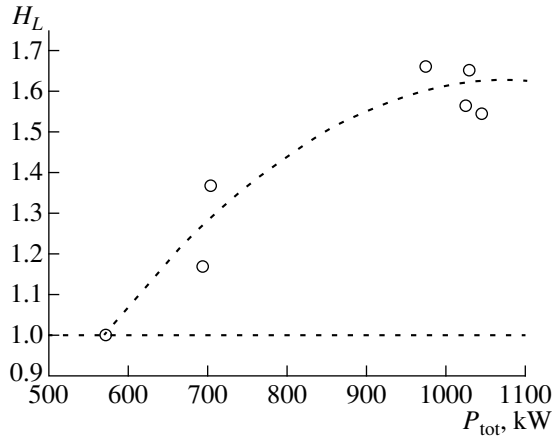

Fig. 3. Dependence of the enhancement factor H_L on the total heating power P_{tot}.

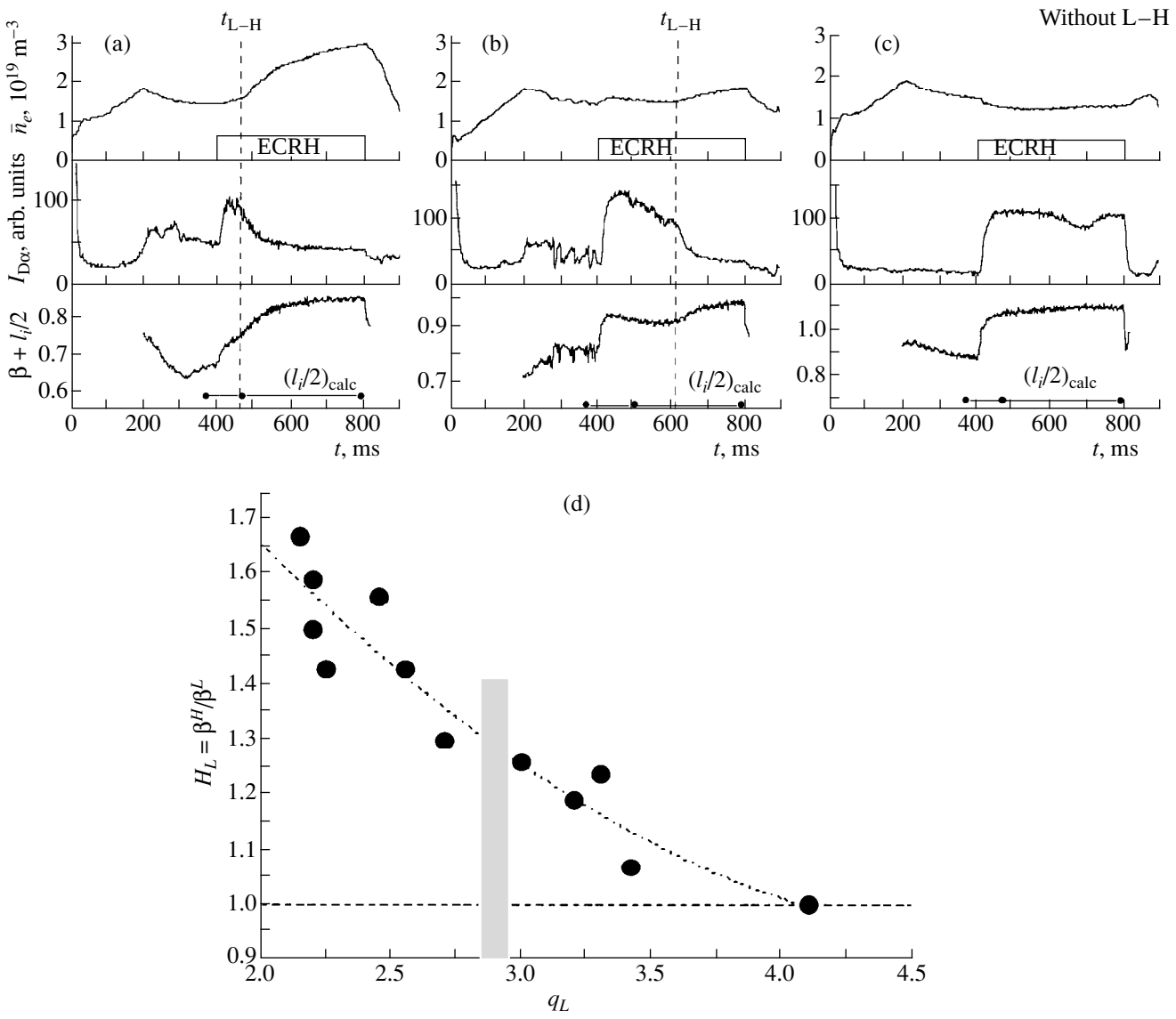

Fig. 4. Variations in the characteristics of the H-mode (the increase in $\bar{n}_e$ and β_p and the decrease in $I_{D\alpha}$) with increasing q_L for B_T = 2.42 T and P_{ab} = 750 kW: (a) q_L = 2.2 (shot no. 26 308, I_p = 330 kA), (b) q_L = 3 (shot no. 26 311, I_p = 240 kA), and (c) q_L = 4.1 (shot no. 26 314, I_p = 180 kA). (d) The enhancement factor H_L as a function of q_L.

power P_{th}^{LH} for the L–H transition. Indeed, according to the ITER scaling, we have $P_{th}^{LH} \sim n^{0.58}$. Since, in the initial regime (in the L-phase), the density is equal to $\bar{n}_e \simeq 1.4\text{–}1.5 \times 10^{19}$ m^{-3} and the total heating power P_{tot} exceeds the threshold power P_{th}^{LH} by nearly 70%, we can expect that, according to the scaling, the L–H transition should disappear at the plasma density $n_{th} \sim 1.5 \times 10^{19} \times (1.7)^{1/0.58} \simeq 3.6 \times 10^{19}$ m^{-3}, which is close to the experimentally observed limit.

Hence, the data obtained in T-10 are consistent with the prediction that P_{th}^{LH} should grow with increasing plasma density.

The data presented in Figs. 6 and 7 provide additional information on the features of the H-mode in the T-10 tokamak. As was noted above, the main feature is the fact that the plasma density $\bar{n}_e$ continues to grow when the gas-puffing valve is switched off completely and the intensity $I_{D\alpha}$ (i.e., the neutral flux into the plasma) decreases. In the main regime (B_T = 2.42 T, I_p = 330 kA), the plasma density $\bar{n}_e$ in the H-mode nearly doubles by the end of the microwave pulse, reaching $\bar{n}_e = 3 \times 10^{19}$ m^{-3}.

For the ECRH experiments in T-10 [4], the characteristic feature of the L-mode is that the energy confinement time grows with increasing plasma density.

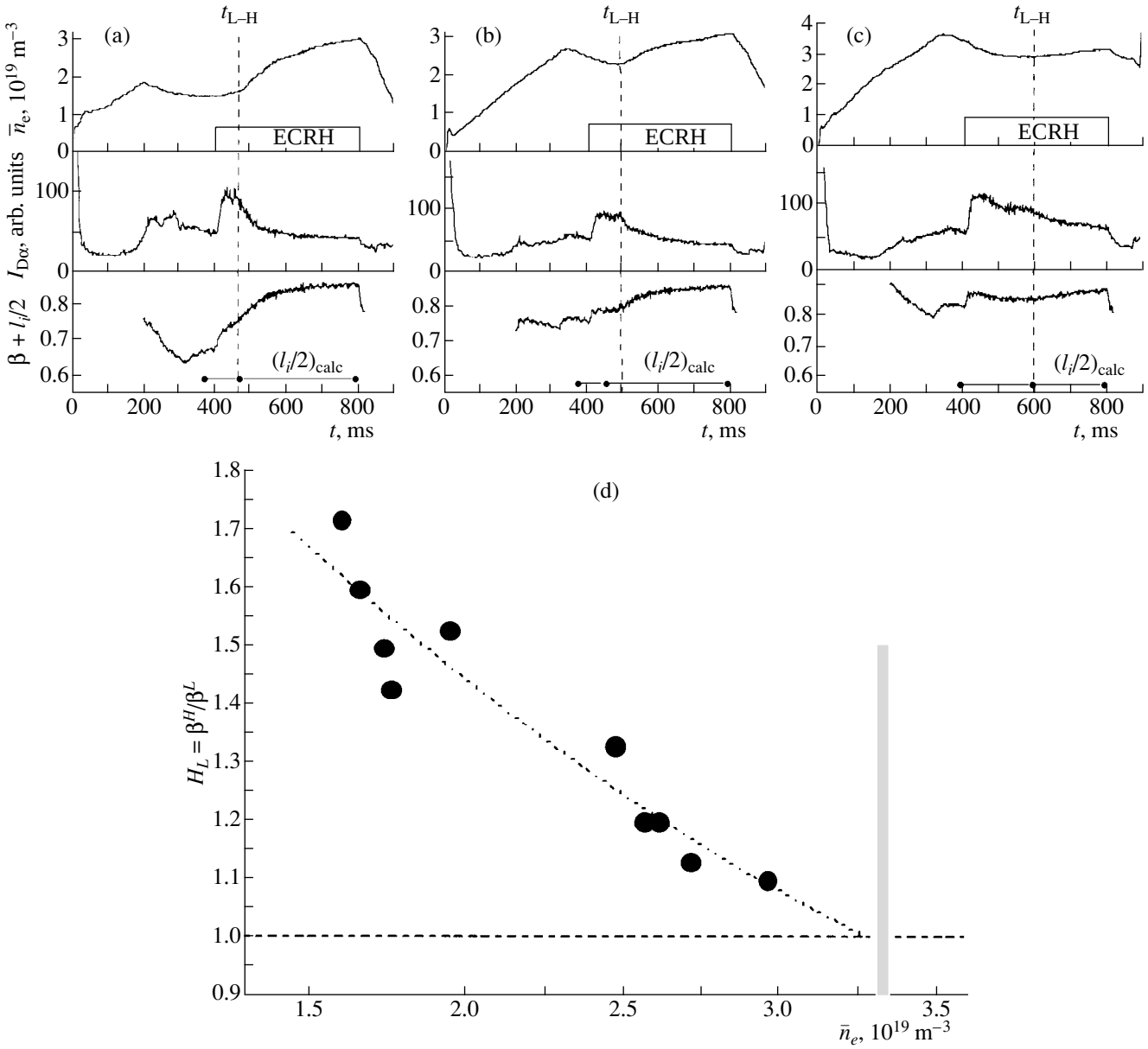

Fig. 5. (a–c) Variations in the characteristics of the H-mode with increasing plasma density (shot nos. 26308, 26324, and 26326) for B_T = 2.42 T, q_L = 2.2 (I_p = 330 kA), and P_{ab} = 750 kW. (d) The enhancement factor H_L as a function of the plasma density.

It is seen from Fig. 6 that, if we increase the plasma density to the same level (3×10^{19} m^{-3}) as is attained in the H-mode by the end of the microwave pulse, then the value of β_p and the energy confinement time τ_E in the L-mode turn out to be close to those in the H-mode (the values of P_{tot} in both cases are nearly the same).

Figure 7 shows the time dependences of the electron temperature T_e (the second harmonic of electron-cyclotron emission) at different radii. It is seen that the electron temperature increases insignificantly during the L–H transition.

Hence, the transport barrier observed experimentally in the H-mode is a barrier for particles, whereas the thermal barrier, which is identified by an increase in T_e, is low and insignificantly contributes to the increase in the plasma energy in the H-mode. This is also confirmed by the results from modeling the external barrier in the H-mode (see Section 8).

4.3. Dependence on the Magnetic Field B_T

In T-10, an L–H transition was observed throughout the entire investigated range of B_T from 2.42 T, when microwave power was absorbed in the center of the plasma, up to B_T = 2.14 T, when the absorption region

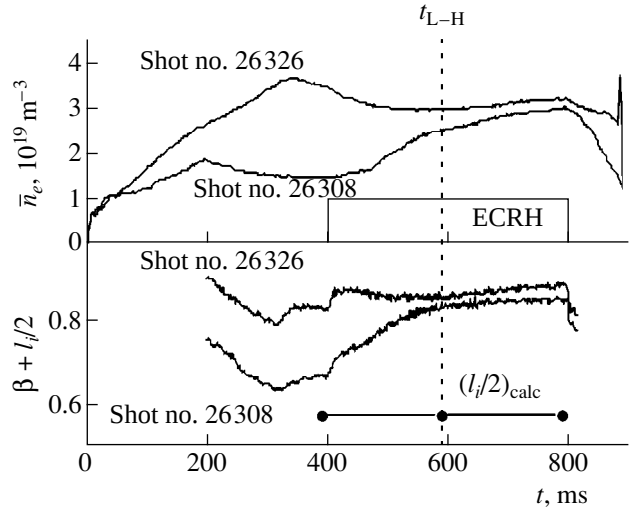

Fig. 6. Comparison of the $\beta + l_i/2$ value in the L- and H-modes for the same plasma density (t_{L-H} is the instant of the L–H transition in shot no. 26 326).

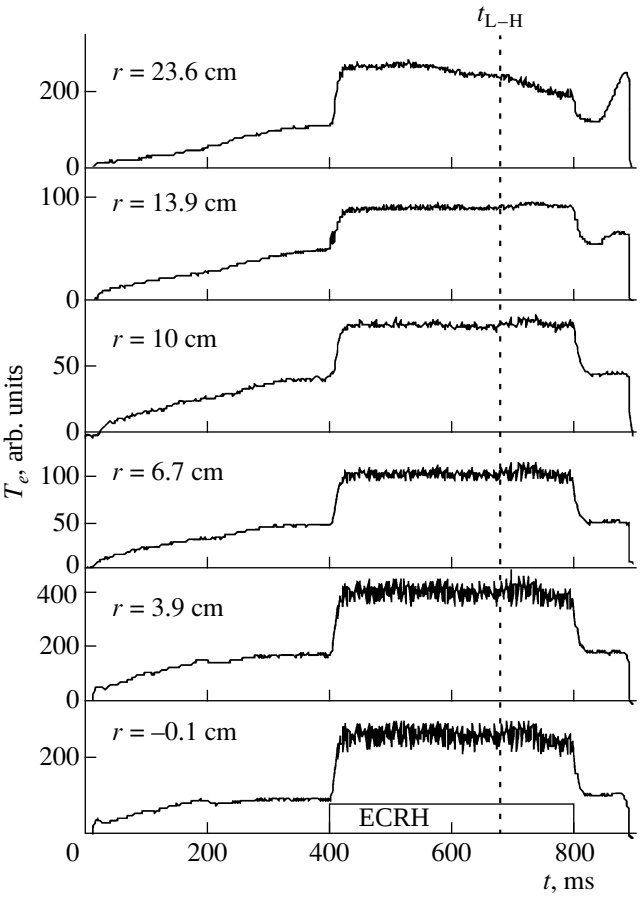

Fig. 7. Time evolution of the electron temperature T_e after the transition to the H-mode (shot no. 26034, B_T = 2.42 T, q_L = 2.34, I_p = 310 kA, and P_{ab} = 750 kW).

was shifted by ~18–19 cm toward higher magnetic fields ($\rho_{ECR} \simeq 0.65$).

Figure 8 illustrates the time dependences of the plasma density $\bar{n}_e$, the value of $\beta_p + l_i/2$ (together with the calculated values of $(l_i/2)_{calc}$), and the intensity of D_α emission. It is seen that the main features of the H-mode (such as spontaneous density growth, the drop in $I_{D\alpha}$, and the increase in the plasma energy) vary only slightly even though there is a substantial difference in the values of B_T. Both the density and β increments vary slightly as B_T varies.

As was expected (see Fig. 8d), the strong shift of the ECR region (B_T = 2.14 T) leads to a small change in the plasma energy after the microwave power is switched on. Therefore, in this case of off-axis heating, the plasma energy and, consequently, the energy confinement time τ_E in the H-mode are markedly lower than those for on-axis heating (B_T = 2.42 T).

The effect of B_T variations is most pronounced in the behavior of the electron temperature.

As is seen from Fig. 9 (cf. Fig. 7), the increase in T_e in the region $r/a \le 0.65$ after the L–H transition in the case of off-axis heating (B_T = 2.14 T) is more pronounced than for on-axis heating (B_T = 2.42 T). In addition, in the case of off-axis heating, the electron temperature in the H-mode does not decrease with increasing density. In contrast, as the power-deposition region shifts closer to the center of the plasma, the decrease in T_e due to the density growth becomes more pronounced.

Presumably, the fact that the decrease in the increment of the temperature T_e becomes smaller as the ECR region approaches the plasma axis is related to the increase in the power P_{ei} transferred from electrons to ions. This is evidenced by the following experimental results:

(i) In the case of on-axis heating in the steady-state phase of the H-mode, the central ion temperature $T_i(0)$ is significantly higher than that for off-axis heating: $T_i(0)$ = 550 eV at B_T = 2.42 T (on-axis heating) in comparison with $T_i(0)$ = 420 eV at B_T = 2.14 T (off-axis heating).

(ii) In the regimes with on-axis heating in which the increase in the density is lower, the temperature T_e after the L–H transition slightly increases.

In [5], it is asserted that, in the case of off-axis heating ($B_T \le 2.14$ T), an internal transport barrier (ITB) arises near the microwave absorption region in the H-mode; as a result, the T_e increment in these regimes is larger than that for on-axis heating. However, as is seen from Fig. 8, the contribution from the ITB to the global improvement of confinement in the H-mode is insignificant if we also take into account the dependence of the energy confinement time on the plasma density.

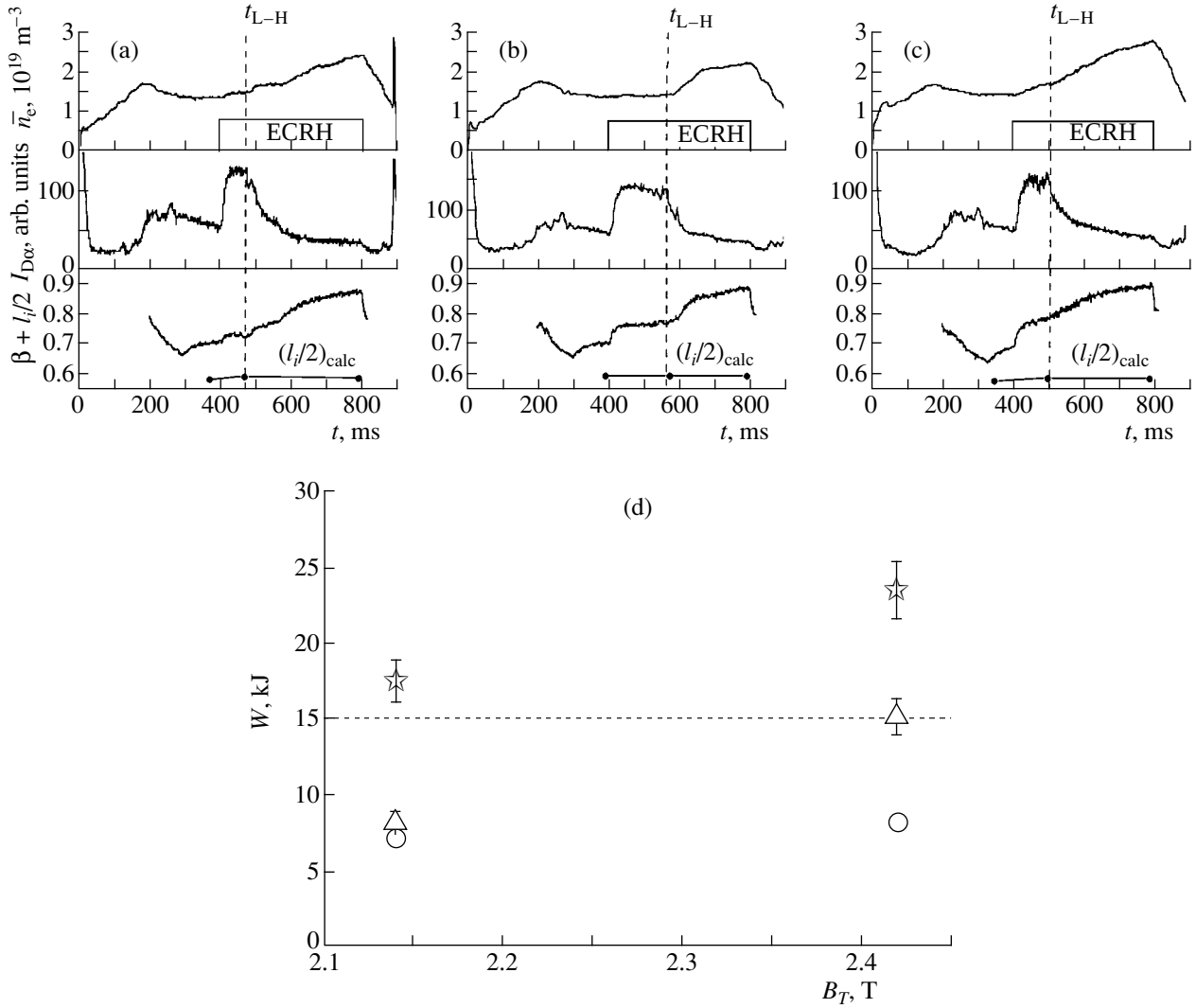

Fig. 8. Variations in the characteristics of the H-mode with increasing B_T: (a) shot no. 26 150, B_T = 2.14 T; (b) shot no. 26 031, B_T = 2.21 T; and (c) shot no. 26 154, B_T = 2.42 T. (d) A comparison of the stored plasma energy W in the regimes with on-axis (B_T = 2.42 T) and off-axis (B_T = 2.14 T) heating in the Ohmic phase (circles), L-phase (triangles), and H-mode (asterisks) for q_L = 2.2 and P_{ab} = 750 kW.

5. MEASUREMENTS OF THE RADIAL ELECTRIC FIELD IN REGIMES WITH THE L–H TRANSITION

The plasma potential and, consequently, the radial electric field E_r in the outer ($r/a > 0.65$) region of the plasma column were measured with a heavy-ion beam probe diagnostic using a 170-keV Tl beam [6].

The results of the measurements of the plasma potential $\Delta\varphi$ are presented in Fig. 10 for the case of on-axis heating (B_T = 2.42 T). The time dependences of $I_{D\alpha}$, $\bar{n}_e$, and $\Delta\varphi$ at the radius $r(\varphi_{min})/a \simeq 0.95$ corresponding to the minimum potential φ_{min} (see Fig. 10b) are shown in Fig. 10a. Figure 10b shows the $\Delta\varphi(r)$ profiles for the instants indicated in Fig. 10a.

We note that the quantity $\Delta\varphi$ presented in Fig. 10 is defined with respect to the "base" plasma potential φ_B^L in the L-phase of the discharge ($\Delta\varphi = \varphi - \varphi_B^L$). The time interval in which the base potential φ_B^L was determined is also shown in the figure. Thus, the presented data characterize the variations in the potential (and, consequently, in the radial electric field $E_r = -\text{grad}(\varphi)$ relative to its value in the L-phase of the discharge). Figure 11 also shows the variations in $\Delta\varphi$ (at $r = r(\varphi_{min})$), including the earlier stage of the discharge before switching on the heating microwave pulse.

The characteristic features of the behavior of the electric field in the H-mode discharges are the following:

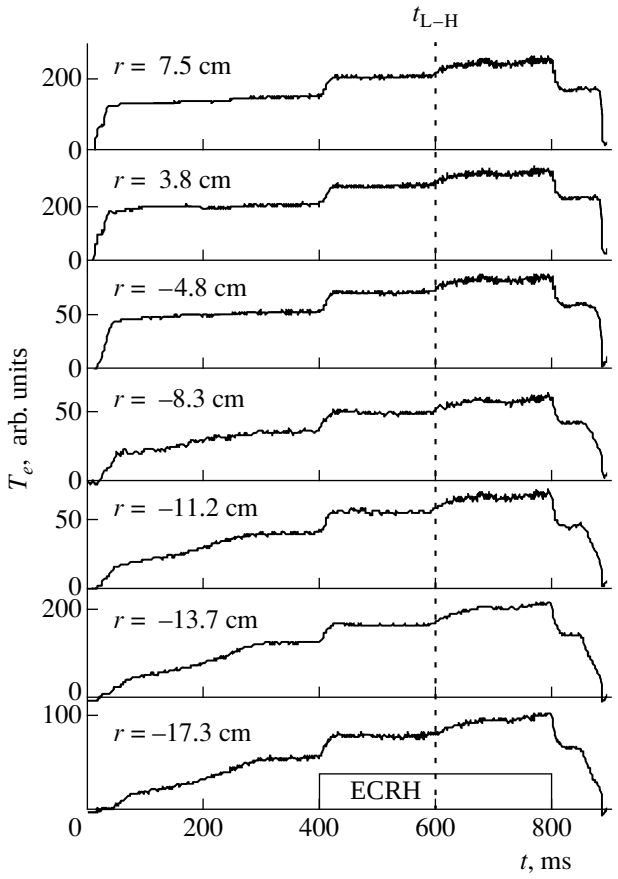

Fig. 9. Time evolution of the electron temperature T_e in the H-mode in the case of off-axis heating (shot no. 26019, B_T = 2.14 T, q_L = 2.2, I_p = 293 kA).

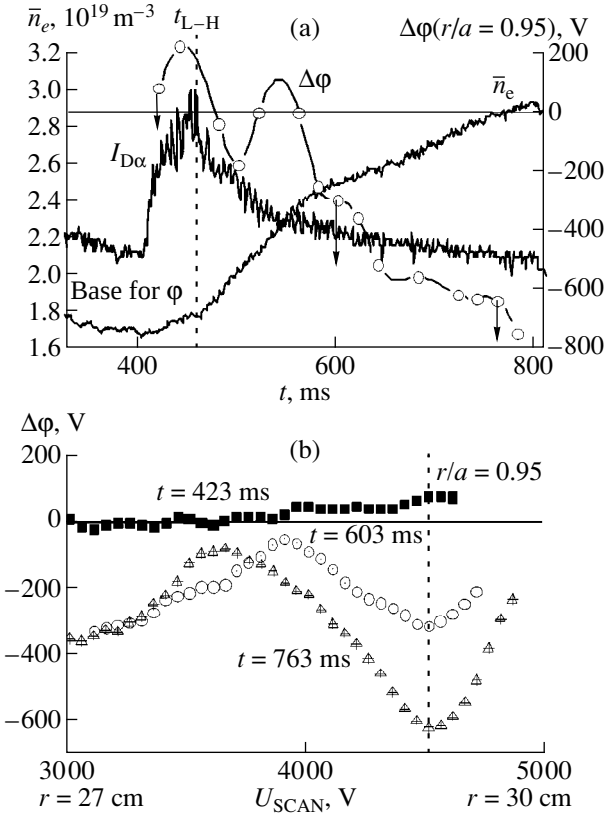

Fig. 10. Results from measurements of the plasma potential Δφ in the H-mode (B_T = 2.42 T, q_L = 2.2, I_p = 330 kA, and P_{ab} = 750 kW): (a) time evolution of Δφ for $r(\varphi_{min})$ and (b) radial profiles of Δφ for the instants indicated by the arrows in plot (a). The interval for determining the base value of the potential φ_B^L is also shown in plot (a).

(i) During the L–H transition, the radial electric field is generated in a narrow region ($\Delta r \simeq$ 1.5–2 cm) adjacent to the limiter.

(ii) After the microwave pulse is switched on, a positive (i.e., directed outward) electric field E_r is generated in this region. This indicates that, in the L-phase, the ratio $\langle v_e \rangle_\perp / \langle v_i \rangle_\perp$ between the transverse (diffusion) velocities of electrons and ions at the plasma edge increases with respect to the Ohmic phase of the discharge.

(iii) During the L–H transition, the field E_r changes its sign and becomes negative (directed inward). However, during the L–H transition, this negative field is low compared to its maximum value reached before the end of the microwave pulse, when the H-mode is nearly steady-state.

(iv) After the L–H transition, the negative radial field E_r increases in magnitude with a characteristic time close to that for the intensity $I_{D\alpha}$ and reaches its maximum ($E_r \simeq$ –(400–500) V/cm) when the H-mode is near its steady state (i.e., the density and β_p are nearly maximum).

Note that, as is seen from Fig. 10b, the potential profile has the shape of a well. This means that, along with the negative field considered above, a positive field E_r is generated on the inner side of the barrier. However, the role of this field and its influence on the features of the H-mode are still unknown and will be the subject of further investigations of the H-mode in T-10.

6. CHANGE IN THE PLASMA TURBULENCE DURING THE L–H TRANSITION

The measurements of plasma turbulence were primarily carried out with a two-frequency reflectometer [7]; the frequency was varied in the range f = 26.4–36 GHz, which corresponded to the variations in the plasma density in the reflection layer in the range n_e = (0.85–1.6) × 10^{19} m^{-3}. In addition, oscillations in the frequency range f = 2–6 GHz were measured with the help of a loop placed outside the limiter and with an

X-ray diagnostics detecting fluctuations in the frequency range $f \le 50$ kHz.

Figure 12 shows the reflectometer signals for two probing frequencies (indicated in figure) in the regime with $B_T = 2.42$ T, $I = 330$ kA ($q_L = 2.2$), and $\bar{n}_e \simeq 1.6 \times 10^{19}$ m^{-3} (shot no. 26308). The figure also shows the time dependences of the reflection-layer radius r_{ref} for both probing frequencies.

The general features of the phenomena observed can be described as follows.

(i) In the frequency range $f < 100$ kHz, in which the amplitude of turbulent fluctuations was maximum (see Fig. 12), the fluctuation amplitude did not decrease during the L–H transition (in some shots, the amplitude even increased). However, more detailed studies showed that, during the L–H transition, coherent turbulent fluctuations at frequencies $f \simeq 100$ kHz were substantially suppressed.

(ii) As is seen from Fig. 12, the amplitude of turbulent fluctuations decreased in the range of higher frequencies $f > 200$ kHz. The amplitude of fluctuations began to fall after the L–H transition, when the radius r_{ref} of the reflection layer increased (due to the increase in the plasma density at the edge) to $r_{\mathrm{ref}} \simeq 27$–$28$ cm. In the subsequent phase of the H-mode, the radius r_{ref} varied more slightly, remaining in the range $27 < r_{\mathrm{ref}} < 30$ cm, and the level of turbulent fluctuations did not change.

An analysis of the results of these experiments showed that a radius of 27.5 cm may be regarded as a boundary of the transport barrier arising during the L–H transition (see also Section 5).

(iii) At higher values of the initial plasma density, when the radius r_{ref} was larger and the reflection layer was in the region $r \ge 27$ cm even before the L–H transition, the decrease in the amplitude of turbulent fluctuations occurred earlier (at the instant of the L–H transition).

However, we did not observe a rapid suppression of turbulence during the L–H transition. The characteristic decay time of turbulent fluctuations was equal to ~100 ms.

(iv) When the reflectometer probing frequency was increased so that, even for the maximum density at the end of the H-mode, the radius r_{ref} of the reflection layer did not attain 27 cm, no change was observed in the level of turbulence at frequencies $f > 100$ kHz.

(v) The X-ray signals did not exhibit noticeable variations in the turbulence level at frequencies $f < 50$ kHz during the L–H transition.

On the other hand, the amplitude A_{HF} of the signal from a high-frequency probe measuring fluctuations of the electric and magnetic fields near the limiter grew substantially (by a factor of 3 to 4) during the microwave pulse. At the instant of the L–H transition, the amplitude began to fall with a characteristic time close to that for the intensity of D_α emission (Fig. 13).

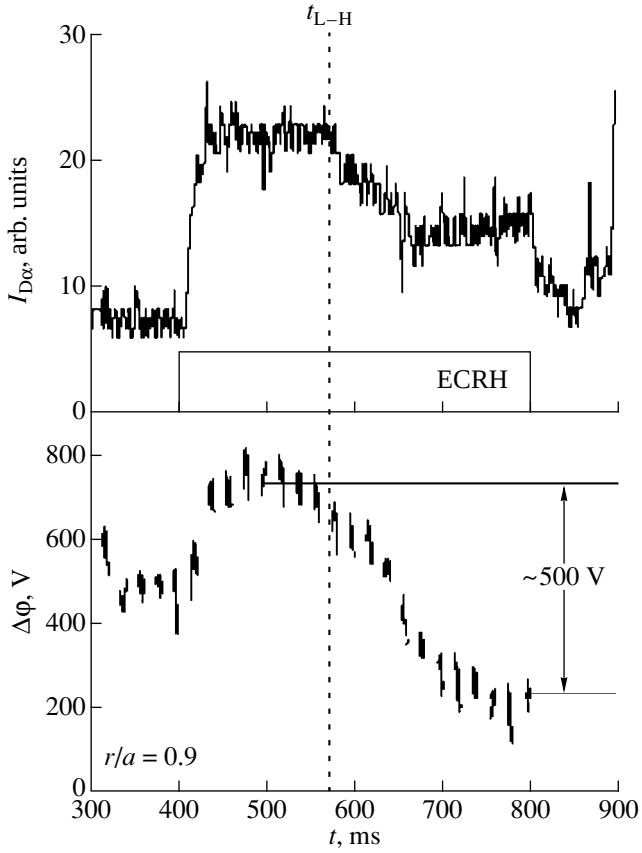

Fig. 11. Time evolution of the plasma potential $\Delta\varphi$ after switching on the microwave pulse and during the L–H transition (shot no. 23779). The base value φ_B is measured in the Ohmic phase of the discharge. The time evolution of $I_{D\alpha}$ is also shown.

7. FEATURES OF PROCESSES IN THE SCRAPE-OFF LAYER REGION DURING THE L–H TRANSITION

In the investigated regimes, we also measured the parameters of the edge plasma. For this purpose, we used Langmuir probes located in the scrape-off layer (SOL) ($r_p \sim 33$–34.5 cm) and at the limiter ($a_L = 30$ cm).

In the main regimes, the electron temperature T_e, the ion saturation current at the probe Γ_i, and the probe potential inside the SOL ($r = 34$ cm) change abruptly at the instant of the L–H transition (see Fig. 13a). In these regimes, the characteristic time of variations in the above parameters is equal to 5–10 ms. Since the signals from the probes located at the limiter vary slightly during the L–H transition, the drop in the signals from the probes located in the SOL indicates that the decay length λ of T_e and n_e in the SOL decreases during the

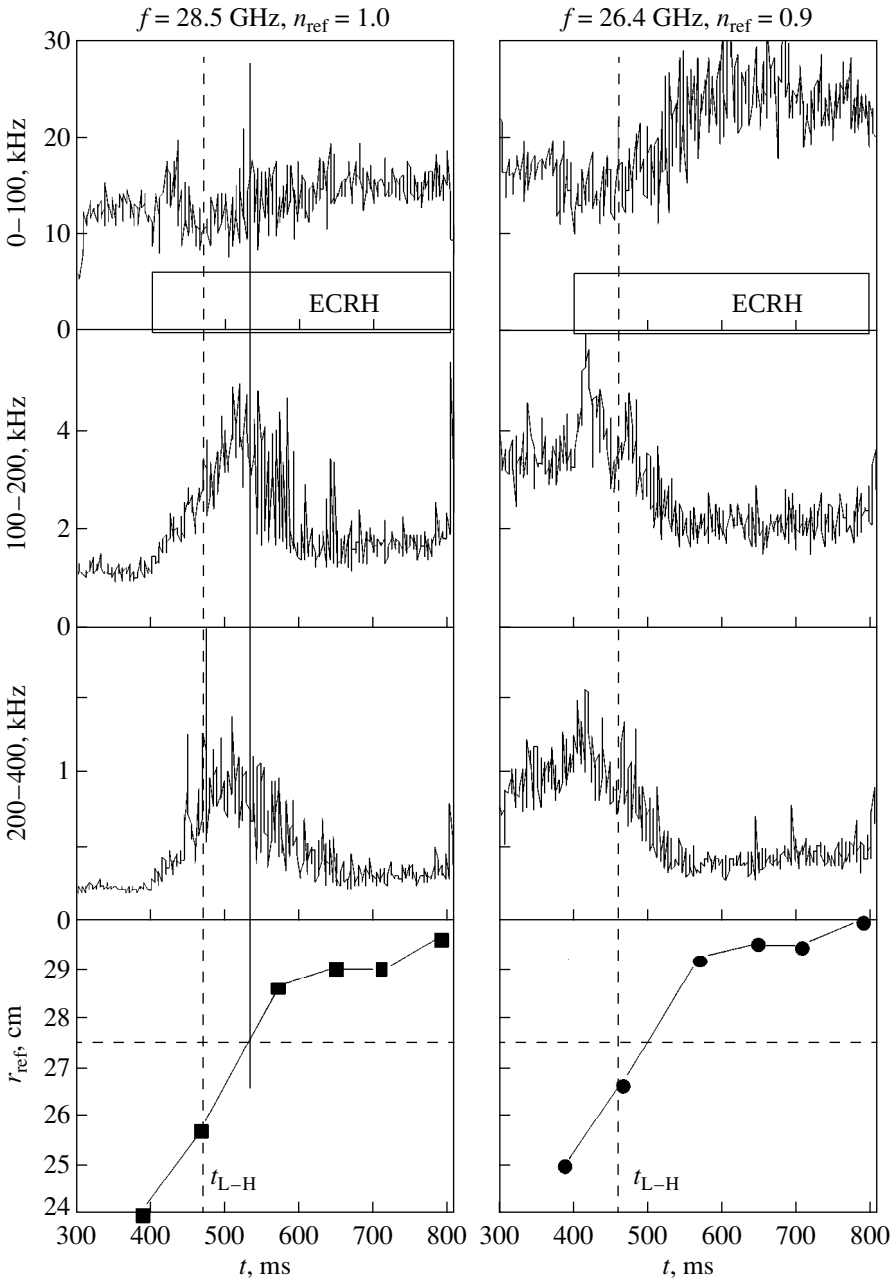

Fig. 12. Results of measurements of plasma turbulence by a reflectometer and time variations in the reflecting-layer radius (shot no. 26308, B_T = 2.42 T, q_L = 2.2, I_p = 330 kA, and P_{ab} = 750 kW).

transition (i.e., the transverse diffusion velocity $\langle v \rangle_\perp$ decreases). The effect is illustrated in Fig. 13c.

8. RESULTS OF SIMULATION OF THE EXTERNAL TRANSPORT BARRIER

To estimate the depth of the transport barrier arising during the L–H transition and its time variations in the course of the evolution of the H-mode, we carried out numerical simulations of the main regime with B_T = 2.42 T and q_L = 2.2 (Fig. 1).

By the transport-barrier depth, we mean the ratio of the diffusion coefficients D (in the region where the barrier exists) in the absence and presence of the barrier.

The main features of the model are the following.

(i) For simulations, we used a transport model of canonical profiles [8] with the additional condition that $T_e(r)$ and $n_e(r)$ fit, as closely as possible, the experimental profiles in both the Ohmic phase and L-phase of the discharge.

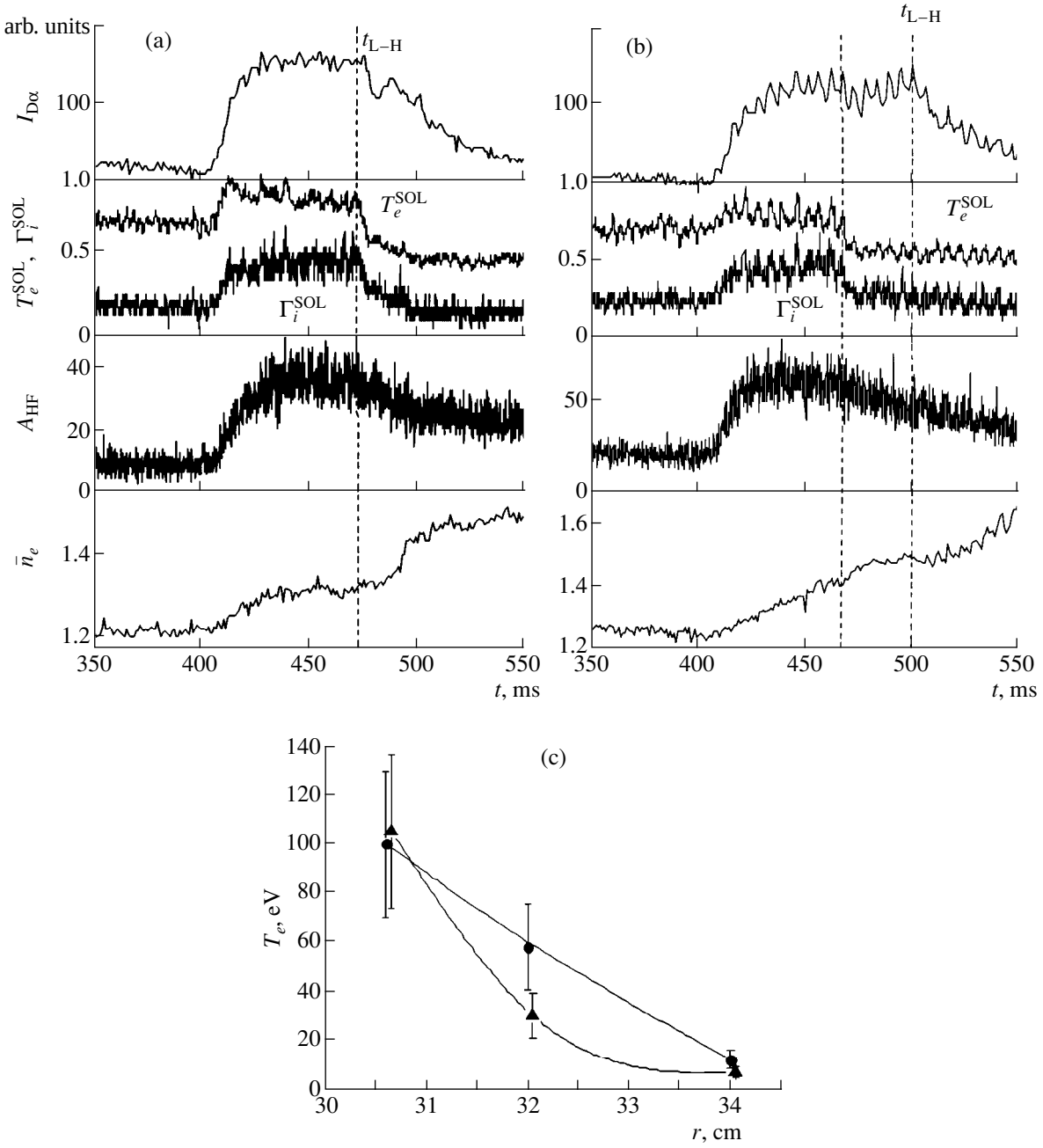

Fig. 13. (a, b) Time evolutions of the temperature T_e, saturation ion current Γ_i in the SOL, $I_{D\alpha}$, $\bar{n}_e$, and microwave-probe signal A_{HF} at $f = 2$ GHz for (a) $B_T = 2.14$ T (shot no. 26150) and (b) $B_T = 2.42$ T (shot no. 26154). (c) Variations in the scale length λ_{Te} of the temperature drop in the SOL during the L–H transition (shot no. 26191, $B_T = 2.16$ T, $I_p = 285$ kA, $q_L = 2.27$ at (●) 440 and (▲) 580 ms; the L–H transition occurs at the instant $t_{L-H} = 495$ ms.

(ii) We took into account that the flux of the working gas into the plasma after the L–H transition decreased according to the relationship

$$\Gamma_{IN} = k_\alpha I_{D\alpha} (k_\alpha = \text{const}),$$

where Γ_{IN} is the neutral flux into the plasma and $I_{D\alpha}$ is the intensity of the D_α line. The factor k_α was determined in the L-phase of the discharge from the condition that the calculated mean density $\bar{n}_e^{calc}$ should coincide with the experimental value.

(iii) The depth of the transport barrier and its time evolution were chosen from the condition that the calculated functions $n_e(r, t)$ and $\beta(r, t)$ should coincide

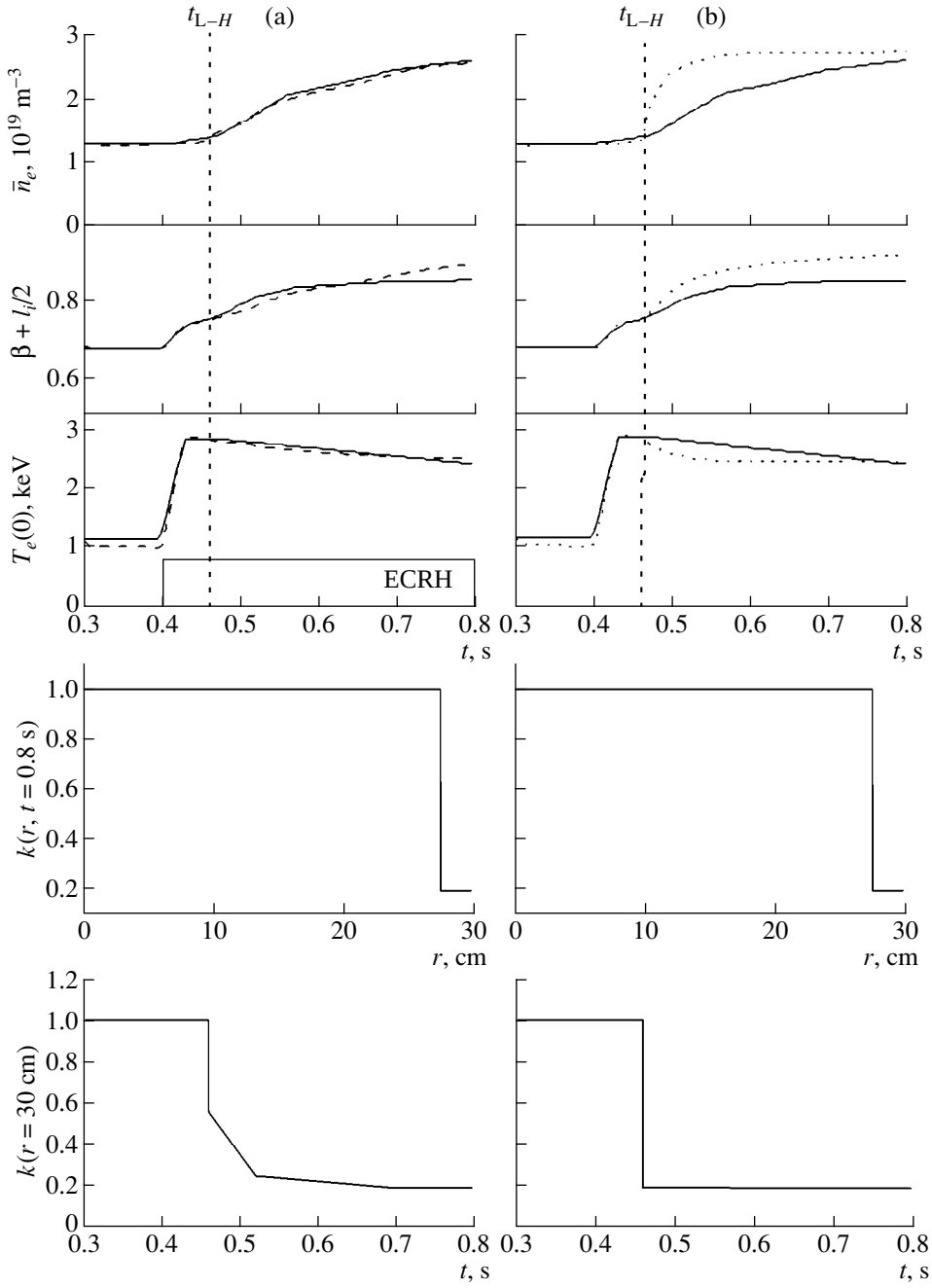

Fig. 14. Results of modeling the regime with an external transport barrier. The solid lines correspond to the experiment, and the dashed lines show the modeling results. The coefficient k characterizing the transport barrier (the barrier depth is equal to $1/k$) satisfies the condition $D^H_{\text{eff}}(r,t) = k(r,t)\ D^L_{\text{eff}}(r)$, where D^L_{eff} and D^H_{eff} are the effective diffusivities in the L- and H-phases, respectively. Columns (a) and (b) refer to different assumptions on the time evolution of the barrier depth adopted in calculations (see the text).

with the experimental dependences. According to the data presented in Section 6, the barrier width was assumed to be equal to $\Delta r_H = 2.5$ cm.

The results of simulations (see Fig. 14) show that the model correctly describes the experimentally observed increase in the density and plasma energy in the H-mode if we strongly reduce the rate of transverse transport of particles to about one-fifth of its initial level in the L-mode. The results of calculations confirm that the decrease in the thermal diffusivity in the transport barrier is substantially less than a decrease in the diffusivity.

To bring into coincidence the calculated and experimental time dependences of $\bar{n}_e$ and β, it is necessary

to take into account that the transport barrier arising at the instant of the L–H transition initially has a small depth; then, the depth increases with a characteristic time close to that for the intensity of D_α emission (Fig. 14a).

Note that, if we assume that the transport barrier has a large depth at the instant of the L–H transition and this depth further remains constant, then the plasma density $\bar{n}_e$ and β grow much more rapidly than observed in the experiment (Fig. 14b).

9. DISCUSSION

1. Frequently, in order to explain the L–H transition, it is assumed that an increase in both the ion-pressure gradient ∇p_i and the transverse velocity $v_\perp$ gives rise to the radial electric field E_r, which produces the velocity shear $E_r B_\varphi$ that is higher than the growth rate of turbulent fluctuations γ. This means that, by the instant of the L–H transition, the following condition is satisfied:

$$\frac{1}{r}\frac{d}{dr}E_r B_\varphi > \gamma. \quad (1)$$

Condition (1) means that turbulence cannot grow (i.e., it is suppressed) and a transport barrier should form at the instant of the L–H transition. However, the results of T-10 experiments described in the preceding sections, such as (i) a fairly long time during which turbulence is suppressed, (ii) a low (as compared to maximum) value of E_r at the instant of the L–H transition and the subsequent substantial growth of E_r as the H-mode approaches its steady state, and (iii) the formation of a transport barrier during the L–H transition with a depth nearly one-half less than the steady-state value, contradict the above assumptions.

Apparently, the data from T-10 experiments agree better with the theoretical predictions formulated in [9, 10].

2. In order to compare the T-10 data with the predictions of [9, 10], we first examine how the plasma parameters change when the microwave pulse is applied.

The input of microwave power has the following effects on the plasma:

(i) both the energy and particle confinement times decrease (the density profile flattens);

(ii) the neutral flux Γ_{IN} into the plasma increases;

(iii) the amplitude of turbulent fluctuations grows; and

(iv) ∇T_e increases (in particular, at the plasma edge).

At the same time, based on the results of T-10 experiments, it was shown in [11] that, at high (>1 MW) levels of the microwave power, variations in the ion temperature can be explained by variations in the power P_{ei} transferred from electrons to ions by Coulomb collisions. This means that the input of microwave power into a plasma is not accompanied by any additional (in comparison with an Ohmically heated plasma) turbulent mechanism governing ion transport.

This allows us to suggest that, in the T-10 plasma, the switching-on of the microwave power enhances electron turbulence, which causes the enhanced transport of electrons. According to [11], the ratio $\langle v_e\rangle_\perp/\langle v_i\rangle_\perp$ between the transverse velocities of electrons and ions increases in this case. Actually, as was shown in Section 5, this leads to the generation of a positive (outward directed) radial electric field E_r.

3. According to the theory [9, 10], the increase in the turbulence level and transverse electron flux $\Gamma_\perp$ leads to the generation of the poloidal velocity $\langle v_p\rangle$ producing a stabilizing effect on turbulence. As the poloidal velocity attains a certain threshold value $\langle v_p\rangle_{\text{th}}$, the stabilizing action of $\langle v_p\rangle$ becomes dominant; as a result, both the turbulence level and turbulence-driven transverse flux decrease. This phenomenon is referred to as the L–H transition. The value $\langle v_p\rangle_{\text{th}}$ can be related to the threshold power P_{th}^{LH} for the L–H transition, because the input power P_{HF} is, in fact, a source that provides the increase in both the turbulence level and transverse transport.

According to [9, 10], the poloidal velocity $\langle v_p\rangle$ is generated at the plasma periphery due to the temperature and density gradients, which does not contradict the above conclusion about the role of ∇T_e (see Section 4).

Finally, according to [9, 10], after the transition to the H-mode, turbulence is not suppressed completely, which is also consistent with the experimental observations in T-10 (see Section 6).

Thus, based on the above considerations, it may be suggested that electron turbulence arising during the microwave-power input triggers the L–H transition in T-10 through the generation of the transverse flux $\Gamma_\perp$ and the stabilizing poloidal velocity $\langle v_p\rangle$.

4. As was said above, the edge electric field E_r, which is initially positive, changes its sign during the L–H transition. Consequently, the ratio of the transverse transport velocities $\langle v_e\rangle_\perp/\langle v_i\rangle_\perp$ becomes less than unity. In view of [11], this suggests that, at the instant of the L–H transition, the turbulence responsible for electron transport becomes suppressed and the transport barrier for electrons arises. This assumption is consistent with the data indicating a shorter decay length of T_e in the SOL (see Section 7).

However, both the value of the negative electric field E_r and (according to the simulation results) the transport-barrier depth are still far from the values that are reached when the steady-state conditions are approached.

The question arises as to why the electric field E_r increases as the H-mode develops and the depth of the transport barrier for electrons increases.

We note that the maximum value of E_r in the best regimes attains $|E_r| \simeq 400$–500 V/cm, which, according to the equation

$$M\frac{dv_{i,r}}{dt} = E_r - \frac{1}{Z_i n_i e}\nabla p_i + \frac{1}{c}v_\perp B, \qquad (2)$$

corresponds to significant variations in the transverse velocity $v_\perp \simeq 2 \times 10^4$ m/s or ∇p_i ($T_i(r(\varphi_{\min})) \simeq 200$–$250$ eV for $T_i(0) \simeq 600$ eV). Under the steady-state conditions, these variations must occur because Eq. (2) must be satisfied.

This suggests the existence of a positive feedback whose scheme can be described as follows.

(i) The low electric field δE_r arising during the L–H transition generates the shear of the $\mathbf{E} \times \mathbf{B}$ flow, which partially suppresses turbulence.

(ii) The drop in the turbulence level leads to an increase in the transport barrier for electrons, whereas the ion transport velocity $\langle v_\perp \rangle_i$, according to [11], changes insignificantly.

(iii) All of this decreases the ratio $\langle v_e \rangle_\perp / \langle v_i \rangle_\perp$ and, consequently, increases (by an absolute value) the radial electric field E_r. Thus, the feedback loop is closed.

(iv) This process continues until a steady state is reached, which determines the final value of E_r and the depth of the electron transport barrier.

10. CONCLUSION

(i) An improved plasma confinement regime with an external transport barrier (H-mode) is obtained in ECRH experiments in T-10. The improvement factor $H_L = \tau_E^H / \tau_E^L$ attains 1.6.

(ii) The threshold power P_{th}^{LH} for the L–H transition is close to that predicted by the ITER scaling. The fact that the threshold power P_{th}^{LH} increases with increasing plasma density also agrees with the predictions of the ITER scaling.

(iii) The best results are obtained at low values of the safety factor ($q_L \longrightarrow 2$).

(iv) It is shown that, in the H-mode in T-10, a transport barrier for electrons arises. The thermal transport barrier has a much smaller depth and its contribution to improved confinement is insignificant.

ACKNOWLEDGMENTS

This work was supported in part by the Ministry of Atomic Energy of the Russian Federation (agreement no. 69F) and the Ministry of Science and Technology of the Russian Federation (under the federal program "Controlled Fusion and Plasma Processes").

REFERENCES

1. K. H. Burrell, Phys. Plasmas **6** (12), 4418 (1999).
2. Yu. V. Esipchuk, Plasma Phys. Controlled Fusion **37**, A267 (1995).
3. *Technical Basis for the ITER-FEAT Outline Design*, Chap. 1, Sect. 2, p. 3.
4. Yu. V. Esipchuk, A. Ya. Kislov, K. N. Tarasyan, *et al.*, J. Mosc. Phys. Soc., No. 1, 119 (1991).
5. K. A. Razumova, V. V. Alikaev, A. Ya. Kislov, *et al.*, in *Proceedings of the 26th EPS Conference on Plasma Physics and Controlled Fusion* (Maastricht, 1999), Vol. 23J, p. 77.
6. A. V. Melnikov, L. G. Eliseev, L. I. Krupnik, *et al.*, in *Proceedings of the 26th EPS Conference on Plasma Physics and Controlled Fusion* (Maastricht, 1999), Vol. 23J, p. 829.
7. V. A. Vershkov, V. V. Dreval, and S. V. Soldatov, Rev. Sci. Instrum. **70** (3), 2903 (1999).
8. Yu. N. Dnestrovskij, Yu. V. Esipchuk, N. A. Kirneva, *et al.*, Fiz. Plazmy **23**, 623 (1997) [Plasma Phys. Rep. **23**, 566 (1997)].
9. M. V. Ossipenko, Fiz. Plazmy **23**, 909 (1997) [Plasma Phys. Rep. **23**, 837 (1997)]; Yu. N. Dnestrovskij, M. V. Ossipenko, and S. V. Tsaun, Fiz. Plazmy **24**, 771 (1998) [Plasma Phys. Rep. **24**, 715 (1998)].
10. R. V. Shurygin, Fiz. Plazmy **25**, 739 (1999) [Plasma Phys. Rep. **25**, 677 (1999)].
11. V. V. Alikaev, A. A. Bagdasarov, A. A. Borschegovskij, *et al.*, in *Proceedings of the 10th International Conference on Plasma Physics and Controlled Nuclear Fusion* (London, 1984); Nucl. Fusion Suppl. **1**, 419 (1985).

Translated by N. Larionova

Plasma Physics Reports, Vol. 26, No. 11, 2000, pp. 931–937. Translated from Fizika Plazmy, Vol. 26, No. 11, 2000, pp. 993–999.

PLASMA OSCILLATIONS AND WAVES

Scattering of Polarized Radio Waves by Langmuir Turbulence in a Plasma in a Magnetic Field

V. V. Tirsky*, V. G. Ledenev, and V. M. Tomozov****

**Institute of Laser Physics, Irkutsk Branch, Siberian Division, Russian Academy of Sciences, Irkutsk, Russia*

***Institute of Solar and Terrestrial Physics, Siberian Division, Russian Academy of Sciences, Irkutsk, 664033 Russia*

Received November 10, 1999; in final form, April 3, 2000

Abstract—A study is made of radio-wave scattering by Langmuir turbulent pulsations in a plasma in a magnetic field. The effect of this process on the polarization of radio waves at frequencies far above or close to the electron plasma frequency is investigated. The wave scattering by Langmuir turbulence is shown to strongly affect the polarization characteristics. When the optical thickness typical of the scattering process is on the order of unity, the degree of wave polarization can change by 30% both at high frequencies and at frequencies close to the plasma frequency, in which case the circular polarization can reverse direction. It is shown that, as a result of wave scattering by Langmuir turbulence, the degree of circular polarization of radio waves depends on the wavelength even in a uniform magnetic field. *© 2000 MAIK "Nauka/Interperiodica".*

1. INTRODUCTION

The polarization characteristics of radio emission from plasmas are of considerable interest for both laboratory experiments and space research. Under astrophysical conditions and in laboratory experiments, the interaction between electron beams and plasmas is often accompanied by the onset of turbulence (in particular, Langmuir turbulence). Astrophysical plasmas (e.g., the solar corona) are often homogeneous on spatial scales typical of the scattering of electromagnetic radiation by Langmuir turbulent pulsations. In laboratory devices with injection of electron beams (in particular, in the GOL-3 device [1–3]), many methods for diagnosing high-temperature plasmas (with an electron temperature of about 10 keV) are based on analyzing the parameters of both intrinsic electromagnetic radiation emitted from the plasma and laser light scattered by the plasma [1–8], in which case the plasma can be assumed to be essentially homogeneous along the magnetic field.

The polarization of the emitted electromagnetic waves, along with the other wave parameters, is an important characteristic that provides insights into the mechanisms for radio emission from space objects and the conditions prevailing in the regions where radio waves are generated [9]. Of particular interest is the study of solar radio waves, because there is a large amount of experimental data in this area of research [10, 11]. However, the experimental data often disagree with theoretical predictions. Thus, Ledenev [12] showed that some types of radio waves emitted from the Sun should be completely polarized, while observations do not usually reveal such a high degree of polarization [13]. Additionally, in many broadband sources, the degree of polarization of the emitted radio waves depends on the wavelength [11]. Moreover, it was found that radio waves of the same type may have different polarizations (see [14, 15]), which also contradicts the results of calculations. However, these contradictions can naturally be explained if we take into account the fact that, under astrophysical conditions and in many laboratory experiments, radio waves are generated and propagate in turbulent plasmas. Below, we will consider the scattering of radio waves by turbulent pulsations in a homogeneous plasma and the effect of this scattering process on the polarization characteristics of radio waves at frequencies far above (Section 2) and close to (Section 3) the electron plasma frequency.

2. SCATTERING OF HIGH-FREQUENCY RADIO WAVES

2.1. Basic Equations

The equations describing the Raman scattering of polarized radio waves by turbulent pulsations in a plasma in a magnetic field were derived in [6]. In this section, we analyze a plasma with an isotropic Langmuir turbulence described by the spectral function $W(\mathbf{k})$, which is inversely proportional to the squared wavenumber of the Langmuir plasmons [5]. We begin by assuming that the following conditions are satisfied:

$$\begin{aligned}&(\omega_{He}/\omega)^2, \quad (\omega_{He}/\omega')^2 \ll 1,\\ &(\omega_{pe}/\omega)^4, \quad (\omega_{pe}/\omega')^4 \ll 1,\end{aligned} \tag{1}$$

where ω_{pe} is the electron Langmuir frequency, ω_{He} is the electron gyrofrequency, and ω and ω' are the frequencies of the incident and scattered electromagnetic waves. When the optical thickness characteristic of the

1063-780X/00/2611-0931$20.00 © 2000 MAIK "Nauka/Interperiodica"

scattering process is on the order of unity and the condition $\Delta\omega < \omega_{pe}$ (where $\Delta\omega$ is the spectral width of the frequency spectrum of the emitted radiation) holds, the equations describing the propagation of polarized radio waves in a plasma in a uniform magnetic field with allowance for wave scattering by Langmuir turbulent pulsations have the form

$$\frac{dI_\omega}{dt} = -\sigma_0 f_1(\omega) I_\omega - \sigma_0 f_2(\omega) V_\omega \cos\vartheta + v_g S_I(\omega), \quad (2)$$

$$\frac{dV_\omega}{dt} = -\sigma_0 f_1(\omega) V_\omega - \sigma_0 f_2(\omega) I_\omega \cos\vartheta + v_g S_V(\omega), \quad (3)$$

$$\frac{dU_\omega}{dt} = -\sigma_0 f_1(\omega) U_\omega + v_g S_U(\omega), \quad (4)$$

$$\frac{dQ_\omega}{dt} = -\sigma_0 f_1(\omega) Q_\omega + v_g S_Q(\omega). \quad (5)$$

Here, I_ω, U_ω, Q_ω, and V_ω are the Stokes parameters of the radio emission; the functions f_1 and f_2 are equal to

$$f_1(\omega) = (((\omega - \omega_{pe})^2 - \omega_{pe}^2)^{1/2} + ((\omega + \omega_{pe})^2 - \omega_{pe}^2)^{1/2})/2\omega, \quad (6)$$

$$f_2(\omega) = ((\omega_{He}(\omega + \omega_{pe})^{-1} + \omega_{He}\omega^{-1})((\omega + \omega_{pe})^2 - \omega_{pe}^2)^{1/2} + (\omega_{He}(\omega - \omega_{pe})^{-1} + \omega_{He}\omega^{-1}) \times ((\omega - \omega_{pe})^2 - \omega_{pe}^2)^{1/2})/2\omega; \quad (7)$$

and

$$\sigma_0 = \frac{\pi}{3}\frac{\omega_{pe}^2}{v_g}\frac{T_e}{m_e c^2}\frac{W}{n_e T_e}\frac{1}{k_{1\max} - k_{1\min}}, \quad (8)$$

where T_e is the electron temperature expressed in J, n_e is the electron plasma density, c is the speed of light in vacuum, v_g is the group velocity of the electromagnetic waves, $k_{1\max}$ and $k_{1\min}$ are the maximum and minimum wavenumbers of the Langmuir turbulence spectrum, and $W = \int \frac{d\mathbf{k}}{(2\pi)^3} W(\mathbf{k})$ is the energy of turbulent pulsations per unit plasma volume. All quantities (except for temperature) are expressed in SI units. The functions S_I, S_U, S_Q, and S_V describe the sources of radio emission in a plasma.

2.2. How the Polarization of Radio Waves Changes due to Scattering in a Turbulent Plasma Slab

When highly directed ($\Delta\theta \ll \pi$) narrowband ($\Delta\omega \ll \omega_{pe}$) radio emission penetrates through a plane-parallel turbulent plasma slab in which there are no sources of radio waves in the frequency range under consideration (S_I, S_U, S_Q, $S_V = 0$), Eqs. (2)–(5) yield the following expressions for the intensities $I_L = (I - V)/2$ and $I_R = (I + V)/2$ of the ordinary and extraordinary waves that have crossed the slab:

$$I_R(z) = I_{R0}\exp(-\sigma_0 z v_g^{-1}(\cos\vartheta)^{-1} \times (f_1(\omega) + f_2(\omega)\cos\vartheta)), \quad (9)$$

$$I_L(z) = I_{L0}\exp(-\sigma_0 z v_g^{-1}(\cos\vartheta)^{-1} \times (f_1(\omega) - f_2(\omega)\cos\vartheta)), \quad (10)$$

where I_{L0} and I_{R0} are the intensities of the incident ordinary and extraordinary waves, respectively.

Figure 1 shows the profiles of $I_R(z)/I_L(z)$ as a function of the optical thickness $\tau = \sigma_0 f_1(\omega) z/v_g$ of the plasma slab for radio waves at the second harmonic of

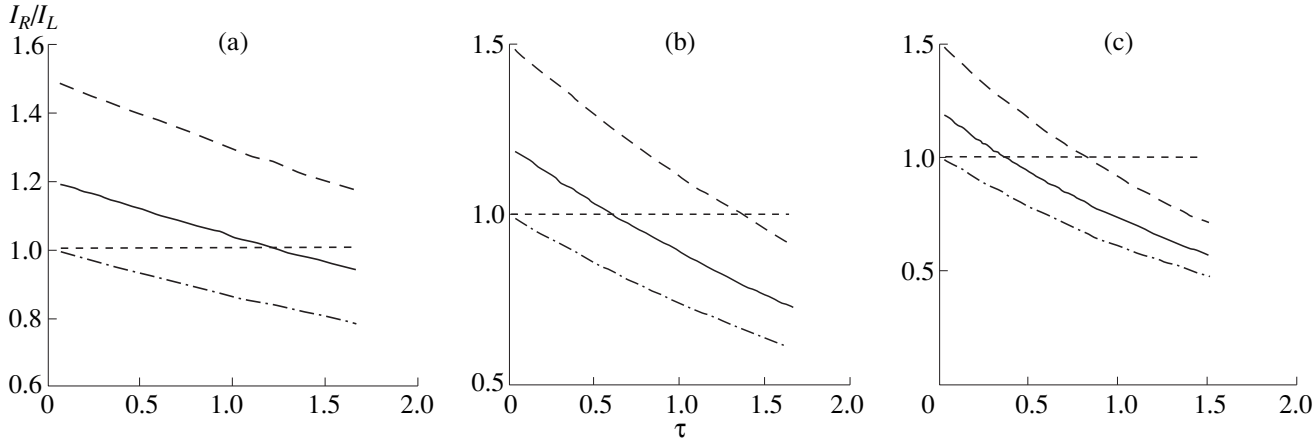

Fig. 1. Ratio of the intensities of extraordinary and ordinary waves propagating along the magnetic field at the second harmonic of the electron Langmuir frequency vs. the optical thickness at $\alpha = 0$ for different ratios of the initial intensities of these waves and for ω_{He}/ω_{pe} = (a) 0.1, (b) 0.2, and (c) 0.3.

the electron plasma frequency. The profiles were obtained for different values of I_{R0}/I_{L0} and for ω_{He}/ω_{pe} = 0.1, 0.2, and 0.3. We can see that, for optical thicknesses on the order of unity, the degree of polarization can change by 20–30%. Since extraordinary waves are scattered more efficiently than ordinary waves, the polarization of radio waves that have crossed the slab can reverse direction if the extraordinary mode dominates in the incident radiation (provided that the degree of polarization of the incident radiation is lower than 30%). As the frequency increases, the ratio I_R/I_L grows essentially in the same way as it does when ω_{He} decreases.

2.3. How the Polarization of Radio Waves Changes due to Scattering at the Exit from a Spherical Plasma Slab

We consider an isotropic source with a sufficiently narrow bandwidth ($\Delta\omega < \omega_{pe}$) inside a plasma region with Langmuir turbulence, assuming that the source is much smaller in size than the turbulent region. In this case, the scattering process can also change the polarization of radiation emitted from this region. Setting S_I, S_U, S_Q, and $S_V = 0$ in Eqs. (2)–(5), we obtain the intensities I_L and I_R of the ordinary and extraordinary waves that have passed through a semitransparent spherical plasma slab:

$$I_R(z) = I_{R0}\exp(-\sigma_0 z v_g^{-1}(f_1(\omega) + f_2(\omega)\cos\vartheta)), \quad (11)$$

$$I_L(z) = I_{L0}\exp(-\sigma_0 z v_g^{-1}(f_1(\omega) - f_2(\omega)\cos\vartheta)), \quad (12)$$

where I_{L0} and I_{R0} are, respectively, the intensities of the ordinary and extraordinary waves emitted by the source.

Our calculations show that the scattering process can polarize even unpolarized radiation from an isotropic source. Thus, if the optical thickness of the slab is equal to $\tau = 0.5$, then expressions (11) and (12) at $\omega_{He}/\omega_{pe} \simeq 0.2$–$0.3$ and $\theta = 0$ indicate that the degree of polarization of radio waves at the exit from the slab can be as high as 10% (the extraordinary mode being dominant) because the frequency of the scattered radiation is shifted from the frequency of the source by ω_{pe}.

2.4. Polarization of Radio Waves Emitted from a Spherical Turbulent Plasma Slab with a Source

We consider a source that is equal in size to the spherical plasma slab with Langmuir turbulence, assuming that $\Delta\omega < \omega_{pe}$. If the slab is semitransparent to the scattered radiation, then Eqs. (2)–(5) give the following expressions for the intensities of the ordinary and extraordinary waves emitted from the slab:

$$I_R = Q_R(1 - \exp(-\sigma_0 z v_g^{-1}(f_1(\omega) + f_2(\omega)\cos\vartheta))) \times v_g(\sigma_0(f_1(\omega) + f_2(\omega)\cos\vartheta))^{-1}, \quad (13)$$

$$I_L = Q_L(1 - \exp(-\sigma_0 z v_g^{-1}(f_1(\omega) - f_2(\omega)\cos\vartheta))) \times v_g(\sigma_0(f_1(\omega) - f_2(\omega)\cos\vartheta))^{-1}, \quad (14)$$

where $Q_R = (S_I + S_V)/2$ and $Q_L = (S_I - S_V)/2$.

Estimates from formulas (13) and (14) at $\omega_{He}/\omega_{pe} \simeq 0.2$–$0.3$ and $\tau = 0.5$ show that, as a result of scattering, the degree of circular polarization of the emitted radio waves can change by approximately 10% because extraordinary waves are scattered more efficiently.

Hence, our calculations show that, when the optical thickness of the scattering plasma slab is on the order of unity, the polarization of high-frequency ($\omega > 1.8\omega_{pe}$) radio emission that is dominated by the extraordinary mode and is scattered by Langmuir turbulent pulsations can change by approximately 30%. If the degree of polarization in the source is below 30%, then the polarization can reverse direction.

3. SCATTERING OF RADIO WAVES WITH FREQUENCIES ABOVE THE ELECTRON LANGMUIR FREQUENCY

Here, we analyze how the scattering process affects the polarization of radio waves with frequencies 1.05–$1.1\omega_{pe}$, assuming that the ratio of the electron gyrofrequency to the electron Langmuir frequency lies in the range 0.1–0.33. As in Section 2, we assume that the spectral function $W(\mathbf{k})$ of the Langmuir turbulence is isotropic and is inversely proportional to the squared wavenumber of the Langmuir plasmons [5]. We consider two cases: radio waves propagating nearly along and nearly transverse to the magnetic field.

3.1. Scattering of Radio Waves Propagating Nearly along the Magnetic Field

If we ignore thermal corrections, then electromagnetic waves in a magnetized plasma are described by the dispersion relation [16]

$$k^2(\varepsilon_\perp k_\perp^2 + \varepsilon_\parallel k_z^2) - \frac{\omega^2}{c^2}[(\varepsilon_\perp^2 - g^2 - \varepsilon_\perp\varepsilon_\parallel)k_\perp^2 + 2k^2\varepsilon_\perp\varepsilon_\parallel] + \frac{\omega^4}{c^4}\varepsilon_\parallel(\varepsilon_\perp^2 - g^2) = 0. \quad (15)$$

Here,

$$\varepsilon_\perp = \varepsilon_\parallel = 1 - (\omega_{pe}/\omega)^2; \quad (16)$$

$$g = -(\omega_{pe}^2\omega_{He}/\omega^3); \quad (17)$$

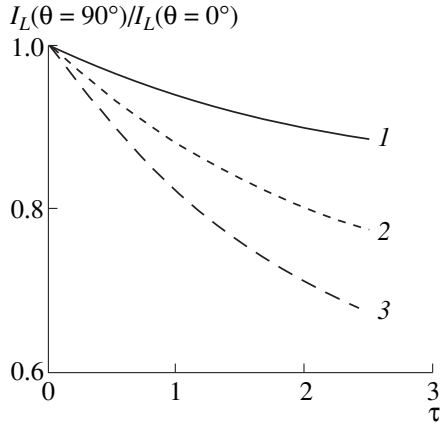

Fig. 2. Ratio of the intensities of ordinary waves propagating across and along the magnetic field at nearly the electron Langmuir frequency vs. the optical thickness at $\alpha = 0$ for ω_{He}/ω_{pe} = (*1*) 0.1, (*2*) 0.2, and (*3*) 0.3.

k_z and $k_\perp$ are the wave vector components parallel and perpendicular to the magnetic field, respectively; and k is the absolute value of the wave vector of the emitted radiation.

Under the conditions

$$k_\perp^2/k_z^2 \ll 1, \quad (g^2k_\perp^2/2k^2\varepsilon_\perp^2) \ll 1, \tag{18}$$

the dispersion relation for transverse waves (i.e., waves propagating nearly along the magnetic field) has the form

$$k^2c^2 = \omega^2(\varepsilon_\perp \pm |g|). \tag{19}$$

The plus and minus signs correspond to two independent polarized waves: the plus sign refers to the right-hand polarized (ordinary) wave and the minus sign refers to the left-hand polarized (extraordinary) wave.

Expressions (19), (16), and (17) imply that, under the condition $\varepsilon_\perp < |g|$, only ordinary waves can propagate nearly along the magnetic field. The intensity of right-hand polarized (ordinary) waves propagating in a plasma satisfies the transport equation [6]

$$\frac{dI_{\omega L}}{dt} = -(\sigma_0\{f_1'(\omega) - f_2'(\omega)\cos\theta\} + v_{gL}\alpha)I_{\omega L} + v_{gL}S_L(\omega), \tag{20}$$

where v_{gL} is the group velocity of the ordinary waves,

$$f_1'(\omega) = \{(\omega + \omega_{pe})^2 - \omega_{pe}^2\}^{1/2}/2\omega, \tag{21}$$

$$f_2'(\omega) = \{\omega_{He}(\omega + \omega_{pe})^{-1} + \omega_{He}\omega^{-1}\} \times \{(\omega + \omega_{pe})^2 - \omega_{pe}^2\}^{1/2}/2\omega, \tag{22}$$

and $\alpha(\omega)$ is the coefficient of the collisional absorption of radio waves by plasma particles.

The transport equation (20) for radio radiation emitted from a plane-parallel plasma slab has the solution

$$I_L(\omega, z, \theta) = \frac{S_L(\omega)v_{gL}}{\{\sigma_0\{f_1'(\omega) - f_2'(\omega)\cos\theta\} + v_{gL}\alpha\}} \times \left[1 - \exp\left(-z\frac{\{\sigma_0\{f_1'(\omega) - f_2'(\omega)\cos\theta\} + v_{gL}\alpha\}}{v_{gL}\cos\theta}\right)\right]. \tag{23}$$

3.2. Scattering of Radio Waves Propagating Nearly Transverse to the Magnetic Field ($\varepsilon_\perp < |g|$)

For radio waves propagating nearly transverse to the magnetic field, i.e., under the conditions opposite to inequalities (18), Eq. (19) yields the dispersion relation

$$k^2 = \frac{\omega^2}{c^2}\varepsilon_\parallel \tag{24}$$

for an ordinary wave and the dispersion relation

$$k^2 = \frac{\omega^2}{c^2}\frac{\{\varepsilon_\perp^2 - g^2\}}{\varepsilon_\perp} \tag{25}$$

for an extraordinary wave. When $\varepsilon_\perp < |g|$, extraordinary waves cannot propagate, because the right-hand side of (25) is negative and the corresponding conditions fail to hold.

The intensity of the scattered ordinary waves satisfies the equation [6]

$$\frac{dI_{\omega L}}{dt} = -(\sigma_0 f_1'(\omega) + v_{gL}\alpha)I_{\omega L} + v_{gL}S_L(\omega), \tag{26}$$

where v_{gL} is the group velocity of the ordinary waves. For a plane-parallel plasma slab, the solution to Eq. (26) has the form

$$I_L(\omega, z, \theta = \pi/2) = \frac{S_L(\omega)v_{gL}}{\{\sigma_0\{f_1'(\omega)\} + v_{gL}\alpha\}} \times \left[1 - \exp\left(-z\frac{\{\sigma_0\{f_1'(\omega)\} + v_{gL}\alpha\}}{v_{gL}}\right)\right]. \tag{27}$$

3.3. Effect of the Scattering Process on the Intensities of Ordinary Waves Propagating at Different Angles to the Magnetic Field ($\varepsilon_\perp < |g|$)

Formulas (23) and (27) make it possible to calculate the intensities I_L of ordinary waves propagating nearly transverse to the magnetic field and the intensities I_L of ordinary waves propagating nearly along the magnetic field at the exit from a plane-parallel plasma slab with allowance for wave scattering by Langmuir turbulent pulsations. Figure 2 shows the ratio of the intensity of ordinary waves propagating transverse to the magnetic field to the intensity of ordinary waves propagating along the field as a function of the optical thickness of

the plasma slab for different values of ω_{He}/ω_{pe} without taking into account collisional absorption. We can see that, when the optical thickness is below unity, the waves propagating transverse to the magnetic field are scattered more efficiently than those propagating along the magnetic field. In other words, in the presence of scattering turbulent pulsations in the plasma region where radio waves with frequencies $(1.05–1.1)\omega_{pe}$ are generated, transversely propagating ordinary waves are more efficiently (in comparison with longitudinally propagating ordinary waves) transformed into radio waves with frequencies close to the second harmonic of the electron Langmuir frequency, and this process is accompanied by the redistribution of transversely propagating waves over a 4π solid angle. As a result, the initially isotropic radiation can become anisotropic; i.e., radiation emitted along the magnetic field can be more intense than radiation emitted transverse to the magnetic field.

3.4. Radio Waves Propagating Nearly along the Magnetic Field ($|g| < \varepsilon_\perp$)

When the absolute value of g is smaller than $\varepsilon_\perp$, Eq. (19) implies that both ordinary and extraordinary waves can propagate nearly along the magnetic field. To the first order in the ratio ω_{He}/ω, the dispersion relation for these types of waves can be obtained from Eq. (19):

$$\omega^2 = k^2c^2 + \omega_{pe}^2\left(1 \mp \frac{\omega_{He}}{\sqrt{k^2c^2 + \omega_{pe}^2}}\right), \qquad (28)$$

where the plus and minus signs refer to extraordinary and ordinary waves, respectively.

The transport equation for extraordinary waves can be written as [6]

$$\frac{dI_{\omega R}}{dt} = -\{\sigma_0\{f_1'(\omega) + f_2'(\omega)\cos\theta\} + v_{gR}\alpha(\omega)\}I_{\omega R} + v_{gR}S_R(\omega), \qquad (29)$$

where v_{gR} is the group velocity of the extraordinary waves. In the case of a plane-parallel plasma slab, Eq. (29) has the solution

$$I_R(\omega, z, \theta) = \frac{S_R(\omega)v_{gR}}{\{\sigma_0\{f_1'(\omega) + f_2'(\omega)\cos\theta\} + v_{gR}\alpha\}} \times\left[1 - \exp\left(-z\frac{\{\sigma_0\{f_1'(\omega) + f_2'(\omega)\cos\theta\} + v_{gR}\alpha\}}{v_{gR}\cos\theta}\right)\right]. \qquad (30)$$

Equation (29) is similar in form to Eq. (20), and, in the case of a plane-parallel slab, solution (30) coincides with solution (23). Figure 3 displays profiles of the ratio I_R/I_L as a function of the optical thickness $\tau = \sigma_0 f_1'(\omega)z/v_g$ at $\omega_{He}/\omega = 0.1$, 0.2, and 0.3. Figure 4 presents the same profiles but for different initial values of I_{R0}/I_{L0} at $\omega_{He}/\omega = 0.2$. We can see that the degree of polarization can change by 20% when the optical thickness is on the order of unity and the polarization of the emitted radiation can even reverse direction when the emission from the source is dominated by an extraordinary mode.

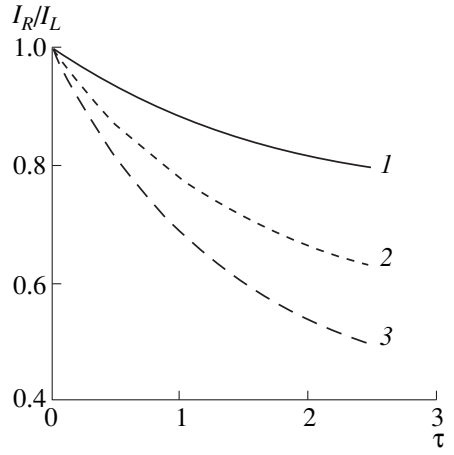

Fig. 3. Ratio of the intensities of extraordinary and ordinary waves propagating along the magnetic field at nearly the electron Langmuir frequency vs. the optical thickness at $\alpha = 0$ for ω_{He}/ω_{pe} = (*1*) 0.1, (*2*) 0.2, and (*3*) 0.3.

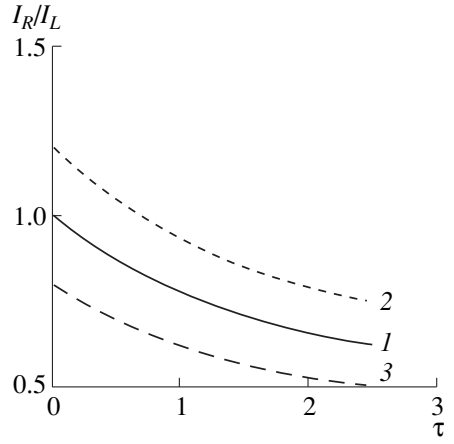

Fig. 4. The same as in Fig. 3 but for different ratios of the initial intensities of extraordinary and ordinary waves at $\omega_{He}/\omega_{pe} = 0.2$.

Note that solutions (23) and (30) are valid up to frequencies close to $2\omega_{pe}$, and as the frequency increases, the ratio I_R/I_L grows essentially in the same way as it does when the magnetic field decreases (Fig. 3).

3.5. Radio Waves Propagating Nearly Transverse to the Magnetic Field ($|g| < \varepsilon_\perp$)

When the absolute value of g is smaller than $\varepsilon_\perp$, Eqs. (24) and (25) imply that both ordinary and extraor-

dinary waves can propagate nearly transverse to the magnetic field. To the first order in the ratio ω_{He}/ω, the dispersion relation for these types of waves can be obtained from Eqs. (24) and (25):

$$\omega^2 = k^2c^2 + \omega_{pe}^2. \tag{31}$$

The transport equation for extraordinary waves has the form [6]

$$\frac{dI_{\omega R}}{dt} = -\{\sigma_0\{f_1'(\omega)\} + v_{gR}\alpha(\omega)\}I_{\omega R} + v_{gR}S_R(\omega). \tag{32}$$

In the case of a plane-parallel plasma slab, this equation has the solution

$$I_R(\omega, z, \theta = \pi/2) = \frac{S_R(\omega)v_{gR}}{\{\sigma_0 f_1'(\omega) + v_{gR}\alpha\}} \times\left[1 - \exp\left(-z\frac{\{\sigma_0 f_1'(\omega) + v_{gR}\alpha\}}{v_{gR}}\right)\right]. \tag{33}$$

Equation (32) is similar in form to Eq. (26), and, in the case of a plane-parallel slab, solution (33) coincides with (27). According to formulas (27) and (33), the extraordinary and ordinary waves are scattered essentially in the same manner, so that the scattering process has no impact on the degree of circular polarization of the radiation propagating transverse to the magnetic field.

4. CONCLUSION

Our calculations show that the scattering of radio waves by Langmuir turbulent pulsations can substantially change the polarization characteristics of radiation. When the optical thickness characteristic of the scattering process is on the order of unity, the degree of polarization of both high-frequency radio waves ($\omega \geq 2\omega_{pe}$) and radio waves with frequencies close to the electron Langmuir frequency can change by up to 30%. However, we must keep in mind that, when the same source generates radio waves at both the fundamental and higher harmonics of the electron Langmuir frequency, the polarization of radiation at the fundamental harmonic changes most strongly. The reason for this is that the group velocity of radiation at higher harmonics is higher than at the fundamental harmonic; thus, for higher harmonics, the plasma is far more transparent with respect to scattering. The most interesting result is that the polarization of the emitted radiation propagating through a plasma slab with the developed Langmuir turbulence can reverse direction, because extraordinary waves are scattered more efficiently than ordinary waves. After passing through a turbulent slab, the radiation that is emitted by the source and is initially dominated by the extraordinary mode may become dominated by an ordinary mode. Generally, this effect lowers the degree of polarization of radiation dominated by an extraordinary mode and raises the degree of polarization of radiation dominated by an ordinary mode.

Another interesting result is that, because of the wave scattering by Langmuir turbulent pulsations, the degree of circular polarization of radio waves depends on the wavelength even in a uniform magnetic field: the longer the wavelength, the higher the degree of polarization of radiation dominated by an ordinary mode.

Extraordinary and ordinary radio waves propagating nearly transverse to the magnetic field are both characterized by the same scattering coefficient. Consequently, the scattering process has no impact on the degree of circular polarization of radiation propagating transverse to the magnetic field. On the other hand, the scattering efficiencies of radio waves of the same type propagating in different directions with respect to the magnetic field are different, which gives rise to the anisotropy of the initially isotropic radiation (Fig. 2).

All of the above effects can be observed in laboratory experiments on the scattering of electromagnetic waves and in space plasmas in the presence of a magnetic field. These effects are most pronounced in the frequency range between the electron Langmuir frequency and the doubled electron Langmuir frequency.

Thus, Langmuir turbulence was observed to be generated during the interaction between a relativistic (0.8–1 MeV) electron beam with a current density of $J = 10$ kA/cm^2 and a plasma with a density of 10^{15} cm^{-3} in experiments carried out in the GOL-3 device (of length $l = 7.5$ m) at the Budker Institute of Nuclear Physics (Novosibirsk, Russia) [1–3]. Devices of this type are capable of creating plasmas with temperatures of up to 10^8 K. Langmuir turbulence can also be generated during the injection of an electron beam into a plasma with such a temperature and with a density of 10^{13}–10^{14} cm^{-3}, in which case the optical thickness characteristic of the scattering of electromagnetic waves by Langmuir turbulent pulsations is equal in order of magnitude to

$$\tau = \frac{\sigma_0 l}{c} = \frac{\pi}{3}\frac{\omega_{pe}l}{c}\frac{T_e}{m_e c^2}\frac{W}{n_e T_e}.$$

Consequently, for an electron energy of about 10–30 keV and a turbulence level of about $W/n_eT_e \sim 10^{-3}$–10^{-4}, the optical thickness for the electromagnetic radiation propagating at nearly the electron Langmuir frequency along the magnetic field in GOL-3 can be on the order of unity.

In space plasmas, the scattering by Langmuir turbulence manifests itself in the dependence of the degree of circular polarization of the emitted radiation on the turbulence level in the region where radio waves are generated. For example, during solar radio bursts, the polarization of the radio emission usually experiences fast variations and may even reverse direction [10].

ACKNOWLEDGMENTS

This work was supported in part by the Russian Foundation for Basic Research, project no. 98-02-17727.

REFERENCES

1. B. N. Breĭzman, L. N. Vyacheslavov, É. P. Kruglyakov, and A. L. Sanin, Fiz. Plazmy **20**, 42 (1994) [Plasma Phys. Rep. **20**, 36 (1994)].
2. B. N. Breizman, E. P. Kruglyakov, and L. N. Vyacheslavov, in *Proceedings of the IAEA Technical Committee Meeting on Time Resolved Two and Three Dimensional Plasma Diagnostics* (IAEA, Vienna, 1991), p. 442.
3. L. N. Vyacheslavov, I. V. Kandaurov, É. P. Kruglyakov, *et al.*, Fiz. Plazmy **18**, 225 (1992) [Sov. J. Plasma Phys. **18**, 119 (1992)].
4. J. Fujita, Fiz. Plazmy **20**, 217 (1994) [Plasma Phys. Rep. **20**, 203 (1994)].
5. V. N. Tsytovich, *Theory of Turbulent Plasma* (Atomizdat, Moscow, 1971; Plenum, New York, 1974).
6. V. V. Tirsky and V. M. Tomozov, Izv. Vyssh. Uchebn. Zaved., Fiz. **4**, 102 (1998).
7. V. V. Tirsky and V. M. Tomozov, Phys. Scr. **51**, 96 (1995).
8. V. V. Tirsky and S. N. Malov, Laser Phys. **6**, 1341 (1995).
9. V. V. Zheleznyakov, *Electromagnetic Waves in Space Plasma* (Nauka, Moscow, 1977).
10. V. V. Zheleznyakov, *Radio Emission from the Sun and Planets* (Nauka, Moscow, 1964).
11. A. Kruger, *Introduction to Solar Radio Astronomy and Radio Physics* (Reidel, Dordrecht, 1979; Mir, Moscow, 1984).
12. V. G. Ledenev, Sol. Phys. **179**, 405 (1998).
13. A. O. Benz and M. Gudel, Sol. Phys. **111**, 175 (1987).
14. S. Krucker, M. J. Aschwanden, T. S. Bastian, and A. O. Benz, Astron. Astrophys. **302**, 551 (1995).
15. S. Krucker, A. O. Benz, and M. J. Aschwanden, Astron. Astrophys. **317**, 569 (1997).
16. A. F. Alexandrov, L. S. Bogdankevich, and A. A. Rukhadze, *Principles of Plasma Electrocdynamics* (Vysshaya Shkola, Moscow, 1988; Springer-Verlag, Berlin, 1984).

Translated by O. Khadin

Plasma Physics Reports, Vol. 26, No. 11, 2000, pp. 938–946. Translated from Fizika Plazmy, Vol. 26, No. 11, 2000, pp. 1000–1009.

PLASMA OSCILLATIONS AND WAVES

Large-Angle Stimulated Raman Scattering of Short Laser Pulses in Plasma

S. Yu. Kalmykov

Institute for High Energy Densities, Associated Institute for High Temperatures, Russian Academy of Sciences, Izhorskaya ul. 13/19, Moscow, 127412 Russia

e-mail: kalmykov@hedric.msk.su

Received May 11, 2000

Abstract—The features of the large-angle stimulated Raman scattering of short laser pulses in a homogeneous underdense plasma are studied analytically. It is found that, for scattering angles that are not too close to zero, a steady-state regime of the convective amplification of unstable waves is established in the frame of reference comoving with the laser pulse. The problem of convective amplification in a two-dimensional region is solved in both weak- and strong-coupling regimes. It is shown that the steady-state envelopes of the scattered radiation and scattering plasma waves are two-dimensional in nature. It is found that, for a given scattering angle, the maximum possible spatial amplification at the trailing edge of the pulse is achieved if the ratio of the transverse to longitudinal size of the pulse is larger than the cotangent of one-half of the scattering angle. © *2000 MAIK "Nauka/Interperiodica".*

1. INTRODUCTION

Stimulated Raman scattering (SRS) [1] is one of the most important parametric processes [2] accompanying the propagation of high-power ultrashort (subpicosecond) [3] laser pulses in an underdense plasma ($\omega_0 \gg \omega_{pe}$, where ω_0 is the laser frequency and $\omega_{pe} = (4\pi e^2 n_0/m_e)^{1/2}$ is the electron plasma frequency corresponding to the unperturbed plasma electron density n_0). The incident electromagnetic (EM) wave (the pump wave) is scattered by spontaneous electron density fluctuations, which in turn can be enhanced by the ponderomotive force at the beat frequency of the pump wave and the scattered EM wave. If the waves meet certain phase relations, a positive feedback arises, which leads to the onset of either temporal or spatial instability [4]. Large-angle SRS can significantly affect the propagation of ultrashort (subpicosecond) laser pulses in plasma and, consequently, the operation of plasma-based laser accelerators using such pulses [5]. In this connection, it is important to determine the maximum achievable amplification coefficient of unstable waves for a given scattering angle, as well as to find out whether this amplification coefficient is achievable for the given pulse dimensions.

In the weak-coupling regime ($a_0 \ll (\omega_{pe}/\omega_0)^{1/2}$, where $a_0 = eE_0/(m_e\omega_0 c)$ is the normalized amplitude of the laser field), and SRS at angles that are not too close to zero is a three-wave process. A high-frequency EM pump wave (ω_0, $\mathbf{k}_0$) decays into a high-frequency scattered EM wave ($\omega_0 - \omega_{BG}$, $\mathbf{k}_s$) and an electron mode close to the natural plasma mode (ω_{BG}, $\mathbf{k}_e$), where $\mathbf{k}_e = \mathbf{k}_0 - \mathbf{k}_s$ and $\omega_{BG} = [\omega_{pe}^2 + 3(k_e V_{Te})^2]^{1/2} \approx \omega_{pe}$ is the frequency of the scattering plasma wave. In this case, the spectral width of the scattered radiation is small compared to the electron plasma frequency, because the weak-coupling regime implies that the temporal growth rate of the instability is much less than ω_{pe}. In the strong-coupling regime [6] ($a_0 \gg (\omega_{pe}/\omega_0)^{1/2}$), the scattering is nonresonant in character: the scattering electron modes are not close to the natural plasma modes, and their spectrum is much wider than the electron plasma frequency (this implies that the maximum value of the temporal growth rate is larger than ω_{pe}). A comprehensive review of the temporal growth rates of the SRS instability in various regimes is presented in [7].

The solution to the problem of the temporal SRS instability (i.e., the initial problem) does not provide an adequate description of large-angle SRS under real experimental conditions when the instability develops in a spatially limited region, which requires taking into account the boundary conditions on the plasma boundary and the laser-pulse edges. The region of the wave interaction may be limited by the finite dimensions of the laser focal region [8] where the plasma is produced. Such a situation is characteristic of sufficiently long laser beams with a length $L_\parallel$ much longer than the Rayleigh length $r_R = k_0 L_\perp^2/2$, where $L_\perp$ is the focal spot size (in this case, the longitudinal size of the plasma produced in the laser focus is on the order of the Rayleigh length). Here, we will consider the opposite situation, where the laser pulse is fairly short ($L_\parallel \ll r_R$) and the longitudinal size of the interaction region is determined by the pulse length. If the plasma length is much longer than the pulse length and the scattering occurs at an angle that is not too close to zero, then, in the frame of

reference moving with the pulse, a steady-state regime of convective amplification of unstable waves can be established in the region occupied by the pulse. In this case, the amplification is two-dimensional in character [9, 10].

In this paper, we restrict ourselves to considering the linear stage of the SRS instability. Therefore, the applicability conditions of the linear theory [11], which are associated with the depletion of the pump wave and determine the limiting value of the convective amplification coefficient, are assumed to be satisfied. We consider the linear regime of the steady-state convective amplification in a spatially limited (rectangular) two-dimensional region in the comoving frame of reference under the conditions of weak and strong coupling. In the strong-coupling regime, the electron motion in a pump field is assumed to be nonrelativistic (large-angle SRS of relativistically strong laser pulses is studied in [12]). In Section 2, we write the basic equations that are used to analyze the instability in the weak- and strong-coupling regimes. The initial–boundary problem is formulated in a rectangular two-dimensional region in the comoving frame. The boundary conditions at the leading edge and side boundaries of the pulse correspond to a certain constant level of the electron density fluctuations in an unperturbed plasma. In Section 3.1, a time-independent boundary problem is solved. It is shown that the SRS instability depends substantially on the transverse size of the pulse; under certain conditions, the finite transverse size of the pulse can significantly limit the maximum amplification coefficient of unstable waves. It is found that the maximum achievable amplification coefficient at the trailing edge of the pulse does not depend on the scattering angle; for the given scattering angle α (counted from the propagation direction of the pulse), it is achieved if the inequality $L_\perp/L_\parallel > \cot(\alpha/2)$ is satisfied. This result is valid for both weak- and strong-coupling regimes (in the former case, it coincides with the results of [9, 10]). It is shown that, within the applicability limits of the basic equations, the solution to the initial–boundary problem approaches the mentioned steady-state amplification regime. By using the explicit steady-state solutions obtained, we study in Section 3.2 the applicability limits of the basic model equations; in particular, it is shown that our results are consistent with the results of [13, 14], from which it follows that the steady-state spatial amplification cannot be realized for sufficiently small scattering angles, such that $\alpha < (k_0 L_\perp)^{-1}$.

In the Conclusion, the results obtained are summarized.

2. BASIC EQUATIONS

We represent the high-frequency electric field in the form

$$\mathbf{a}(\mathbf{r}, t) = \frac{1}{2}(\mathbf{a}_0(\mathbf{r}, t)e^{-i\omega_0 t + ik_0 z} + \mathbf{a}_s(\mathbf{r}, t)e^{-i\omega_s t + i(\mathbf{k}_s, \mathbf{r})}) + \text{c.c.}, \quad (1)$$

where $\omega_s \approx \omega_0$. The normalized envelopes of the laser pulse and scattered radiation ($a_0 = eE_0/(m_e\omega_0 c)$ and $a_s = eE_s/(m_e\omega_s c)$ are assumed to vary slowly in time and space on the scales $\omega_{0(s)}^{-1}$ and $k_{0(s)}^{-1}$, respectively; i.e., $|\partial a_{0(s)}/\partial t| \ll \omega_{0(s)}|a_0|$ and $|\partial a_{0(s)}/\partial \mathbf{r}| \ll k_{0(s)}|a_{0(s)}|$. In this paper, the problem is solved in the nonrelativistic limit; i.e., we assume $|a_{0(s)}| \ll 1$. Both the incident and scattered waves are assumed to satisfy the dispersion relation for EM waves in a plasma: $\omega_{0(s)}^2 = (k_{0(s)}c)^2 + \omega_{pe}^2$. Since we will consider below the SRS in a highly underdense plasma, we can set $\omega_s = \omega_0$ and $k_s \equiv |\mathbf{k}_s| = k_0$, including small deviations of the frequency and wave vector of scattered radiation from ω_0 and k_0 into the spatiotemporal dependence of the envelope $\mathbf{a}_s(\mathbf{r}, t)$. Thus, the longitudinal and transverse components of the wave vector of scattered radiation are determined by $\mathbf{k}_s = (\mathbf{k}_{s\perp}, k_0\cos\alpha)$, where $k_{s\perp} \equiv |\mathbf{k}_{s\perp}| = k_0\sin\alpha$. The ponderomotive force at the beat frequency of the pump wave and scattered EM wave excites the scattering electron density perturbations

$$\delta\tilde{n}_s(\mathbf{r}, t) = \frac{1}{2}\delta n_s(\mathbf{r}, t)e^{i(\mathbf{k}_e \cdot \mathbf{r})} + \text{c.c.} \quad (2)$$

with the characteristic wave vector $\mathbf{k}_e = \mathbf{e}_z k_0 - \mathbf{k}_s$ such that $k_{e_z} = 2k_0\sin^2(\alpha/2)$ and $k_e \equiv |\mathbf{k}_e| = 2k_0\sin(\alpha/2)$.

We assume that the electron plasma is on average uniform and that there are no long-wavelength ($\lambda \gg k_e^{-1}$) perturbations of the electron density. (Note that such perturbations can significantly suppress the SRS instability [15, 16].) We will describe the SRS of a short laser pulse ($L_\parallel/c \ll \omega_{pi}^{-1} = (4\pi e^2 n_0/m_i)^{-1/2}$, where ω_{pi} is the ion plasma frequency) at a given angle in an underdense plasma using nonrelativistic hydrodynamic equations for a cold electron fluid against the immobile ion background and the Maxwell equations for the scattered radiation. From this set of equations, we obtain the coupled reduced equations for the amplitude $\mathbf{a}_s$ of the scattered EM wave and the dimensionless envelope $N_s \equiv \delta n_s/n_0$ of the scattering electron density perturbations

$$\left[i\left(\frac{\partial}{\partial t} + \mathbf{v}_g \cdot \nabla\right) + \frac{c^2}{2\omega_0}\Delta_\perp\right]\mathbf{a}_s = \frac{\omega_{pe}^2}{4\omega_0}\left(\mathbf{a}_0 - \frac{\mathbf{k}_{s\perp}}{k_0^2}(\mathbf{k}_{s\perp} \cdot \mathbf{a}_0)\right)N_s^*, \quad (3)$$

$$\left(\frac{\partial^2}{\partial t^2} + \omega_{pe}^2\right)N_s^* = -\frac{1}{2}(k_e c)^2(\mathbf{a}_0^* \cdot \mathbf{a}_s), \quad (4)$$

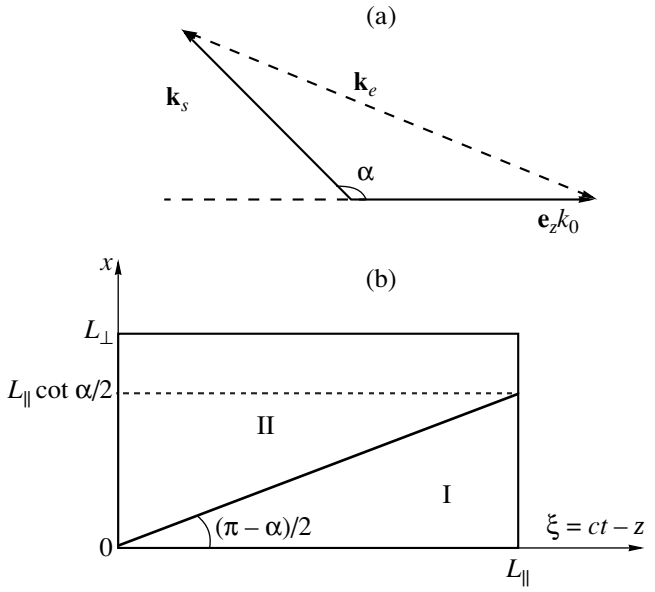

Fig. 1. Geometry of large-angle SRS. (a) Wave-vector diagram in the laboratory frame of reference. (b) The interaction region in the coordinates x and $\xi = ct - z$ (in the comoving frame of reference). The boundary conditions are imposed at $x = 0$ and $\xi = 0$. In region I, in which the solution is affected by the boundary condition at the side boundary $x = 0$, the spatial amplification of the decay waves is two-dimensional in character. Region II corresponds to the regime of one-dimensional amplification of the decay waves along the ξ-axis (i.e., toward the trailing edge of the pulse). For the scattering angles satisfying the inequality $\alpha < 2\arctan(L_\parallel/L_\perp)$, the training edge of the pulse entirely lies in the region affected by the boundary condition at $x = 0$.

where $\mathbf{v}_g = c^2\mathbf{k}_s/\omega_0$ is the group velocity of the scattered EM wave. For a highly underdense plasma, we can neglect the difference between $v_g \equiv |\mathbf{v}_g|$ and the speed of light in a vacuum c. Below, we will consider the case of linearly polarized laser light and analyze the SRS in the plane that is orthogonal to the plane of polarization ($\mathbf{k}_{s\perp} \perp \mathbf{a}_0$) and in which the amplification coefficient of unstable waves is maximum [11]. Thereby, the two-dimensional geometry of the SRS is defined as is shown in Fig. 1a. We will investigate the SRS at a given angle in the frame of reference comoving with the laser pulse. In this frame, it is convenient to choose the distance from the leading edge of the pulse $\xi = ct - z$ as the longitudinal variable; the time t and the transverse variable x are not transformed when passing over to the comoving frame. It is assumed that the pulse is localized in the longitudinal and transverse directions in the scattering plane and has a rectangular envelope:

$$\mathbf{a}_0(x, \xi) = \mathbf{e}_0 a_0, \tag{5}$$

where $\mathbf{e}_0$ is the unit polarization vector of the pump field and the pump-field amplitude a_0 is constant at $0 \le \xi \le L_\parallel$ and $0 \le x \le L_\perp$ and is equal to zero outside of this region. Therefore, the region of the wave interaction is a rectangle with the longitudinal size $L_\parallel$ and transverse size $L_\perp$ (see Fig. 1b).

Under the condition

$$\left|\frac{\partial a_s}{\partial x}\right| \ll k_{s_x}|a_s| = k_0 \sin\alpha |a_s|, \tag{6}$$

which implies that the scattered EM wave is short-wavelength in both the longitudinal and transverse directions, we can consider the scattered EM wave to be quasi-planar and neglect the transverse Laplacian in Eq. (3). In Section 3.2, we will show that this condition determines the lower and upper limiting values of the scattering angle at which condition (6) is satisfied and the related reduction of the order of the equation for the envelope of scattered radiation is formally justified. The following analysis is related to different approximations of Eq. (4) for the scattering electron density perturbations in the weak- and strong-coupling regimes.

In the weak-coupling regime ($\omega_{pe}/\omega_0 \gg a_0^2$), the scattering electron density wave is close to the natural plasma mode. This allows us to further reduce Eqs. (3) and (4) representing the amplitudes of the decay waves in the form

$$\{\mathbf{a}_s, N_s^*\} = \{\hat{\mathbf{a}}_s, \hat{N}_s^*\} e^{i\omega_{pe}t - i(\mathbf{k}_p \cdot \mathbf{r})}, \tag{7}$$

where $\mathbf{k}_p \parallel \mathbf{k}_s$, $k_p \equiv |\mathbf{k}_p| = \omega_{pe}/c$, and the amplitudes $\hat{N}_s$ and $\hat{a}_s$ vary slowly on the scales ω_{pe}^{-1} and k_p^{-1}. In the comoving frame, the reduced equations take the form

$$\left[\frac{\partial}{\partial t} + 2c\sin^2(\alpha/2)\left(\frac{\partial}{\partial \xi} + \cot(\alpha/2)\frac{\partial}{\partial x}\right)\right]\hat{A}_1 = \gamma_0 \hat{A}_2, \tag{8}$$

$$\left(\frac{\partial}{\partial t} + c\frac{\partial}{\partial \xi}\right)\hat{A}_2 = \gamma_0 \hat{A}_1, \tag{9}$$

where $\hat{A}_1 \equiv 2i\hat{a}_s(\omega_0/\omega_{pe})^{3/2}\sin(\alpha/2)$, $\hat{A}_2 \equiv \hat{N}_s^*$, and $\gamma_0 = (a_0/2)(\omega_0\omega_{pe})^{1/2}\sin(\alpha/2) \ll \omega_{pe}$ is the familiar temporal growth rate of the instability associated with the SRS at the angle α in an unbounded plasma [7] in the weak-coupling regime. We formulate the initial–boundary problem for Eqs. (8) and (9) with the following initial conditions and boundary conditions at the leading edge ($\xi = 0$) and side boundary (for definiteness, $x = 0$) of the pulse:

$$\begin{aligned}\hat{A}_1(t, x, \xi = 0) &= \hat{A}_1(t, x = 0, \xi) \\ &= \hat{A}_1(t = 0, x, \xi) \equiv 0,\end{aligned} \tag{10}$$

$$\begin{aligned}\hat{A}_2(t, x, \xi = 0) &= \hat{A}_2(t, x = 0, \xi) \\ &= \hat{A}_2(t = 0, x, \xi) = \hat{N}_0 = \text{const}.\end{aligned} \tag{11}$$

In the strong-coupling regime ($\omega_{pe}/\omega_0 \ll a_0^2 < 1$), the scattering electron density perturbations are not

close to the natural plasma modes and the growth rate of the SRS instability is much higher than the electron plasma frequency. This allows us to neglect the term with the plasma frequency squared as compared to the second time derivative in Eq. (4). As a result, the equations in the comoving frame take the form

$$\left[\frac{\partial}{\partial t} + 2c\sin^2(\alpha/2)\left(\frac{\partial}{\partial \xi} + \cot(\alpha/2)\frac{\partial}{\partial x}\right)\right]A_1 = -i\left(\frac{2}{\sqrt{3}}\Gamma_0\right)^{3/2}A_2, \quad (12)$$

$$\left(\frac{\partial}{\partial t} + c\frac{\partial}{\partial \xi}\right)^2 A_2 = -\left(\frac{2}{\sqrt{3}}\Gamma_0\right)^{3/2}A_1, \quad (13)$$

where $A_1 \equiv a_s(2\omega_0/\omega_{pe})^{3/2}\sin(\alpha/2)$, $A_2 \equiv N_s^*/\omega_{pe}^{1/2}$, and $\Gamma_0 = \sqrt{3}\,[(a_0/4)^2\omega_{pe}^2\,\omega_0\sin^2(\alpha/2)]^{1/3}$ is the familiar growth rate of the instability associated with SRS at the angle α in an unbounded plasma [7] in the strong-coupling regime ($\Gamma_0 \gg \omega_{pe}$). For this set of equations, we also formulate the initial–boundary problem with the following initial conditions and boundary conditions at the leading edge and side boundary of the pulse:

$$A_1(t, x, \xi = 0) = A_1(t, x = 0, \xi) = A_1(t = 0, x, \xi) \equiv 0, \quad (14)$$

$$A_2(t, x, \xi = 0) = A_2(t, x = 0, \xi) = A_2(t = 0, x, \xi) = \omega_{pe}^{-1/2}N_0 = \text{const}, \quad (15)$$

$$\frac{\partial A_2}{\partial \xi}(t, x, \xi = 0) = \frac{\partial A_2}{\partial t}(t = 0, x, \xi) \equiv 0. \quad (16)$$

The boundary conditions for Eqs. (8) and (9) or (12) and (13) correspond to the propagation of a laser pulse in a plasma with a constant level of seed electron density fluctuations. The side boundary ($x = L_\perp$) and trailing edge ($\xi = L_\parallel$) of the pulse are the transparent boundaries through which the decay waves leave the interaction region. At these boundaries, the amplitudes of the decay waves are completely determined by the solutions to the initial–boundary problem for Eqs. (8) and (9) or (12) and (13). In the next section, we will analyze these solutions.

3. SPATIAL AMPLIFICATION OF WAVES IN A TWO-DIMENSIONAL REGION IN A COMOVING FRAME OF REFERENCE

3.1. Steady-State Solutions Describing the Amplification of Waves in a Two-Dimensional Region

If the scattering angle is not too close to zero (if $\alpha > \max\{(k_0L_\perp)^{-1}, 2(L_\parallel/L_\perp)^{1/2}(k_0L_\perp)^{-1/2}\}$, as will be shown in Section 3.2), then both the scattered EM wave and the scattering plasma wave leave the interaction region through the trailing edge ($\xi = L_\parallel$) and side boundary ($x = L_\perp$) of the pulse. Since, in this case, the SRS instability is convective in character, we can expect that, in the comoving frame of reference, the interacting waves will arrive at a steady state as time elapses. In this section, we obtain steady-state solutions to the boundary problems for Eqs. (8) and (9) or (12) and (13), describing convective amplification of waves in a two-dimensional region, and prove that the solutions to the initial–boundary problem arrive at this steady-state regime of amplification. In Section 3.2, we determine the range of scattering angles in which the solutions obtained formally satisfy the applicability condition (6) of Eqs. (8) and (9) or (12) and (13).

In order to obtain steady-state solutions to the boundary problems, we omit the time derivatives in Eqs. (8) and (9) or (12) and (13). In the region $\xi \geq 0$ and $x \geq 0$, we apply the Laplace transformation with respect to ξ to obtain an ordinary differential equation with the boundary condition at $x = 0$, from which we get the Laplace transform as a function of x. The inversion of the Laplace transform gives us the sought solution to the two-dimensional time-independent boundary problem.

When solving Eqs. (8) and (9), describing the instability in the weak-coupling regime, it is convenient to introduce the normalized amplitude of scattered radiation $\hat{B}_1(x, \xi) = \sqrt{2}\sin(\alpha/2)\hat{A}_1(x, \xi)$ whose Laplace transform is

$$\hat{B}_1(x, s) = \frac{\hat{N}_0\kappa_0}{s^2 - \kappa_0^2}\left\{1 - \exp\left[-\left(s - \frac{\kappa_0^2}{s}\right)x\tan\frac{\alpha}{2}\right]\right\}. \quad (17)$$

The quantity $\kappa_0 = (a_0/2)(k_pk_0/2)^{1/2} \ll k_p$ is the familiar spatial growth rate of the convective instability associated with a large-angle SRS in the comoving frame of reference in the weak-coupling regime [11, 16]. The normalized amplitude $\hat{B}_1(x, \xi)$ obtained by inverting expression (17) has the form

$$\hat{B}_1(x, \xi) = \hat{N}_0\left[\sinh(\kappa_0\xi) - H\left(\xi - x\tan\frac{\alpha}{2}\right)\right.$$
$$\times \sum_{l=1}^{\infty}\left(\frac{\xi}{x\tan(\alpha/2)} - 1\right)^{l-1/2} \quad (18)$$
$$\left.\times I_{2l-1}\left(2\kappa_0\sqrt{\left(\xi - x\tan\frac{\alpha}{2}\right)x\tan\frac{\alpha}{2}}\right)\right],$$

where $H(y) = 1$ at $y \geq 0$ and $H(y) = 0$ at $y < 0$ and I_{2l-1} is an odd-order modified Bessel function. Figure 2 shows the reliefs and contour plots of $\hat{B}_1(x, \xi)$ for two values of the ratio $L_\perp/L_\parallel$ equal to 1.2 and 0.6 at the scattering angle $\alpha = \pi/2$, corresponding to side scattering. Expression (18) for the normalized amplitude of scattered radiation was earlier obtained in [9, 10], where

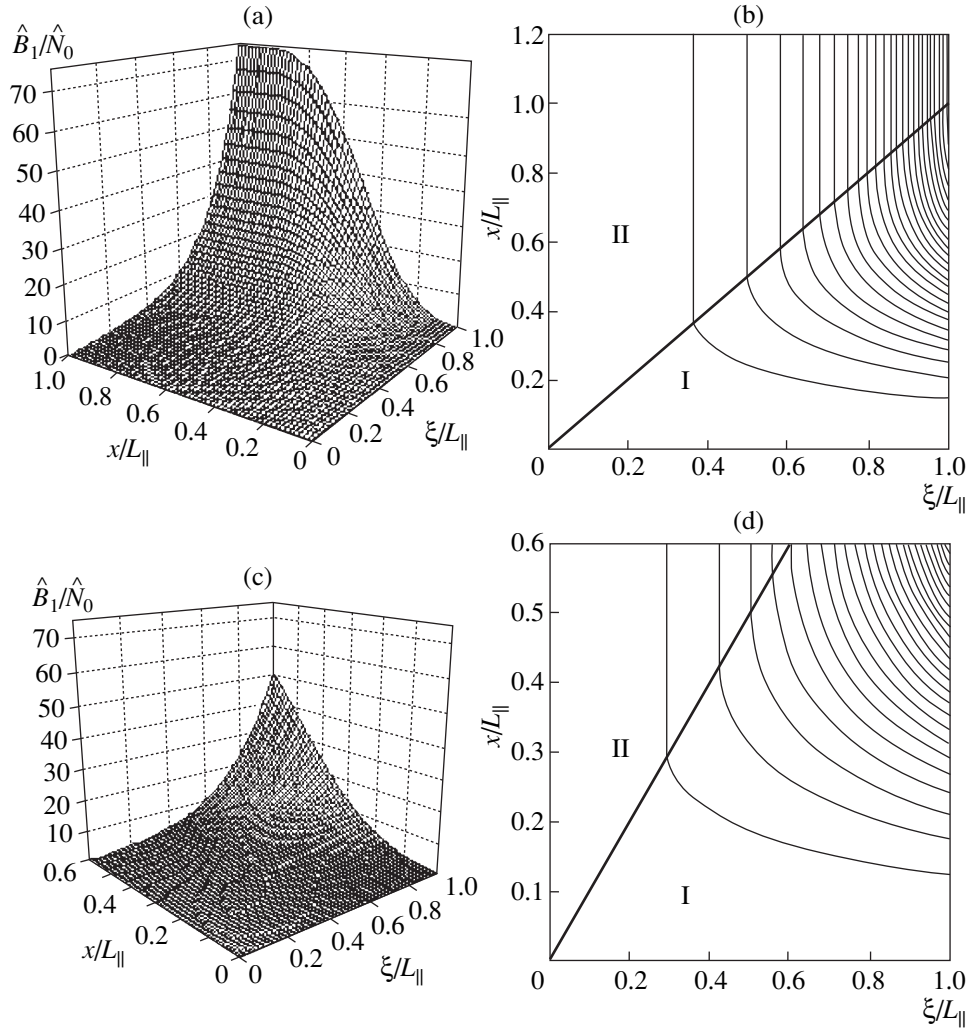

Fig. 2. Side SRS in the weak-coupling regime: (a, c) the reliefs and (b, d) contour plots of the ratio $\hat{B}_1/\hat{N}_0$ corresponding to the amplification coefficient $\kappa_0 L_\parallel = 5$ for the ratios of the transverse to longitudinal size of the pulse $L_\perp/L_\parallel$ = (a, b) 1.2 and (c, d) 0.6. In region I ($\xi > x$), two-dimensional amplification takes place. In region II ($\xi < x$), amplification is one-dimensional. The influence of the boundary condition at $x = 0$ reduces the growth rate of perturbations in region I. The maximum possible amplification coefficient at $\xi = L_\parallel$ is not achieved if $L_\perp/L_\parallel < \cot(\alpha/2) = 1$ (c, d).

the spatiotemporal linear theory of a large-angle SRS of a short laser pulse with finite transverse dimensions was developed. Amplitude (18) corresponds to the steady-state regime of convective amplification in a two-dimensional region. This steady-state solution is established in a time of $\tau_0 = \max\{L_\parallel/c, L_\parallel/[2c\sin^2(\alpha/2)]\}$ after the pulse has entered the plasma.

When solving Eqs. (12) and (13), describing the SRS instability in the strong-coupling regime, it is convenient to introduce the normalized amplitude of scattered radiation in the form $B_1(x, \xi) = -3\sqrt{2}\sin(\alpha/2)(G_0/k_p)^{-1/2}A_1(x, \xi)$, where $G_0 = [(a_0/2)^2 k_p^2 k_0]^{1/3}$. The Laplace transform of the normalized amplitude is

$$B_1(x, s) = 3i\frac{N_0 G_0 s}{s^3 - iG_0^3} \times\left\{1 - \exp\left[-\left(s - \frac{iG_0^3}{s^2}\right)x\tan\frac{\alpha}{2}\right]\right\}. \quad (19)$$

The quantity $K_0 = (\sqrt{3}/2)G_0$ is the familiar spatial growth rate of the convective instability associated with large-angle SRS in the comoving frame of reference in the strong-coupling regime [11, 16]. The normalized amplitude $B_1(x, \xi)$ obtained by inverting Laplace trans-

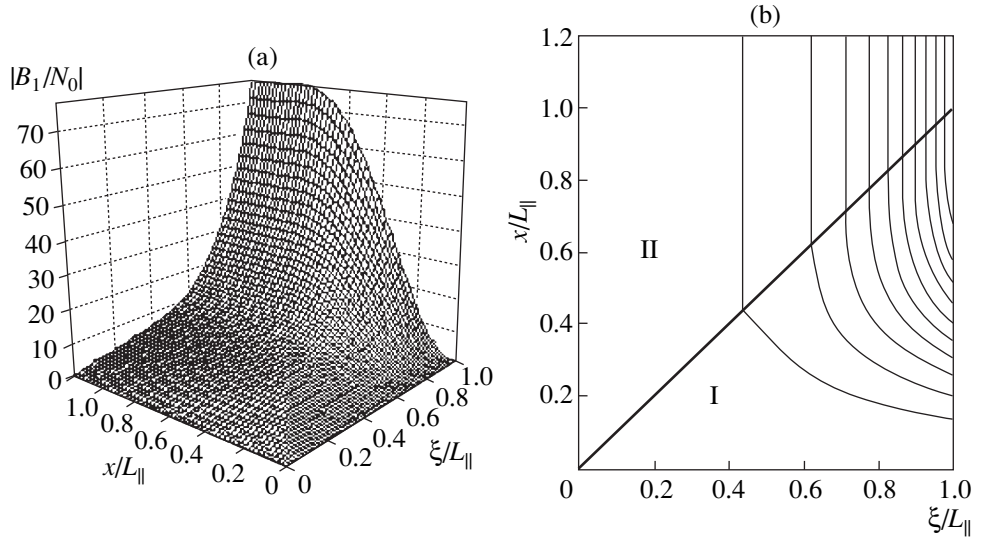

Fig. 3. Side SRS in the strong-coupling regime: (a) the relief and (b) contour plot of $|B_1/N_0|$ corresponding to the amplification coefficient $K_0L_\parallel = 5\sqrt{3}/2$ for the ratio of the transverse to longitudinal size of the pulse $L_\perp/L_\parallel = 1.2$. As in Fig. 2, in region I ($\xi > x$), two-dimensional amplification takes place, whereas in region II ($\xi < x$), amplification is one-dimensional. The influence of the boundary condition $B_1(\xi, x = 0) \equiv 0$ reduces the growth rate of perturbations in region I as compared to region II.

form (19) has the form

$$B_1(x, \xi) = N_0 \sum_{j=1}^{3} c_j^2 \exp(c_j G_0 \xi)$$

$$\times \left[1 - H\left(\xi - x\tan\frac{\alpha}{2}\right)\exp\left(-c_j G_0 x \tan\frac{\alpha}{2}\right) \right. \qquad (20)$$

$$\left. \times \sum_{l=0}^{\infty} \frac{\left(c_j G_0 x \tan\frac{\alpha}{2}\right)^l}{(2l)!\,l!} \gamma\left(2l+1,\, c_j G_0 \left[\xi - x\tan\frac{\alpha}{2}\right]\right) \right],$$

where

$$\gamma(\beta, z) = z^\beta \sum_{s=0}^{\infty} \frac{(-z)^s}{s!(\beta + s)}$$

is the incomplete gamma-function [17] and c_j are the roots of the equation $c_j^3 = i$. Figure 3 shows the relief and contour plot of $|B_1(x, \xi)|$ for $L_\perp/L_\parallel = 1.2$ and $\alpha = \pi/2$.

In the region where the solution is affected by the boundary condition at $x = 0$ (this region is bounded by the characteristics $\xi = x\tan(\alpha/2)$ and $x = 0$ and is designated as region I in Figs. 1–3), the amplitude of scattered radiation shows a two-dimensional behavior: the solution monotonically increases along both the x- and ξ-axes. In region II, solutions (18) and (20) are completely determined by the boundary condition at the leading edge of the pulse; in this region, the solution depends only on the longitudinal coordinate and increases as $\propto\{\exp(\kappa_0\xi), \exp(K_0\xi)\}$ with the growth rate κ_0 or K_0, which is independent of the scattering angle. A correction suppressing the exponential growth of the amplitude of scattered radiation in region I [see expressions (18) and (20)] appears because the solutions must satisfy the boundary condition $\{\hat{B}_1, B_1\}(x = 0, \xi) \equiv 0$.

For a sufficiently large focal-spot size $L_\perp$ or for near-backward scattering ($\alpha \approx \pi$), when the inequality $L_\perp \gg \cot(\alpha/2)L_\parallel$ is satisfied, the one-dimensional regime of amplification dominates in almost the entire interaction region. In this case, the contribution of the boundary effects on scattering is insignificant (see also the remark at the end of Section 3.2.1) and the influence of the boundary conditions at the side boundaries of the pulse can be neglected. (Note that, in [16], the problem of large-angle SRS in the presence of long-wavelength perturbations of the electron density was solved just in this approximation.) In the opposite case, i.e., at $L_\perp \leq \cot(\alpha/2)L_\parallel$ (see Fig. 1b), the evolution of the decay waves is two-dimensional in the entire region occupied by the pulse.

Solutions (18) and (20) allow us to answer the question of whether the maximum possible amplification coefficient can be achieved for the given scattering angle and the given ratio of the transverse to longitudinal size of the pulse. In the interaction region, the amplitudes of the waves increase monotonically along

both the x- and ξ-axes. Hence, the amplitude of scattered radiation reaches its maximum at the trailing edge of the pulse ($\xi = L_\parallel$). The maximum amplification coefficient $\{\hat{B}_1, |B_1|\} \propto \{\exp(\kappa_0 L_\parallel), \exp(K_0 L_\parallel)\}$ is attained in the one-dimensional regime of amplification and can be achieved if at least part of the trailing edge does not fall in region I, where the solution is affected by the boundary condition at the side boundary. This takes place if the pulse dimensions satisfy the inequality (see Fig. 1b)

$$\frac{L_\perp}{L_\parallel} > \cot\left(\frac{\alpha}{2}\right). \tag{21}$$

If the opposite inequality is satisfied, then the finite transverse size of the pulse significantly reduces the amplitude of scattered radiation (cf. Figs. 2a and 2b).

Above, we have studied steady-state solutions (18) and (20) in the comoving frame of reference in the weak- and strong-coupling regimes. Below, we will show that the solutions to the initial–boundary problem for Eqs. (8) and (9) or (12) and (13) with the initial and boundary conditions (10) and (11) or (14) and (16), respectively, arrive at the steady-state solutions obtained as $t \longrightarrow \infty$. The initial–boundary problem is solved by the double Laplace transformation in the time t and the longitudinal coordinate ξ (the corresponding variables in the Laplace transforms are p and s, respectively). The Laplace transforms of the normalized amplitudes $\hat{B}_1(t, x, \xi)$ (weak coupling) and $B_1(t, x, \xi)$ (strong coupling) are

$$\hat{B}_1(p, x, s) = \frac{\hat{N}_0 \kappa_0/(ps)}{\dfrac{p}{2c\sin^2(\alpha/2)} + s - \dfrac{\kappa_0^2}{(p/c) + s}} \times \left\{1 - \exp\left[-x\tan\frac{\alpha}{2}\left(\frac{p}{2c\sin^2(\alpha/2)} + s - \frac{\kappa_0^2}{(p/c) + s}\right)\right]\right\}, \tag{22}$$

$$B_1(p, x, s) = \frac{3iN_0 G_0/(ps)}{\dfrac{p}{2c\sin^2(\alpha/2)} + s - \dfrac{iG_0^3}{[(p/c) + s]^2}} \times \left\{1 - \exp\left[-x\tan\frac{\alpha}{2}\left(\frac{p}{2c\sin^2(\alpha/2)} + s - \frac{iG_0^3}{[(p/c) + s]^2}\right)\right]\right\}, \tag{23}$$

respectively. To examine the functions $\hat{B}_1(t, x, \xi)$ and $B_1(t, x, \xi)$ at $t \longrightarrow \infty$, we consider the expressions $\lim p\hat{B}_1(p, x, s)$ and $\lim pB_1(p, x, s)$ at $p \longrightarrow 0$. Passing over to the limit $p \longrightarrow 0$ (at $\alpha \neq 0$) in expressions (22) and (23), we obtain formulas (17) and (19), respectively. It follows from here that, at $t \longrightarrow \infty$, the interacting waves arrive at the steady-state regime described by formulas (18) or (20). This is formally true for arbitrary small scattering angles, excluding $\alpha = 0$. To verify that there is no asymptotic steady-state solutions for interacting waves in the case of direct-forward scattering, we return to the dimensional amplitudes $\hat{a}_s(p, x, s) = -i(\omega_{pe}/2\omega_0)^{3/2}\sin^{-2}(\alpha/2)\,\hat{B}_1(p, x, s)$ (weak coupling) and $a_s(p, x, s) = -(1/6)(\omega_{pe}/2\omega_0)^{4/3} \times a_0^{1/3}\sin^{-2}(\alpha/2)B_1(p, x, s)$ (strong coupling) and pass over to the limit $\alpha \longrightarrow 0$ taking into account expressions (22) and (23). As a result, we obtain the expression

$$\lim_{a \to 0}\{\hat{a}_s, a_s\}(p, x, s) = \frac{\omega_{pe}^2}{4i\omega_0}\{\hat{N}_0, N_0\}a_0\frac{1}{p^2 s}, \tag{24}$$

from which it follows that the limit $\lim_{p \to 0} p\{\hat{a}_s, a_s\}$ is absent. This means that there is no steady state for the case of direct-forward scattering, which agrees with the familiar results for the direct-forward SRS [13].

3.2. Applicability Conditions of Two-Dimensional Steady-State Solutions

The explicit solutions (18) and (20) to the time-independent boundary problem correctly describe SRS only within the applicability limits of the model based on the reduced equations (8) and (9) or (12) and (13), respectively. In particular, condition (6), which allows us to reduce the order of the equation for the scattered-field envelope with respect to the variable x, must be satisfied. Obviously, this condition can be violated for scattering angles close to either π (near-backward scattering) or zero (near-forward scattering). Below, we will determine the range of scattering angles in which the steady-state regime of convective amplification of perturbations in the course of SRS is correctly described by the solutions to the boundary problem for the reduced equations.

3.2.1. Near-backward scattering ($\alpha \approx \pi$). As the scattering angle tends to π, the characteristic $x = \xi\cot(\alpha/2)$ tends to $x = 0$. As a result, region I, in which the solution is affected by the boundary condition at $x = 0$, becomes progressively narrower; correspondingly, the absolute value of the x-derivative of the solution to the boundary problem increases and becomes infinite at $\alpha = \pi$, when the amplitude of scattered radiation, determined by expressions (18) or (20), undergoes a discontinuity at the boundary $x = 0$. In order to estimate the characteristic value of the transverse derivative of the envelope of scattered radiation in region I, we approximate the x profile of the envelope at the given ξ by a linear function: $a_s(x, \xi) = (x/\xi)\tan(\alpha/2)a_s(\xi, x = \xi\cot(\alpha/2))$. We substitute this approximation into condition (6) to obtain the upper estimate for the range of

scattering angles in which expressions (18) and (20) are formally valid. As a result, we obtain

$$\pi - \alpha > \left(\frac{2}{k_0 L_\parallel}\right)^{1/2}. \quad (25)$$

Note that the transverse derivative $\partial a_s/\partial x$ obtained from the linear approximation gives a somewhat underestimated value of the derivative compared to its maximum value in region I. However, this fact is of minor importance, and the upper estimate (25) for the range of admissible scattering angles remains valid in order of magnitude. For example, in the weak-coupling regime, substituting the exact maximum value of $\partial a_s/\partial x$ obtained from the explicit solution (18) into condition (6) gives the inequality $\pi - \alpha > 2(k_0 L_\parallel)^{-1/2}(\pi\kappa_0 L_\parallel/2)^{-1/4}$, where $\kappa_0 L_\parallel$ is the maximum achievable amplification coefficient for the scattering at the angle α. Under the applicability conditions of the linear theory, this coefficient is not too large, $\kappa_0 L_\parallel \sim 10$–$20$, from which we obtain $(\pi\kappa_0 L_\parallel/2)^{-1/4} \sim 0.5$. Hence, the use of condition (25) as the order-of-magnitude estimate is well justified.

If condition (25) is violated, expressions (18) or (20) fail to describe the scattered-field envelope in region I (in fact, in the boundary layer of width $l_b \approx [L_\parallel/(2k_0)]^{1/2}$). To correctly describe the boundary effects, it is necessary to take into account the secondary derivative with respect to the transverse coordinate and to correctly specify the pulse shape, which must correspond to the smooth vanishing of the pulse amplitude at the side boundary. At the same time, in region II, solutions (18) and (20) are independent of the boundary conditions at the side boundary ($x = 0$) of the pulse and condition (6) is satisfied throughout this region. Therefore, at $\pi - (k_0 L_\parallel/2)^{-1/2} < \alpha \le \pi$, the applicability of the solutions obtained is only violated in a narrow boundary layer of width $l_b \ll L_\perp$, whereas in most of the region occupied by the pulse ($l_b < x \le L_\perp$, $0 \le \xi \le L_\parallel$), these solutions correctly describe the envelope of scattered radiation.

3.2.2. Small-angle scattering ($\alpha \approx 0$). As the scattering angle formally tends to zero, the characteristic $\xi = x\tan(\alpha/2)$ tends to the vertical line $\xi = 0$ and the region in which the solution is affected by the boundary condition at $x = 0$ extends over the entire region occupied by the pulse. At $\alpha \ll 2\arctan(\xi/x)$, the asymptotic behavior of solutions (18) and (20) at a given point (x, ξ) inside the pulse is described by the formulas

$$\hat{B}_1(x, \xi, \alpha \ll 2\arctan(\xi/x)) \sim \frac{x\alpha}{2}\hat{N}_0\kappa_0, \quad (26)$$

$$B_1(x, \xi, \alpha \ll 2\arctan(\xi/x))$$

$$\sim \frac{x\alpha}{4}\left[iN_0 G_0 \sum_{j=1}^{3} \exp(c_j G_0 \xi)[2 - \gamma(3, c_j G_0 \xi)]\right], \quad (27)$$

respectively. At $\alpha \ll 2\arctan(\xi/x)$, condition (6) with allowance for formulas (26) and (27) leads to the inequality $\sin\alpha \approx \alpha \gg (k_0 x)^{-1}$. If this inequality is violated in the entire interaction region (i.e., at $0 \le x \le L_\perp$), then we cannot examine the instability within the framework of Eqs. (8) and (9) or (12) and (13) and must use the more general initial set of equations (3) and (4), which contain the second derivatives with respect to the transverse coordinate.

As was shown in [14], where equations similar to Eqs. (3) and (4) were used to describe the three-dimensional instability of a laser pulse with respect to transverse perturbations of the envelope with a characteristic scale length of $L_\perp$ (i.e., $k_{s_\perp}^{-1} \sim L_\perp$), taking into account the higher spatial derivatives leads to the absolute instability of the pulse amplitude in the comoving frame of reference. Thus, we obtain the lower limit for the admissible scattering angles: $\alpha \gg (k_0 L_\perp)^{-1}$. For lower scattering angles, our results become invalid. Moreover, when estimating the lower limit for scattering angles for which the interacting waves arrive at a steady state in the comoving frame, we must take into account the finite duration of the pulse propagation in a plasma. Assuming that the characteristic length of a plasma produced in the laser focal region is on the order of the Rayleigh length r_R, we compare the propagation time of the pulse in the plasma $\tau_R = r_R/c$ with the characteristic time $\tau_0 = L_\parallel/[2c\sin^2(\alpha/2)]$ required for the steady-state solution describing a small-angle SRS in the comoving frame to be established [9, 10]. Under the condition $\tau_0 < \tau_R$ (from which we obtain $\alpha > 2(L_\parallel/L_\perp)^{1/2}(k_0 L_\perp)^{-1/2}$), the propagation time is sufficient for the steady-state solution in the comoving frame to be established. Therefore, in order for the steady-state regime of two-dimensional spatial amplification of perturbations arising due to a small-angle SRS can be established in the comoving frame of reference and we can describe this steady state in terms of solutions (18) or (20) to the boundary problem for the reduced equations (8) and (9) or (12) or (13), respectively, the scattering angles must satisfy the inequality

$$\alpha > \max\left\{\frac{1}{k_0 L_\perp}, \left(\frac{L_\parallel}{L_\perp}\right)^{1/2}\frac{2}{(k_0 L_\perp)^{1/2}}\right\}.$$

Summarizing the obtained results concerning the applicability of the steady-state solutions (18) or (20) to the boundary problems for Eqs. (8) and (9) or (12) and (13), respectively, in the entire region occupied by the laser pulse, we can state the following.

In the range

$$\max\left\{\frac{1}{k_0 L_\perp}, \left(\frac{L_\parallel}{L_\perp}\right)^{1/2}\frac{2}{(k_0 L_\perp)^{1/2}}\right\} < \alpha < \pi - \left(\frac{2}{k_0 L_\parallel}\right)^{1/2}, \quad (28)$$

expressions (18) and (20) correctly describe the amplitude of scattered radiation in the comoving frame of reference in the steady-state regime of two-dimensional convective amplification in the region occupied by the pulse.

For

$$\pi - \left(\frac{2}{k_0 L_\parallel}\right)^{1/2} < \alpha \le \pi,$$

solutions (18) and (20) become invalid in region I, where they are affected by the boundary conditions at the side boundary of the pulse $x = 0$, whereas in region II, the amplitude of scattered radiation is correctly described by expressions (18) and (20).

For

$$0 \le \alpha < \max\left\{\frac{1}{k_0 L_\perp}, \left(\frac{L_\parallel}{L_\perp}\right)^{1/2} \frac{2}{(k_0 L_\perp)^{1/2}}\right\},$$

solutions (18) and (20) are inapplicable in the entire region occupied by the pulse.

4. CONCLUSION

In this paper, we have examined the steady-state (in the comoving frame of reference) regime of amplification of the perturbations arising due to an SRS at angles satisfying condition (28) in the two-dimensional region in which the pump field is localized. It is established that the amplification of unstable modes in the comoving frame is two-dimensional in nature. It is shown that the finite transverse dimensions of the laser pulse can limit the coefficient of convective amplification. It is found that, in order for the maximum possible (in linear theory) amplification coefficient to be achieved for SRS at the given angle α, the ratio of the transverse to longitudinal size of the pulse must satisfy the inequality $L_\perp/L_\parallel > \cot(\alpha/2)$.

ACKNOWLEDGMENTS

This work was supported by the Russian Foundation for Basic Research, project no. 98-02-16263.

REFERENCES

1. G. G. Comisar, Phys. Rev. **141**, 200 (1966); N. Bloembergen and Y. R. Chen, Phys. Rev. **141**, 298 (1966); M. V. Goldman and D. F. du Bois, Phys. Fluids **8**, 1404 (1965); N. E. Andreev, Zh. Éksp. Teor. Fiz. **59**, 2105 (1970) [Sov. Phys. JETP **32**, 1141 (1971)].
2. V. P. Silin, *Parametric Action of High-Power Radiation on a Plasma* (Nauka, Moscow, 1973), p. 149.
3. G. Mourou and D. Umstadter, Phys. Fluids B **4**, 2315 (1992); J. P. Watteau, G. Bonnaud, J. Coutant, *et al.*, Phys. Fluids B **4**, 2217 (1992).
4. D. W. Forslund, J. M. Kindel, and E. L. Lindman, Phys. Fluids **18**, 1002 (1975); **18**, 1017 (1975).
5. E. Esarey, P. Sprangle, J. Krall, and A. Ting, IEEE Trans. Plasma Sci. **24**, 252 (1996).
6. C. B. Darrow, C. Coverdale, M. D. Perry, *et al.*, Phys. Rev. Lett. **69**, 442 (1992).
7. T. M. Antonsen, Jr. and P. Mora, Phys. Fluids B **5**, 1440 (1993).
8. N. M. Kroll, J. Appl. Phys. **36**, 34 (1965); D. L. Bobroff and H. A. Haus, J. Appl. Phys. **38**, 390 (1967); L. M. Gorbunov and D. K. Salikhov, Fiz. Plazmy **10**, 824 (1984) [Sov. J. Plasma Phys. **10**, 478 (1984)].
9. C. J. McKinstrie, R. Betti, R. E. Giacone, *et al.*, Phys. Rev. E **51**, 3752 (1995).
10. C. J. McKinstrie and E. J. Turano, Phys. Plasmas **4**, 3347 (1997).
11. N. E. Andreev, V. I. Kirsanov, and L. M. Gorbunov, Phys. Plasmas **2**, 2573 (1995).
12. A. S. Sakharov, Fiz. Plazmy **26**, 700 (2000) [Plasma Phys. Rep. **26**, 657 (2000)].
13. A. S. Sakharov and V. I. Kirsanov, Phys. Rev. E **49**, 3274 (1994); W. B. Mori, C. D. Decker, D. E. Hinkel, and T. Katsouleas, Phys. Rev. Lett. **72**, 1482 (1994); C. J. McKinstrie and E. J. Turano, Phys. Plasmas **3**, 4683 (1996).
14. N. E. Andreev, V. I. Kirsanov, L. M. Gorbunov, and A. S. Sakharov, IEEE Trans. Plasma Sci. **24**, 363 (1996); N. E. Andreev, L. M. Gorbunov, V. I. Kirsanov, and A. S. Sakharov, Fiz. Plazmy **22**, 419 (1996) [Plasma Phys. Rep. **22**, 379 (1996)].
15. N. E. Andreev and S. Yu. Kalmykov, Proc. SPIE **2770**, 53 (1996).
16. N. E. Andreev and S. Yu. Kalmykov, IEEE Trans. Plasma Sci. **PS-28** (4) (2000).
17. F. W. J. Olver, *Asymptotics and Special Functions* (Academic, New York, 1974; Nauka, Moscow, 1990).

Translated by A. Sakharov

Plasma Physics Reports, Vol. 26, No. 11, 2000, pp. 947–959. Translated from Fizika Plazmy, Vol. 26, No. 11, 2000, pp. 1010–1023.

NONLINEAR PHENOMENA

Generation of a Wakefield during Gas Ionization

N. E. Andreev, M. E. Veĭsman, M. G. Cadjan, and M. V. Chegotov

Institute for High Energy Densities, Associated Institute for High Temperatures, Russian Academy of Sciences, Izhorskaya ul. 13/19, Moscow, 127412 Russia

Received December 27, 1999; in final form, March 27, 2000

Abstract—One-dimensional equations are derived that describe the hydrodynamic and electrodynamic properties of a plasma created through gas ionization by a short intense laser pulse. Different approaches (in particular, the particle-in-cell method) are used to show that, with ionization processes included, the excitation of a wakefield by an intense laser pulse can be described by the method of slowly varying amplitudes. It is shown that ionization processes enhance the wakefield excited by a moderate-intensity laser by about 10% in the case of a linearly polarized laser and by about 50% in the case of a circularly polarized laser. Ionization processes in light gases irradiated with high-intensity laser pulses have essentially no effect on the wakefield during the resonant excitation of a plasma wave by the ponderomotive force and play a governing role far from the resonance. © *2000 MAIK "Nauka/Interperiodica".*

1. INTRODUCTION

The progress achieved over the past decade in the creation of compact devices generating intense femtosecond laser pulses (so-called T^3 systems) has made it possible to substantially extend the area of theoretical and experimental research on the interaction of highly localized (in both space and time) intense electromagnetic fields with matter (see, e.g., [1]). Thus, combining the high intensity of laser pulses with a properly adjusted pulse duration provides the possibility of generating a large-amplitude wake plasma wave [2, 3], which can be employed in modern-day laser wakefield accelerators (plasma-based electron acceleration schemes) [4].

The theory of wakefield excitation by short laser pulses in fully ionized homogeneous plasmas and in preformed plasma density channels has been developed in considerable detail [5–12] (see also reviews [13, 14] and the literature cited therein). However, the theory of the propagation of high-intensity laser pulses in a matter whose charge content changes due to ionization by intense optical radiation requires further development. In particular, the ionization of matter by laser pulses not only may give rise to radiation energy losses but may also seriously distort the incident laser pulse shape on the particle-acceleration time scale [15, 16] and provide conditions for optical guiding by preformed plasma channels [17].

Our purpose here is to analyze how ionization processes affect the wakefield excitation by a laser pulse in a gas. The generation of plasma waves by laser pulses with allowance for ionization processes was studied in [18, 19]. Mori and Katsouleas [18] applied the single particle model to determine the ponderomotive force that excites a plasma wave during ionization. However, in deriving the expression for the ponderomotive force (see formula (15) in [18]), they neglected the fact that the growth rate of the electron density due to ionization contains oscillations at the harmonics of the laser field frequency (see relation (13) in [18]) because of the strongly nonlinear dependence of the ionization probability on the laser field intensity. Moreover, the expression for the ponderomotive force obtained in [18] contained such parameters as the phase ϕ and amplitude E of the ionizing electric field, which remained undetermined. As a result, Mori and Katsouleas [18] described the effect of ionization processes on the amplitude of the wake plasma wave by the phenomenological expression with two undetermined parameters. The approach developed by Fisher and Tajima [19] was also phenomenological, with undetermined main parameters that governed the contribution of ionization processes to the wakefield amplitude.

Below, we apply the kinetic and hydrodynamic equations that describe the relativistic dynamics of the interaction of intense laser fields with plasma and systematically take into account ionization processes (cf. [20]) in order to study the excitation of a wake plasma wave by an intense laser pulse. Since the irradiation of a gas by a short laser pulse is usually characterized by the inequality $\gamma < 1$, where γ is the Keldysh parameter [21], the plasma production can be examined using the tunneling-ionization model. In this way, we can turn to the so-called "two-stage" model, in which the transition of an electron from the bound state to the state of free motion is described by the methods of quantum mechanics in the spirit of the theory of tunneling ionization, and the dynamics of the free electrons themselves in the laser field is described by the classical equations of motion [22, 23]. Recently, this approach has been used to study nonadiabatic gas heating by intense laser pulses [20, 24]. In our paper, the two-stage model is used to investigate the characteristic features

1063-780X/00/2611-0947$20.00

of the wakefield excitation with allowance for ionization processes.

Using the one-dimensional approximation, we compare the results obtained by the following three approaches: the most complete numerical investigation based on particle-in-cell (PIC) simulations; numerical solution of the set of equations consisting of the Maxwell equations and the hydrodynamic equations for an electron fluid, which are derived from the kinetic equation by the method of moments; and numerical and analytical solution of the equation for the wakefield amplitude, which is derived from the Maxwell equations and hydrodynamic equations by averaging over time.

We demonstrate that the results of the hydrodynamic calculations based on the full set of equations and the results obtained by analytically solving the reduced equation for the wakefield amplitude both agree well with the kinetic PIC simulation results.

2. BASIC EQUATIONS

We describe the ionization process and free electron motion in the field of a short high-power laser pulse by the hydrodynamic equations. We incorporate ionization into the basic equations through the standard procedure of deriving hydrodynamic equations from the kinetic equation for the momentum electron distribution function $f(\mathbf{r}, \mathbf{p}, t)$:

$$\frac{\partial f}{\partial t} + (\mathbf{v}\cdot\nabla) f + e\left(\mathbf{E} + \frac{1}{c}\mathbf{v}\times\mathbf{B}\right)\cdot\frac{\partial f}{\partial \mathbf{p}} = \Gamma(\mathbf{r}, t)\delta(\mathbf{p}), \quad (1)$$

where $\mathbf{E}$ and $\mathbf{B}$ are the electric and magnetic fields in a plasma. The term $\Gamma(\mathbf{r}, t)\delta(\mathbf{p})$ describes the source of the electrons produced during ionization by a strong electromagnetic field. The atoms (or ions) are ionized by the field of a short (with a duration τ_p of about 100 fs or shorter) high-power laser pulse via the tunneling mechanism, because the Keldysh parameter $\gamma = \omega\sqrt{2m_e U}/|e|E$ (where ω is the laser frequency, U is the ionization potential of an atom (or ion), and $m_e(e)$ and e are the mass and charge of an electron) is comparatively small (about unity or smaller) [21]. In this case, we can assume that the initial velocity of free electrons produced during such an ionization process is zero [22, 23, 25]. For this reason, the ionization term in Eq. (1) is proportional to $\delta(\mathbf{p})$. Note that, in order to study the distribution function of the electrons that are ejected out of the atoms during tunneling ionization, Tikhonchuk and Bychenkov [26] incorporated ionization processes into the kinetic equation through the source term of the form $\Gamma(\mathbf{r}, t)\delta(\mathbf{p})$. More recently, an analogous approach was applied in [20, 27] to the kinetic equation in order to derive the hydrodynamic equations describing gas ionization.

In Eq. (1), we neglected recombination and both elastic and inelastic collision processes (electron–neutral, electron–ion, and electron–electron collisions) because, in a moderately dense plasma, these processes occur on time scales far longer than the characteristic time scales of our problem, i.e., the pulse duration and the plasma period, which is approximately the pulse duration or shorter (see below). In fact, if the neutral atom density is about 10^{19} cm^{-3} or lower and the electron velocity is about $\sim 10^{10}$ cm/s (which is close to the speed of light), then even for a collision cross section of about $\sigma \sim 10^{-16}$ cm^2 the time interval between successive non-Coulomb collisions is approximately equal to 100 fs, which is comparable with the pulse duration. However, for such electron velocities, the collision cross section is much lower: $\sigma \ll 10^{-16}$ cm^2 [28]. During a short high-power laser pulse, Coulomb collisions between electrons and ions can definitely be neglected, because, first, the relative velocities of colliding particles are high [29] and, second, the electron–electron collision time is longer than 100 fs even for electron temperatures of about several electronvolts [20]. We can also ignore recombination processes because the recombination time is estimated to be much longer than the pulse duration (see, e.g., [28]).

We integrate Eq. (1) over momenta to obtain the equation for the electron density $n_e(\mathbf{r}, t) \equiv \int d^3\mathbf{p} f(\mathbf{r}, \mathbf{p}, t)$:

$$\frac{\partial n_e}{\partial t} + \mathrm{div}(n_e \mathbf{V}_e) = \Gamma, \quad (2)$$

where $\mathbf{V}_e(\mathbf{r}, t) \equiv n_e^{-1}(\mathbf{r}, t)\int d^3\mathbf{p}\mathbf{v} f(\mathbf{r}, \mathbf{p}, t)$ is the mean directed electron velocity. Integrating Eq. (1) multiplied by $\mathbf{p}$ over $\mathbf{p}$ and using Eq. (2), we arrive at the equation for the mean momentum $\mathbf{P}_e(\mathbf{r}, t) \equiv n_e^{-1}(\mathbf{r}, t)\int \mathbf{p} f(r, p, t) d^3\mathbf{p}$:

$$\frac{\partial \mathbf{P}_e}{\partial t} + (\mathbf{V}_e\cdot\nabla)\mathbf{P}_e + \frac{\Gamma}{n_e}\mathbf{P}_e = e\left(\mathbf{E} + \frac{1}{c}\mathbf{V}_e\times\mathbf{B}\right). \quad (3)$$

In deriving Eq. (3), we neglected the pressure force $n_e^{-1}\partial\Pi_{ij}/\partial r_j$ (where $\Pi_{ij} = \int (v_j - V_{e,j})(p_i - P_{e,i}) f d^3\mathbf{p}$ is the pressure tensor) in comparison with the ponderomotive force that acts on the electron fluid and is described by the second term on the left-hand side of Eq. (3) and by its right-hand side. Recall that, during gas ionization by a short laser pulse, we can actually ignore electron–neutral and electron–ion collisions, in which case the energy of the electrons in the ionized gas (the so-called residual electron energy [22, 20, 24]) is governed by their nonadiabatic interaction with the laser field at the instants at which they are ejected out of the atom rather than by inverse bremsstrahlung. Although the residual electron energy may be significant, we can readily show that, at least in the one-dimensional approximation discussed below, it does not contribute to the pressure force, because the ionization-produced electrons preferentially move transverse to the propagation direction of the laser pulse (see Sec-

tion 4).[1] On the other hand, in the one-dimensional approximation, the ionized gas is inhomogeneous only in the propagation direction of the pulse, so that the derivative of the pressure tensor, which is mainly governed by the residual electron energy, equals zero.

The hydrodynamic equations (2) and (3) contain the source term Γ, which characterizes the rate at which free electrons originate per unit volume. To determine Γ, we must calculate the rate at which the electrons are ejected out of all atomic shells:

$$\Gamma = \sum_{m=0}^{Z-1} W_m N_m \equiv \sum_{m=0}^{Z-1} \Gamma^{\langle m \rangle}, \tag{4}$$

where $\Gamma^{\langle m \rangle} \equiv N_m W_m$, W_m is the probability of the tunneling ionization of an ion in the mth ionization state per unit time ($m = 0$ corresponds to a neutral atom), $N_m(N_0)$ is the density of such ions, and N_0 is the density of neutral atoms. The probability W_m is described by the familiar Ammosov–Delone–Kraĭnov formula, which is not averaged over the pulse period [30, 31]:

$$W_m(E) = \omega_{\text{at}} \frac{\exp(1)}{2\pi} \frac{(m+1)^2}{M_m^4} \times \left[4\exp(1) \frac{(m+1)^3}{M_m^4} \frac{E_{\text{at}}}{E} \right]^{2M_m - 1} \exp\left(-\frac{2}{3} \frac{(m+1)^3}{M_m^3} \frac{E_{\text{at}}}{E} \right), \tag{5}$$

where $E_{\text{at}} = 5.142 \times 10^9$ V/cm, $E \equiv |\mathbf{E}|$ is the instantaneous electric field amplitude, $M_m = (m+1)\sqrt{13.606/U_m}$, the ionization potential U_m of an ion in the mth ionization state is measured in eV, and $\omega_{\text{at}} = 4.134 \times 10^{16}$ s^{-1} is the atomic frequency. The time evolution of the densities N_m of atoms and ions, which are both assumed to be immobile, can be described by the equations [32, 33]

$$\frac{\partial N_m}{\partial t} = -W_m N_m + W_{m-1} N_{m-1}, \quad m = 1, \ldots, Z-1,$$
$$\frac{\partial N_Z}{\partial t} = W_{Z-1} N_{Z-1}, \quad N_0 = N_{\text{at}} - \sum_{m=1}^{Z} N_m, \tag{6}$$

where Z is the nuclear charge of an atom and $N_{\text{at}} = \text{const}$ is the net density of the gas atoms and ions. Solving Eqs. (6) at a fixed laser field amplitude E yields the time dependence of Γ. Figure 1 shows that the time evolution $\Gamma(t)$ is smooth in the case of a circularly polarized pulse and experiences rapid oscillations [34] in the case of a linearly polarized pulse, the oscillation period being equal to one-half of the laser field period. The envelope of $\Gamma(t)$ is characterized by a sequence of peaks corresponding to ionization of ions in the corresponding ionization states. The peak widths along the time axis, τ_{ion}, which can be regarded as characteristic time scales on which ions in the corresponding ionization states are ionized, are approximately equal to several laser field periods. Such short ionization time scales allow us, in particular, to speak of the threshold intensity $I_{\text{th}}^{(m)}$ for the ionization of an ion in the mth ionization state.

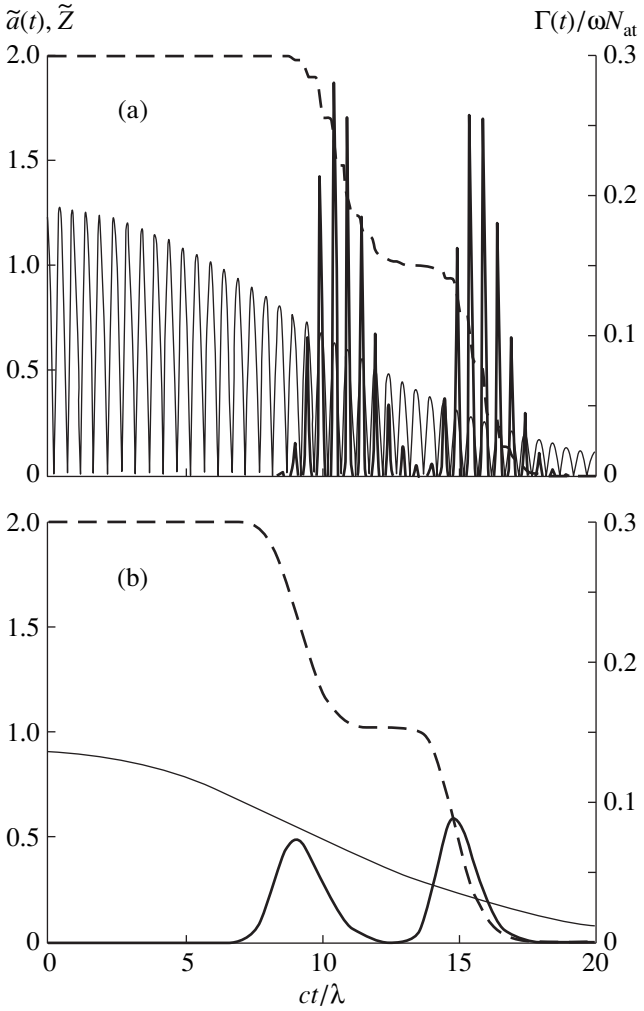

Fig. 1. Source term $\Gamma(t)/(\omega N_{\text{at}})$ (heavy solid curves) for the electrons originating during the ionization of helium atoms by a Gaussian laser pulse with the peak intensity $I_{\max} = 5 \times 10^{16}$ W/cm^2, full width at half-maximum $\tau_p = 50$ fs, and wavelength $\lambda = 0.8$ μm. The zero time corresponds to the pulse center. The light solid curves show the absolute value of the dimensionless laser field amplitude $\tilde{a}(t) = e|\mathbf{E}(t)|/(m_e \omega c)$, where the field amplitude is related to the laser intensity I_l by $\langle \mathbf{E}^2(t) \rangle = 4\pi I_l / c$ (the angular brackets stand for averaging over the laser field period). The dashed curves show the mean ion charge $\bar{Z} = n_e/N_{\text{at}}$ in the case of (a) linear and (b) circular polarization.

[1] The isotropization of the momentum electron distribution function via electron–electron and electron–neutral (ion) collisions can be neglected, because the collision times and, accordingly, the rise time of the ionization front are much longer than the pulse duration.

In the Maxwell equations and in the kinetic equation (1), we must take into account ionization processes. To do this, we must consider not only the current $\mathbf{J}$ of free electrons but also the current $\mathbf{J}_{\text{ion}}$ driven by the polarization of atoms ionized by the laser field [35]. To determine the current $\mathbf{J}_{\text{ion}}$, we take into account the fact that, because of the direct ionization of gas atoms by an electromagnetic field with the wave vector $\mathbf{k}$ and frequency ω, the energy density $w_{\mathbf{k},\omega}$ of the laser radiation decreases at the rate

$$\left(\frac{\partial w_{\mathbf{k},\omega}}{\partial t}\right)_{\text{ion}} = -\sum_{m=0}^{Z-1} W_m N_m U_m, \tag{7}$$

and the momentum flux of the laser radiation, $\mathbf{S}/c^2$ (where $\mathbf{S} = (c/4\pi)\mathbf{E}\times\mathbf{B}$ is the Poynting vector), changes at the rate

$$\left(\frac{\partial}{\partial t}\frac{\mathbf{S}}{c^2}\right)_{\text{ion}} = -\sum_{m=0}^{Z-1} W_m N_m U_m \frac{\mathbf{k}}{\omega}. \tag{8}$$

The rates (7) and (8) at which the energy and momentum of the laser radiation change can be incorporated into the Maxwell equation

$$\operatorname{curl}\mathbf{B} = \frac{4\pi}{c}(\mathbf{J}+\mathbf{J}_{\text{ion}}) + \frac{1}{c}\frac{\partial \mathbf{E}}{\partial t} \tag{9}$$

by supplementing the current $\mathbf{J} = en_e\mathbf{V}_e$ of free electrons with the ionization current $\mathbf{J}_{\text{ion}}$ defined as

$$\mathbf{J}_{\text{ion}} = \frac{\mathbf{E}}{E^2}\sum_{m=0}^{Z-1} W_m N_m U_m. \tag{10}$$

In order to take into account the ionization current $\mathbf{J}_{\text{ion}}$ in Eq. (9), we must add the ionization-induced charge density ρ_{ion} to the conventional hydrodynamic density $\rho(\mathbf{r}, t) \equiv en_e + |e|\sum_{m=1}^{Z} mN_m$ of free electrons in the Maxwell equation for the electric field $\mathbf{E}$, $\operatorname{div}\mathbf{E} = 4\pi\rho + 4\pi\rho_{\text{ion}}$. In fact, Eqs. (2) and (6) with expression (4) imply that, at each instant, the charge of the free electrons is equal in magnitude to the total ion charge; therefore, the hydrodynamic free-charge density ρ and hydrodynamic current density $\mathbf{J}$ satisfy the free-charge conservation law $\partial\rho/\partial t + \operatorname{div}\mathbf{J} = 0$. Taking the divergence of Eq. (9) and using the free-charge conservation law, we arrive at the conservation law for the ionization-induced ion charge, $\partial\rho_{\text{ion}}/\partial t + \operatorname{div}\mathbf{J}_{\text{ion}} = 0$. In particular, we can see that, if $\operatorname{div}\mathbf{J}_{\text{ion}} \neq 0$, then $\rho_{\text{ion}} \neq 0$. Note that, in one-dimensional geometry, the ionization current (10), which results from gas ionization by the transverse field of the laser pulse, is purely transverse, so that we have $\operatorname{div}\mathbf{J}_{\text{ion}} = 0$ and, accordingly, $\partial\rho_{\text{ion}}/\partial t = 0$ and $\rho_{\text{ion}} = 0$. Previously, Rae and Burnett [36] introduced the current (10) on the basis of energy considerations, and then it was used in [32, 33, 27, 16]. Relationship (8) shows that using the polarization current (10) can also be justified on the basis of the momentum conservation law for a "field–matter" system during the ionization of matter by a radiation field.

Since, in the approximation of immobile ions, the Maxwell equation for the electric field $\mathbf{E}$,

$$\operatorname{curl}\operatorname{curl}\mathbf{E} + \frac{1}{c^2}\frac{\partial^2\mathbf{E}}{\partial t^2} = -\frac{4\pi}{c^2}\frac{\partial(\mathbf{J}+\mathbf{J}_{\text{ion}})}{\partial t}, \tag{11}$$

contains the electric current density $\mathbf{J} = en_e\mathbf{V}_e$ of free electrons, it is convenient to rewrite Eq. (3) in terms of $\mathbf{J}$. With the relativistic relationship between the electron momentum $\mathbf{P}_e$ and the electron velocity $\mathbf{V}_e(\mathbf{r}, t) = \mathbf{P}_e(\mathbf{r}, t)/\sqrt{m_e^2 + [\mathbf{P}_e(\mathbf{r}, t)/c]^2}$, we obtain

$$\frac{\partial\mathbf{J}}{\partial t} + \frac{1}{\rho_e}(\mathbf{J}\cdot\nabla)\mathbf{J} + \mathbf{J}\operatorname{div}\frac{\mathbf{J}}{\rho_e}$$
$$= \frac{e}{m_e}\sqrt{1-\frac{\mathbf{J}^2}{\rho_e^2c^2}}\left\{\rho_e\mathbf{E} + \frac{1}{c}\mathbf{J}\times\mathbf{B} - \frac{1}{\rho_e c^2}\mathbf{J}(\mathbf{J}\cdot\mathbf{E})\right\} \tag{12}$$
$$+ \frac{e}{\rho_e^3}\Gamma\mathbf{J}\frac{\mathbf{J}^2}{c^2},$$

where $\rho_e \equiv en_e$ is the charge density of free electrons.

3. WAKEFIELD EXCITATION IN ONE-DIMENSIONAL GEOMETRY

In order to clarify the main effect of optical ionization on the longitudinal electric field of a wake plasma wave excited by a short laser pulse, we treat the problem in one-dimensional geometry, in which case all of the quantities depend solely on the spatial variable x in the propagation direction of the laser pulse. The longitudinal component E_x of the electric field of the wake wave driven by a laser pulse in a plasma turns out to be potential and satisfies the equation

$$\frac{\partial E_x}{\partial t} = -4\pi J_x. \tag{13}$$

Recall that the source term Γ in Eqs. (2), (3), and (12) is nonzero only over short time intervals corresponding to ionization of ions in the corresponding ionization state (Fig. 1). The laser intensity required to further ionize ions with a comparatively low ionization energy is far below the relativistic intensity, which is about 10^{18} W/cm^2 for laser wavelengths of $\lambda \sim 1$ μm. Consequently, in order to study the characteristic features of the excitation of the longitudinal electric field during ionization, we can solve Eq. (12) in the weakly relativistic approximation, omitting terms of second order in J_x and higher and retaining terms quadratic in E_z (below, for simplicity, we will consider laser pulses

with linear polarization along the z-axis):

$$\frac{\partial J_x}{\partial t} = \frac{e}{m_e}\rho_e E_x - \frac{e}{m_e c} J_z B_y. \quad (14)$$

Here, J_z can be taken to be linear in E,

$$\frac{\partial J_z}{\partial t} = \frac{e}{m_e}\rho_e E_z. \quad (15)$$

Taking into account the fact that the plasma is highly underdense, $n_e \ll n_c \equiv m_e\omega^2/4\pi e^2$, we obtain from the Maxwell equations the relationship

$$B_y = -E_z,$$

which is valid to zero order in the parameter n_e/n_c and enables us to rewrite Eq. (14) as

$$\frac{\partial J_x}{\partial t} = \frac{e}{m_e}\rho_e E_x + \frac{e}{m_e c} J_z E_z. \quad (16)$$

Note that Eqs. (13), (15), and (16), supplemented with Eqs. (4)–(6) and the equation $\rho_e(\partial\rho_e/\partial t = e\Gamma)$ for the electron density, which is analogous to Eq. (2) and in which the term $\mathrm{div}(n_e\mathbf{V}_e)$ is discarded, completely describe one-dimensional excitation of the longitudinal plasma field E_x by a plane-polarized laser pulse in the approximation that is linear in the electron density n_e and quadratic in E_z. In the approximation cubic in the relativistic corrections (i.e., with allowance for the inverse effect of the wakefield on the laser radiation), the laser pulse propagation is described by the z-component of Eq. (11) and the projection of Eq. (12) for the current onto the z-axis:[2]

$$\frac{\partial J_z}{\partial t} + \frac{\partial}{\partial x}\left(\frac{J_z J_x}{\rho_e}\right) = \frac{e}{m_e}\left[1 - \frac{3J_z^2}{2\rho_e^2 c^2} - \frac{J_x}{\rho_e c}\right]\rho_e E_z. \quad (17)$$

We emphasize that this approach accounts for the full set of harmonics of the electron source term $\Gamma(t)$ (Figs. 1, 2).

3.1. Equations for Slowly Varying Amplitudes of the Longitudinal Wake Electric Field and the Transverse Laser Electric Field

Using the set of equations derived above, we can analyze, on the one hand, the effect of ionization processes on the wakefield excitation and, on the other hand, the nonlinear effect of both ionization processes and the generation of a plasma wave on the electromagnetic field of a laser pulse. We can simplify the analysis and obtain analytic results by averaging Eqs. (2), (4)–(6), (11), and (13)–(17). We thus arrive at equations for the slowly varying (over the pulse period) complex amplitudes of the transverse laser electric field $E_{z,1} = \langle E_z \exp(i\omega t)\rangle$ and longitudinal electric field $E_{x,0} = \langle E_x\rangle$ (the angular brackets indicate averaging over the time interval $2\pi/\omega$, where ω is the laser frequency). We expand each of the quantities E_x, E_z, J_x, J_z, Γ, and n_e, which vary rapidly on the time scale $2\pi/\omega$, in a harmonic series of the form

$$A(x,t) = A_0(x,t) + \frac{1}{2}\sum_{n=1}^{\infty}\left[A_n(x,t)e^{-in\omega(t-x/c)} + A_n^*(x,t)e^{in\omega(t-x/c)}\right],$$

where A stands for any of these quantities and A_n is the slowly varying (on the time scale $2\pi/\omega$) amplitude of the nth harmonic of A. The main condition for this expansion to be valid is the inequality $\Gamma_0/(n_e\omega) < 1$, which should hold in the region where the bulk atoms are already ionized. Our calculations show that this inequality is satisfied for moderately short laser pulses, which are at least as long as several oscillation periods.

We should take into account two circumstances. First, the series expansion for the electron density contains only even harmonics, which stem, on the one hand, from the ionization processes (n_e increases in a steplike manner each half-period of the laser field; see Fig. 1) and, on the other hand, from the hydrodynamic and relativistic nonlinear effects. Second, in the weakly relativistic approximation, the amplitude $E_{z,1}$ of the first harmonic of the laser field is maximum. Then, using Eqs. (13), (15), and (16) and taking into account Eq. (2), we obtain the following equation for the slowly

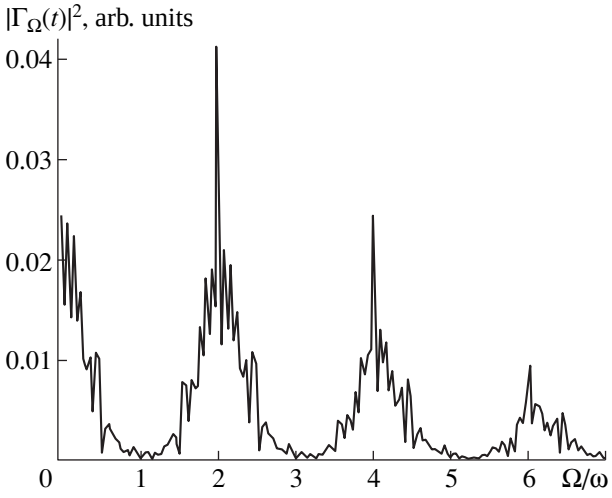

Fig. 2. Spectrum $|\Gamma_\Omega|$ (arb. units) of the ionization term $\Gamma(t)$ for a carbon gas. The laser parameters are the same as in Fig. 1.

[2] In this equation, the electron charge density in the term $e\rho_e E_z/m_e$ should be deduced from the continuity equation with the term $\mathrm{div}(n_e\mathbf{V}_e)$, specifically, $\partial\rho_e/\partial t + \mathrm{div}\,\mathbf{J} = e\Gamma$.

varying dimensionless amplitude $a_p = eE_{x,0}/(m_e\Omega_p c)$ of the longitudinal electric field:

$$\frac{\partial^2 a_p}{\partial t^2} + \omega_p^2 a_p = -\frac{\omega_p^2}{4\Omega_p}\left\{\frac{\partial |a|^2}{\partial t} + 2|a|^2\frac{\Gamma_0}{n_{e,0}} - \frac{1}{2}\mathrm{Re}\left\{(a^*)^2\frac{\Gamma_2}{n_{e,0}}\right\}\right\},$$

where $n_{e,0} = \int_{-\infty}^{t}\Gamma_0(t')dt'$, $\omega_p^2 = 4\pi e^2 n_{e,0}/m_e$, $\Omega_p^2 = (4\pi e^2/m_e)\int_{-\infty}^{+\infty}\Gamma_0(t)dt$, and $a = eE_{z,1}/(m_e\omega c)$. For an elliptically polarized laser pulse, we have $a = eE_l/(m_e\omega c)$, where the laser field amplitude E_l is determined by the pulse intensity $I_l = (c/8\pi)|E_l|^2$. Since, in the variables $\xi = x - ct$, $\tau = t$, the quantities E_z and n_e treated in the quasistatic approximation [5] depend mainly on ξ, the latter equation becomes

$$\frac{\partial^2 a_p}{\partial \xi^2} + k_p^2 a_p = \frac{k_p^2}{4\Omega_p}\left\{c\frac{\partial |a|^2}{\partial \xi} - 2|a|^2\frac{\Gamma_0}{n_{e,0}} + \frac{1}{2}\mathrm{Re}\left\{(a^*)^2\frac{\Gamma_2}{n_{e,0}}\right\}\right\}, \quad (18)$$

where $k_p^2 = \omega_p^2/c^2$. From Eqs. (11) and (17), we obtain an equation for the dimensionless envelope a of the transverse laser field:

$$2\omega\frac{\partial a}{\partial \tau} - 2ic\frac{\partial^2 a}{\partial \xi \partial \tau} + i\left(\omega_p^2 + \frac{\partial a_p}{\partial \xi}c\Omega_p - \frac{|a|^2}{4}\omega_p^2\right)a = -\frac{2\omega}{a^*}\sum_{m=0}^{Z-1}\frac{\Gamma_0^{\langle m\rangle}}{n_c}\frac{U_m}{m_e c^2} + \frac{\Gamma_2\omega_p^2}{4\omega n_{e,0}}a^*. \quad (19)$$

In deriving (19), we used the Maxwell equation $\mathrm{div}\mathbf{E} = 4\pi\rho$ to express the zeroth harmonic of the electron density through the background electron density, which is proportional to ω_p^2, and the perturbed electron density, which is proportional to $\partial a_p/\partial\xi$ and is associated with the generation of a wake plasma wave.

An attempt to analyze how ionization influences the wakefield excitation was made, in particular, in [18, 19]. However, in contrast to Eq. (18), which was derived here by applying the kinetic approach to gas ionization, the model equations analogous to (18) that were proposed in [18, 19] are phenomenological and contain some undetermined parameters. In our model, supplementing Eq. (18) with Eqs. (19) and (4)–(6), from which we find Γ_0, Γ_2, and $n_{e,0}$, yields a closed self-consistent set of equations.

Note that Eq. (18) differs markedly from the set of Eqs. (13), (15), and (16) in that it contains only slowly varying quantities; moreover, in the weakly relativistic approximation, Eq. (18) includes only the zeroth (Γ_0) and second (Γ_2) harmonics from the full set of harmonics of the source Γ of free electrons (see the spectrum of Γ in Fig. 2). We emphasize that the model proposed by Mori and Katsouleas [18] differs qualitatively from our approach to the theory of wakefield generation in that it neglects the highest harmonics of the free-electron source.

Equation (19) implies that the energy of laser radiation changes according to the law

$$\frac{\partial}{\partial \tau}\int_{-\infty}^{\infty}d\xi|a|^2 = -\frac{c}{2}\int_{-\infty}^{\infty}d\xi\left\{\frac{n_e - n_{e,0}}{n_c}\frac{\partial |a|^2}{\partial \xi} - |a|^2\frac{\partial}{\partial \xi}\left(\frac{n_{e,0}}{n_c}\right) - \mathrm{Re}\left(\frac{\Gamma_2}{2cn_c}a^{*2}\right) + 4\sum_{k=0}^{Z-1}\frac{\Gamma_0^{\langle k\rangle}}{n_c}\frac{U_k}{m_e c}\right\}. \quad (20)$$

According to Eq. (20), the losses of laser energy can be classified into two groups: adiabatic losses, which are associated with the ponderomotive force, and nonadiabatic losses, which stem from gas ionization by laser radiation. Adiabatic losses include, in particular, the fraction of energy that is expended on the excitation of a wake plasma wave [2] and is described by the first term on the right-hand side of Eq. (20). Since these adiabatic energy losses depend resonantly on the pulse duration and are maximum when the pulse duration is approximately equal to the period of plasma waves, they can be neglected even when the propagation distance of a laser pulse is long and the plasma is highly underdense [2, 3].

Nonadiabatic losses result from the nonadiabatic nature of ionization and consist of two parts. First, they include energy losses associated with overcoming the atomic potential barrier [32, 16], which are described by the fourth term with U_m on the right-hand side of (20). These losses can be ignored if the penetration depth x of laser radiation into the plasma satisfies the inequality $x \ll x_U = \frac{c}{8\pi}\int_{-\infty}^{\infty}E_0^2(t)dt/\sum_{m=1}^{Z}N_m(t = +\infty)\sum_{n=0}^{m}U_n$, where $E_0(t)$ is the amplitude of the electric field of the laser pulse at the entrance to the region occupied by the gas and $N_m(t = +\infty)$ is the density of the ions in the mth ionization state after the ionizing pulse. For convenience in estimates, we can represent x_U in the form

$$x_U/L_\mathrm{p} \approx 2\times 10^3\left(\frac{I_\mathrm{max}\ [\mathrm{W/cm^2}]}{10^{16}\ [\mathrm{W/cm^2}]}\right)\left(\frac{N_\mathrm{at}\ [\mathrm{cm^{-3}}]}{10^{18}\ [\mathrm{cm^{-3}}]}\right)^{-1} \times\left(\sum_{m=1}^{Z}\frac{N_m(t = +\infty)}{N_\mathrm{at}}\sum_{n=0}^{m-1}U_n\ [\mathrm{keV}]\right),$$

where $L_p = c\tau_p$ is the characteristic length of the pulse and I_{max} is its peak intensity. Second, the laser field energy is lost due to losses associated with the conversion of a fraction of the laser energy into residual electron energy [37, 38]. These losses are described by the second and third terms on the right-hand side of Eq. (20), which constitute a function localized in ξ [20] and are unimportant on spatial scales $x \ll x_Q = \frac{cn_e^{-1}}{8\pi}\int_{-\infty}^{+\infty} E_0^2(t)dt/Q_e(t = +\infty)$, where $Q_e(t = +\infty) = n_e^{-1}\int_{-\infty}^{+\infty}\frac{\mathbf{P}^2(t = +\infty, t^*)}{2m_e}\Gamma(t^*)dt^*$ is the residual electron energy behind the laser pulse and $\mathbf{P}(t = +\infty, t^*)$ is the momentum that the electrons originating at approximately the instant $t = t^*$ gain up to the time $t = +\infty$. According to [24], the energy Q_e can be estimated as $Q_e \approx \sum_{m=1}^{Z_{max}}\frac{3U_m^3}{(\hbar\omega)^2}\left[\frac{3}{2}\alpha_m^3(t_m) + \eta^2\alpha_m^2(t_m)\right]$ for a laser pulse with a nearly linear polarization ($1 - \eta^2 \gg 3\alpha_m$) and as $Q_e \approx \frac{1+\eta^2}{2}\sum_{m=1}^{Z_{max}}\frac{3U_m^3}{(\hbar\omega)^2}\alpha_m^2(t_m)$ for a laser pulse with nearly circular polarization ($1 - \eta^2 \ll 3\alpha_m$). Here, η is the polarization ellipticity ($\eta = 1$ corresponds to circular polarization and $\eta = 0$ refers to linear polarization), t_m is the instant at which the electrons are ejected out of the $[m-1]$th shell of the ions (atoms) at the highest rate, $\alpha_m(t) \equiv [M_m/(m+1)]^3|E_l(t)|/E_{at} \sim 10^{-1}$ is a small parameter in the region where the ionization rate is essentially nonzero, and Z_{max} is the maximum number of completely ionized electron shells at fixed parameters of the laser radiation. The last formulas enable us to estimate x_Q as

$$x_Q/L_p \approx 6\times 10^2\left(\frac{I_{max}\ [\mathrm{W/cm^2}]}{10^{16}\ [\mathrm{W/cm^2}]}\right)\left(\frac{N_{at}\ [\mathrm{cm^{-3}}]}{10^{18}\ [\mathrm{cm^{-3}}]}\right)$$
$$\times\left\{\sum_{m=1}^{Z_{max}}\left(\frac{U_m\ [\mathrm{eV}]}{100\ [\mathrm{eV}]}\right)^3(\lambda\ [\mu\mathrm{m}])^2\right.$$
$$\left.\times\left[\left(\frac{\alpha_m(t_m)}{10^{-1}}\right)^3 + 6.3\eta^2\left(\frac{\alpha_m(t_m)}{10^{-1}}\right)^2\right]\right\}^{-1}$$

for $1 - \eta^2 \gg 3\alpha_m$ and

$$x_Q/L_p \approx 8\times 10^1\left(\frac{I_{max}\ [\mathrm{W/cm^2}]}{10^{16}\ [\mathrm{W/cm^2}]}\right)\left(\frac{N_{at}\ [\mathrm{cm^{-3}}]}{10^{18}\ [\mathrm{cm^{-3}}]}\right)^{-1}$$
$$\times\left\{\frac{1+\eta^2}{2}\sum_{m=1}^{Z_{max}}\left(\frac{U_m\ [\mathrm{eV}]}{100\ [\mathrm{eV}]}\right)^3(\lambda\ [\mu\mathrm{m}])^2\left(\frac{\alpha_m(t_m)}{10^{-1}}\right)^2\right\}^{-1}$$

for $1 - \eta^2 \ll 3\alpha_m$.

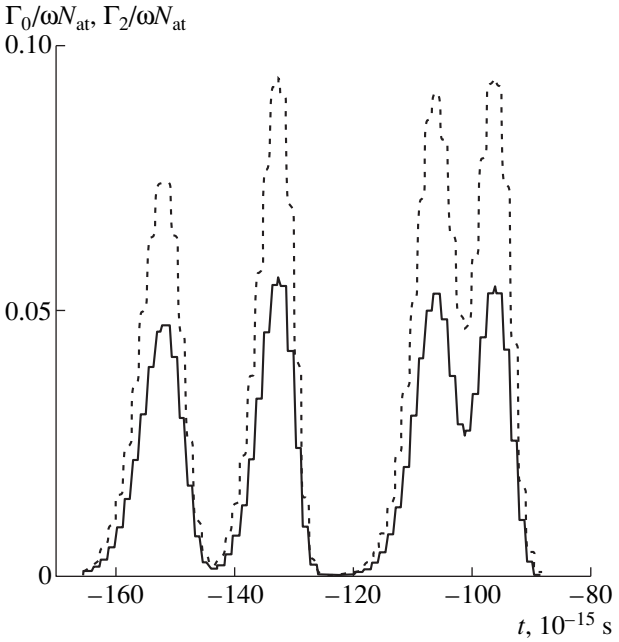

Fig. 3. Harmonics of the ionization rate, $\Gamma_0(t)$ (solid curve) and $\Gamma_2(t)$ (dashed curve), normalized to $N_{at}\omega$, for a carbon gas (the zero time corresponds to the pulse center). The laser parameters are the same as in Fig. 1.

The above estimates for x_U and x_Q imply that, in most of the cases that are important from a practical standpoint ($Z < 10$, $N_{at} < 10^{18}$ cm^{-3}, and $I_{max} > 10^{16}$ W/cm^2), the energy losses are significant only on spatial scales of about several hundreds of laser wavelengths or longer. On shorter spatial scales, variations in $|a|^2$ as a result of losses of the pulse energy due to gas ionization can be discarded, in which case we can determine the wakefield amplitude a_p assuming that the laser pulse is prescribed and neglecting possible self-modulation of the pulse [6–10, 13, 14]).

The plots of $\Gamma_0(\xi)$ and $\Gamma_2(\xi)$, which enter Eqs. (18) and (19), are shown in Fig. 3 for the particular case of ionization of a carbon gas by a linearly polarized laser pulse. In this case, the quantity $\mu(\xi) = (1/2)\Gamma_2(\xi)/\Gamma_0(\xi)$ obeys the relationship

$$\mu(\xi) \approx \frac{\sum_{m=1}^{Z} N_{m-1}\left\{1 + \frac{3}{2}\left[M_{k-1} - \frac{25}{8}\right]\alpha_m(\xi)\right\}}{\sum_{m=1}^{Z} N_{m-1}\left\{1 + \frac{3}{2}\left[M_{k-1} - \frac{9}{8}\right]\alpha_m(\xi)\right\}},$$

which holds when the power index of the exponential function in formula (5) is sufficiently large (i.e., when $\alpha_m(\xi) \ll 1/3$). For such values of $\alpha_m(\xi)$, the quantity

$\mu(\xi)$ depends weakly on ξ. For different gases, it lies in the range (0.7, 1); for example, for hydrogen, we have $\mu(\xi) \approx 0.83$. Note that the expression for $\mu(\xi)$ derived by Brunel [34] differs from our expression because, first, he used the ionization rate for hydrogen rather than the ionization rate adopted in [34] and, second, our expression for Γ_2 is more exact.

In the case of a circularly polarized pulse, the spectrum of the ionization source contains no satellite harmonics and the wakefield excitation is described by Eq. (18) with $\Gamma_2 = 0$ ($\mu = 0$). Below, most of our attention will be focused on a pulse with linear polarization, in which case both the zeroth and second harmonics should be taken into account.

3.2. Analytic Solution for a Prescribed Laser Pulse

Equation (18) is easy to solve analytically if we take into account the fact that the width of the ionization front, $L_{\text{ion}} = c\tau_{\text{ion}}$, is much shorter than both the wavelength of a laser pulse, $L_{\text{p}} = c\tau_{\text{p}}$, and the plasma wavelength. We approximate the electron density profile $n_{e0}(\xi)$ as $n_{e0}(\xi) = n_{\text{at}} \sum_{m=1}^{Z_{\max}} \theta(\xi_m - \xi)$, where ξ_m is the position of the mth ionization front and the integer $Z_{\max}$ is equal to the maximum possible ion charge for the given parameters of the laser pulse. Since, in the general case of multielectron atoms (when $Z_{\max}$ is large), the solution is somewhat involved, we present it for the case of hydrogen ($Z_{\max} = 1$):

$$\begin{aligned} a_p &= -\frac{1}{2}a^2(\xi_1)G_\Gamma(\xi_1)\sin[k_p(\xi_1 - \xi)] \\ &+ \frac{1}{4}\int_{\xi_1 - 0}^{\xi} a^2(\xi')\cos[k_p(\xi - \xi')]k_p d\xi' \\ &+ \frac{B}{4}a^2(\xi_1 - 0)\sin[k_p(\xi_1 - \xi)], \\ G_\Gamma(\xi) &\equiv 1 - \frac{\mu(\xi)}{2}, \end{aligned} \tag{21}$$

where $k_p = \Omega_p/c$ is the wave vector of the plasma wave behind the pulse and ξ_1 is the point at which the ionization rate Γ_0 is the highest. The term proportional to $G_\Gamma(\xi)$ stems from the ionization source, and the second and third terms on the right-hand side of (21) describe the ponderomotively driven wakefield. When the pulse propagates in a preionized gas [in which case $\xi_1 = \infty$ and $a(\xi_1) = 0$], we have $B = 0$. When the gas is ionized immediately by a pulse with a smooth front of width $L_f \gg L_{\text{ion}}$, we have $B = 1$.

We use formula (21) to investigate the effect of ionization of an initially neutral gas at the laser pulse front on the wakefield excitation. For simplicity, we consider a rectangular pulse ($a(\xi) = 0$ for $|\xi| > L/2$) with the total length $L \gg L_f$, assuming again that $L_f \gg L_{\text{ion}}$, in which case $B = 1$. We also assume that $k_p^{-1} \gg L_f$. If such a rectangular pulse propagates in a preionized homogeneous gas, then, for $\xi < -L/2$, the second term on the right-hand side of (21) yields a familiar result [2]: $a_p = (1/2)a_0^2\cos(k_p\xi)\sin(k_pL/2)$. This indicates that the wakefield is the strongest at $k_pL = \pi(1 + 2n)$ (where n is an integer), the maximum field amplitude being $(1/2)a_0^2$ (where $a_0 = eE_{\max}/(m\omega c)$, $E_{\max} = \sqrt{8\pi I_{\max}/c}$). When a rectangular pulse ionizes an initially neutral gas, the second and third terms on the right-hand side of (21), which describe the ponderomotively driven plasma wave, give the following expression for the wakefield amplitude at $\xi < -L/2$:

$$\begin{aligned} a_p &= -1/4[[2a_0^2 - a^2(\xi_1)]\cos(k_p\xi)\sin(k_pL/2) \\ &+ a^2(\xi_1)\sin(k_p\xi)\cos(k_pL/2)]. \end{aligned}$$

The amplitude is seen to be maximum under the same condition $k_pL = \pi(1 + 2n)$, in which case the total wakefield amplitude in an ionized gas has the form

$$\begin{aligned} &a_p \\ &= [(-1)^{n+1}/2][a_0^2 + a^2(\xi_1)(G_\Gamma - 1/2)]\cos(k_p\xi), \end{aligned} \tag{22}$$

where the term proportional to $G_\Gamma a^2(\xi_1)$ stems from the ionization source and the remaining terms describe the ponderomotively driven wakefield. From the above expressions for G_Γ and μ, we have $G_\Gamma \simeq 0.6$ for a circularly polarized pulse and $G_\Gamma = 1$ for a pulse with linear polarization. Accordingly, when $I_{\max}$ is close to the ionization threshold I_{th}, we have $a^2(\xi_1) \approx a_0^2$. As a result, from (22), we find that the total (with allowance for both ionization and ponderomotive forces) maximum amplitude of the wakefield excited in an initially neutral gas is larger than that of a wakefield excited in a completely preionized gas by approximately 10% in the case of a linearly polarized pulse and by approximately 50% in the case of a circularly polarized pulse. For $I_{\max} \gg I_{\text{th}}$, we have $a^2(\xi_1) \ll a_0^2$, so that, in the case of an initially neutral gas, the wakefield amplitude is essentially the same as that in the case of a completely preionized gas.[3]

Using expression (21), we can show that the situation with a Gaussian laser pulse is qualitatively the same. Specifically, for $I_{\max} \gg I_{\text{th}}$, ionization processes also have an insignificant impact on the wakefield amplitude.[4] When $I_{\max}$ is close to I_{th}, ionization processes act to enhance the wakefield amplitude by

[3] This is true for $k_pL \neq 2\pi n$; otherwise, we have $a_p = 0$ in the case of a preionized gas and $a_p \neq 0$ when the gas is ionized directly by the laser pulse.

[4] This is true for the case of nearly resonant excitation of a wake wave by ponderomotive forces, i.e., when the laser pulse length is slightly longer than the plasma wavelength.

approximately 10% in the case of linear polarization and by approximately 50% in the case of circular polarization. However, the dependence of the maximum amplitude of the wakefield excited by a Gaussian pulse in an initially neutral gas on the dimensionless pulse length is peaked at a pulse length somewhat longer than that in the case of wakefield generation in a preionized gas (see Fig. 4).

3.3. Results of the Numerical Solution

The above analytic conclusions agree well with the results of a more exact numerical solution of Eq. (18); simulations of the wakefield generation on the basis of Eqs. (2), (4)–(6), (13), (15), and (16), with the full set of the harmonics of Γ; and PIC simulations (see the next section). We used Eq. (18) and the above expression for μ(ξ) to calculate the longitudinal wakefield excited during gas ionization by a Gaussian laser pulse

$$a(\xi) = a_0 \exp[-2\ln 2(\xi/L_p)^2], \qquad (23)$$

where $L_p = \tau_p c$ is the laser-pulse full width at half-maximum. The zeroth harmonics of the ionization rate Γ_0 and electron density $n_{e,0} = -\frac{1}{c}\int_{+\infty}^{\xi} \Gamma_0(s)ds$ were computed from (4) and (6), which were averaged over the laser field period and in which the ionization rates were calculated from formula (5), which was also averaged over the laser field period. For a linearly polarized pulse, formula (5) becomes [30, 31]

$$\overline{W}_m(\xi) = \omega_{at}\left(\frac{3\exp(1)}{\pi}\right)^{3/2}\frac{(m+1)^2}{3M_m^{4.5}} \times \left[\frac{4\exp(1)(m+1)^3}{M_m^4}\frac{E_{at}}{E_{z1}(\xi)}\right]^{2M_k - 1.5} \times \exp\left[-\frac{2}{3}\frac{(m+1)^3}{M_m^3}\frac{E_{at}}{E_{z1}(\xi)}\right].$$

The results of studying the wakefield amplitude as a function of the pulse length are presented in Fig. 4. The amplitude of the wakefield excited in a preionized gas is shown by the dashed curve. The solutions to Eq. (18) for circularly polarized and linearly polarized lasers are illustrated by the heavy and light solid curves, respectively. We can see that the solid curves essentially coincide with the results of solving the more complicated equations (2), (13), (15), and (16), which are not averaged over time. Finally, in Fig. 4a, the PIC simulation results for circularly polarized and linearly polarized lasers are presented by the closed and open circles, respectively. The circles are also seen to agree well with the solutions to Eq. (18).

Analyzing Fig. 4, we can draw the following conclusions. On the one hand, ionization processes act to increase the maximum amplitude of the wakefield driven by the ponderomotive forces in the range of resonant pulse lengths ($k_p L_p \approx 2.4$). On the other hand (and more importantly), ionization processes make it possible to generate wake plasma waves by substantially longer laser pulses. The latter effect is especially pronounced in the case of ionization of atoms with a small number of electron shells (see Fig. 4a for hydrogen); moreover, for the parameters adopted here, the amplitude of the wakefield excited by long nonresonant ($k_p L_p \gg 1$) pulses is comparable with that in the case of

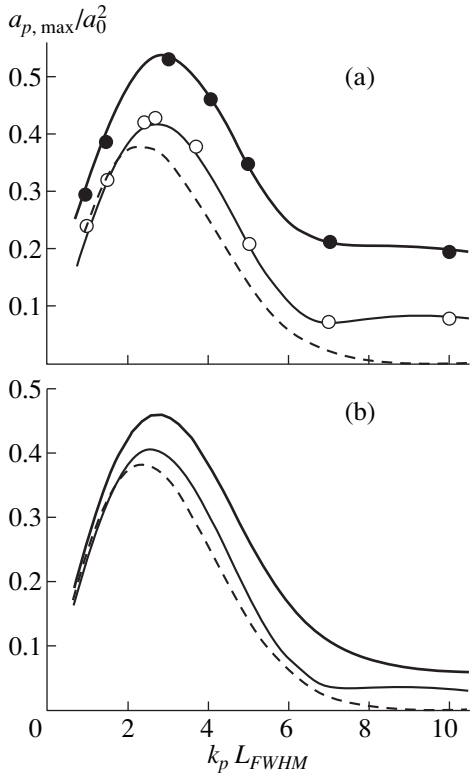

Fig. 4. Maximum normalized wakefield amplitude $a_{p,\max}/a_0^2$, where $a_{p,\max} = eE_{x,0\max}/(m_e\Omega_p c)$ and $\Omega_p = [4\pi e^2 n_{e\max}/m_e]^{1/2}$, vs. the dimensionless length $L_p\Omega_p/c$ of a Gaussian ionizing laser pulse (23) (with the wavelength $\lambda = 1$ μm) propagating in (a) a hydrogen gas with the density $N_{at} = 10^{-2}n_c$ and (b) a nitrogen gas with the density $N_{at} = 2\times 10^{-3}n_c$. The dimensionless peak amplitude of the pulse is equal to $a_0 = eE_{max}/(m_e\omega c) = 0.025$ ($I_{max} = cE_{max}^2/(8\pi) \approx 8.57\times 10^{14}$ W/cm^2) for hydrogen and $a_0 = 0.175$ ($I_{max} \approx 4.2\times 10^{16}$ W/cm^2) for nitrogen. The light and heavy solid curves refer to linearly polarized and circularly polarized pulses, respectively. The dashed curves are depicted for a pulse propagating in a preionized gas with the maximum electron density $n_{e\max} = Z_{max}N_{at} = 10^{-2}n_c$ ($Z_{max} = 1$ for hydrogen and $Z_{max} = 5$ for nitrogen). The open and closed circles reflect the PIC simulation results for hydrogen in the case of (a) linear and (b) circular polarization, respectively.

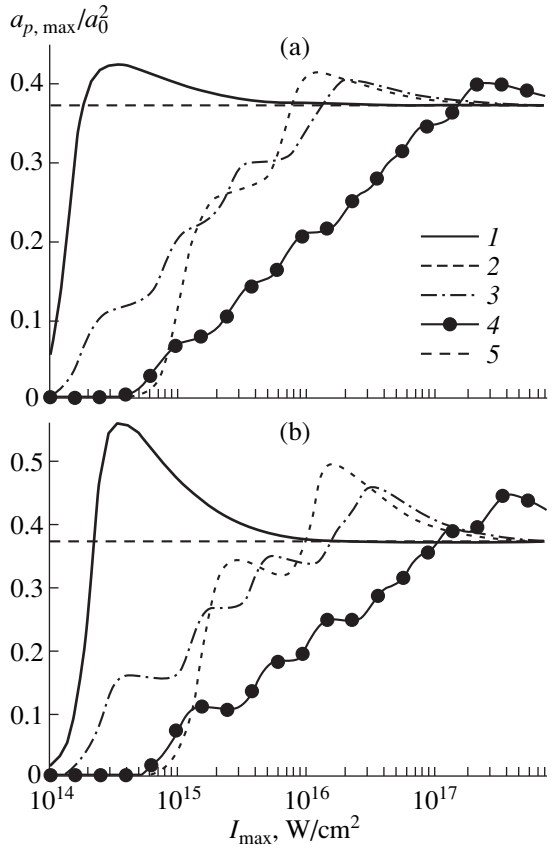

Fig. 5. Maximum normalized wakefield amplitude $a_{p,\max}/a_0^2$ vs. the peak intensity $I_{\max}$ of a Gaussian ionizing laser pulse with the wavelength $\lambda = 1$ μm in the case of (a) linear and (b) circular polarization. The dimensionless pulse length is $L_p\Omega_p/c = 2.7$, and the maximum electron density in a gas after the passage of the pulse is $n_{e\max} = Z_{\max}N_{at} = 10^{-2}n_c$. The results presented were obtained for (*1*) hydrogen, $Z_{\max} = 1$; (*2*) helium, $Z_{\max} = 2$; (*3*) nitrogen, $Z_{\max} = 5$; and (*4*) neon, $Z_{\max} = 8$. Curve (*5*) presents the wakefield amplitude in the case of propagation of a laser pulse through a preionized gas with the electron density $n_{e\max}$.

resonant pulses. In the case of ionization from many electron shells, this effect is less pronounced (compare Figs. 4a and 4b). We can expect that this effect will be significant in the case of ionization from the lowest *s* shell of multielectron atoms, which are characterized by high ionization energies (e.g., 552 and 667 eV for electrons from the *s* shell of a nitrogen atom). However, the ionizing fields required to eject the electrons out of the lowest shells are so strong that, strictly speaking, the weakly relativistic approximation used in our study fails to hold.

Figure 5 illustrates the results of calculations of the wakefield amplitude as a function of the peak intensity of the laser pulse for different gases. In computations, the gas density was chosen in such a way that the conditions for the resonant excitation of a plasma wave by the ponderomotive force were satisfied at the maximum possible (in the laser intensity range under consideration) electron density. For multielectron gases, the maximum amplitude $a_{p,\max}$ is a more complicated function of $I_{\max}$ in comparison with that for hydrogen. The peaks in the dependence of $a_{p,\max}$ on $I_{\max}$ stem from the successive ionization of the electron shells, starting from the shell farthest from the nucleus. The effect of the ionization processes on the wakefield amplitude is expected to be the strongest for laser pulses with moderate peak intensities, when the ionization saturates near the pulse center. In this case, the amplitude of the wakefield driven resonantly in an initially neutral gas is larger than that of a wakefield excited in a preionized gas by about 10% for a linearly polarized pulse and by about 50% for a circularly polarized pulse. The amplitude of the wakefield generated by a high-intensity laser pulse in an initially neutral gas (when the ionization saturates at the leading portion of the pulse far from the pulse center) is essentially the same as that in the case of a preionized gas and does not depend on the pulse polarization.

4. RESULTS FROM PIC SIMULATIONS OF LASER PULSE PROPAGATION IN A GAS AND WAKEFIELD GENERATION

The kinetic processes that occur during gas ionization by a laser pulse were modeled with a relativistic electromagnetic 1D3V PIC code, in which the standard PIC method for plasma simulation was supplemented with an algorithm suitable for modeling gas ionization in a strong field. The production of particles that model free electrons originating from gas ionization in a laser field was simulated by this algorithm as follows: (i) particles originate at a zero initial velocity and (ii) the number ΔN of particles in each cell over the time interval Δt is computed from the formula $\Delta N = \frac{N_{\text{cell}}}{ZN_{\text{at}}}\int_t^{t+\Delta t}\Gamma\,dt'$, where Γ is calculated from relationships (4)–(6) taken with the instantaneous electric field amplitude $|\mathbf{E}(x, t)|$, ZN_{at} is the electron density, and N_{cell} is the number of particles in a cell in the case of a completely ionized gas. Note that, since the number Δn of free electrons originating over the time interval Δt per unit volume is equal to $\Delta n = \int_t^{t+\Delta t}\Gamma\,dt'$, the number of particles Δn produced in each cell is related to ΔN by $\Delta N/N_{\text{cell}} = \Delta n/ZN_{\text{at}}$. The dynamics of the ionization-produced free electrons was simulated in the standard manner [39]. On the time scales under consideration, the atoms and ions were assumed to be immobile. For hydrogen, the simulations were carried out with $N_{\text{cell}} = 75$ (varying the number N_{cell} of particles in a cell from 50 to 150 did not significantly influence the calculation accuracy). In the simulations described here, the spatial and temporal steps for numerical modeling were determined from the shortest spatial scale (the spatial cell

size), which was chosen in order to resolve the ionization front (which depends on both the pulse duration and intensity). Thus, for a pulse with an amplitude $a_0 = 0.025$ and a duration of $10\omega^{-1}$–$100\omega^{-1}$, the spatial step was chosen to lie in the interval $0.025c/\omega$–$0.1c/\omega$, which ensured the desired accuracy of computations.

The fraction of laser energy expended on gas ionization was modeled by supplementing the Maxwell equations with the dissipative currents, which were calculated from the phenomenological formula (10). The Maxwell equations were integrated by the method of vacuum characteristics [39].

The results from calculations of the amplitude of the wakefield excited by linearly polarized and circularly polarized laser pulses are illustrated in Fig. 4, which shows that they agree well with the results obtained from the equations for the averaged amplitudes.[5]

Our PIC code can be used not only to obtain the wakefield amplitude but also to calculate the electron velocity distribution function $f(v_x, v_z, t, x)$. Figure 6 displays the function $f(v_x, 0, t, x_0)$ calculated at two different times $t = t_1$ and $t = t_2$ at the point x_0 after the passage of a linearly polarized ionizing laser pulse. Behind the pulse, the electrons oscillate in a wakefield, so that, at an arbitrary time t, the function $f(v_x 0, t, x_0)$ is shifted from $v_x = 0$ by an amount $V_x(t)$, which coincides with the velocity determined from the hydrodynamic equations. The instants t_1 and t_2 were chosen to correspond to the maximum hydrodynamic velocities $V_x = V_{x,\max}(-V_{x,\max})$ of the electrons moving along the x-axis in the positive and negative direction, respectively. In this case, the peak in the function $f(v_x, 0, t, x_0)$ is shifted from $v_x = 0$ by an amount $V_{x,\max}$ at $t = t_1$ and by an amount $-V_{x,\max}$ at $t = t_2$ (Fig. 6). Let us compare the value of $|V_{x,\max}|$ obtained from Eq. (18) with that predicted by PIC simulations. We use Eq. (18) to calculate the dimensionless amplitude $a_p(t)$ for the parameters of Fig. 6. Then, we find the longitudinal electric field amplitude $|E_{x,\max}| = 8.5 \times 10^5$ V/cm. From the consequence of relationship (13), $|V_{x,\max}| = e|E_{x,\max}|/(m_e\Omega_p)$, we obtain $|V_{x,\max}|/c = 2.64 \times 10^{-4}$, which coincides with the corresponding result of PIC simulations to within 4%.

Figure 7 shows the function $f(0, v_z, t_1, x_0)$ for the same parameters as in Fig. 6. After the passage of the pulse, the plasma stops moving along the z-axis, so that the width of the distribution function in v_z is governed by the stochastic motion of the electrons due to the nonadiabatic character of their interaction with the laser field during ionization [20]. On the time scales under

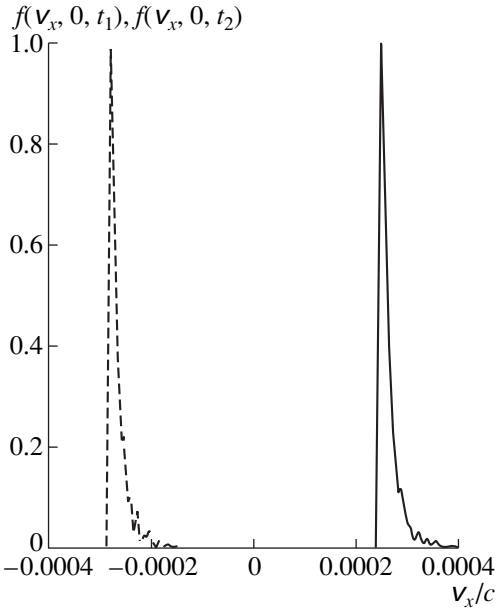

Fig. 6. Electron distribution function over the longitudinal velocities ($v_z = 0$), normalized to its maximum value, at the instants t_1 and t_2 at which a $a_p(t_1) = a_p(t_2) = 0$ (when the absolute value of the directed electron velocity, $|V_x|$, is maximum): the solid curve refers to $f(v_x, 0, t_1)$ at $V_x = V_{x,\max}$ and the dashed curve refers to $f(v_x, 0, t_2)$ at $V_x = -V_{x,\max}$. The results were obtained for a linearly polarized Gaussian laser pulse (with $\tau_p\omega = 30$, $I_{\max} = 8.57 \times 10^{14}$ W/cm^2, and $\lambda = 1$ μm) propagating in a hydrogen gas with the density $N_{at} = 1.1 \times 10^{19}$ cm^{-3}.

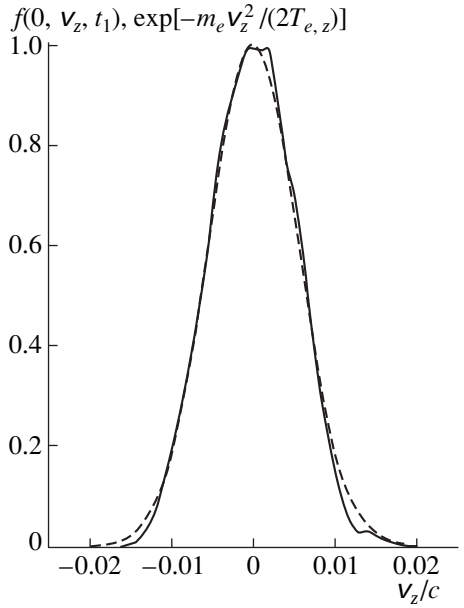

Fig. 7. Electron distribution function $f(0, v_z, t_1)$ over the transverse velocities (solid curve) and the Maxwellian distribution function with the electron temperature 15.4 eV (dashed curve). The functions are normalized to their maximum values. The laser parameters are the same as in Fig. 6.

[5] Note that the three calculation methods (the hydrodynamic method based on the full set of equations, the hydrodynamic method based on the reduced (averaged) equations, and the kinetic PIC method) yield not only nearly the same amplitudes of the electric field but also nearly the same field phases; in other words, the time evolutions $a_p(t)$ computed using these methods essentially coincide.

consideration, which are shorter than the electron–ion and electron–electron collision times, the total energy of the stochastic electron motion (the residual electron energy) is completely converted into the energy of the electron motion along the *z*-axis. This circumstance permits us to identify the residual energy with the "transverse" (in the *z*-direction) temperature $T_{e,z}$ [20, 26]. Since, in the case of a linearly polarized laser pulse, the transverse electron motion is one-dimensional, we have $T_{e,z}/2 = Q_e$, where Q_e is the residual energy per electron (see Section 3.1). Also shown in Fig. 7 is the Maxwellian electron distribution function over velocities v_z with the temperature $T_{e,z} = 2Q_e = 15.4$ eV, where the energy Q_e was determined analytically according to the theory developed by Andreev *et al.* [20]. We can see that the Maxwellian function is fairly close to that obtained from PIC simulations. A comparison between Figs. 6 and 7 shows that the residual energy of the transverse (to the laser-pulse propagation) electron motion along the *z*-axis is much higher than both the residual energy of the longitudinal electron motion along the *x*-axis [30] (this energy determines the width of the distribution function in Fig. 6) and the residual energy of the longitudinal electron motion in a wakefield (this energy governs the shift of distribution functions relative to the point $x = 0$ in Fig. 6).

Our PIC simulation results also confirm the above estimates for the ionization-related laser-energy losses associated with the ionization current and residual electron energy, which are described by the fourth term and by the second and third terms on the right-hand side of Eq. (20), respectively. According to PIC simulations, the residual energy per plasma electron, $(m_e/2n_e)\int \mathbf{v}^2 f(\mathbf{v}, t, x_0) d^3\mathbf{v}$, is equal to 7.6 eV. This value is close to the energy $Q_e \approx 7.7$ eV calculated from the formulas presented in [20] and, to a high accuracy, agrees with the law of energy conservation in the interaction of a laser pulse with matter.

5. CONCLUSION

We have developed two hydrodynamic models and used them to calculate the generation of a wakefield, taking into account ionization processes in a gas. The reduced equation obtained for the wakefield envelope makes it possible to analytically study how ionization processes affect the wakefield amplitude and to investigate it as a function of the gas and pulse parameters.

We have shown that, when the peak intensity of the laser pulse is far above the ionization threshold and under conditions close to the resonant excitation of a wake plasma wave by the ponderomotive force, ionization processes have little effect on the wakefield excitation: the amplitude of the wakefield excited in an initially neutral gas is essentially the same as that of the wakefield excited by a laser pulse propagating in a preionized gas and does not depend on the pulse polarization. The most important result is that, under conditions that are far from resonance (i.e., for long laser pulses), the wakefield amplitude is enhanced by ionization and is much larger than that in the case of a preionized gas (see the range $k_p L_p > 8$ in Fig. 4).

During ionization, the wakefield can be generated by a longer laser pulse with peak intensities close to the ionization threshold, in which case the maximum amplitude of the ionization-enhanced wakefield is larger than that in the case of a preionized gas. This effect is most pronounced in light gases, such as hydrogen and helium. In the case of a linearly polarized laser, ionization processes act to increase the maximum amplitude of the wakefield at resonant pulse lengths by approximately 10% in comparison with that in a preionized gas. In the case of a circularly polarized laser radiation, this difference may be even larger: the increase in maximum amplitude may be as large as 50%.

The results of solving reduced (averaged) hydrodynamic equations for the slowly varying wakefield amplitude agree well with both kinetic PIC simulations and the results of solving the full set of hydrodynamic equations.

ACKNOWLEDGMENTS

This work was supported in part by the Russian Foundation for Basic Research, project no. 98-02-16263.

REFERENCES

1. *Proceedings of ICONO'98. Ultrafast Phenomena and Interaction of Superstrong Laser Fields with Matter: Nonlinear Optics and High-Field Physics* (Moscow, 1998); Proc. SPIE **3735** (1999).
2. L. M. Gorbunov and V. I. Kirsanov, Zh. Éksp. Teor. Fiz. **93**, 509 (1987) [Sov. Phys. JETP **66**, 290 (1987)]; L. M. Gorbunov and V. I. Kirsanov, Tr. FIAN **219**, 3 (1992).
3. P. Sprangle, E. Esarey, A. Ting, and G. Joyce, Appl. Phys. Lett. **53**, 2146 (1988).
4. D. Tajima and J. M. Dawson, Phys. Rev. Lett. **43**, 267 (1979).
5. P. Sprangle, E. Esarey, and A. Ting, Phys. Rev. Lett. **64**, 2011 (1990).
6. N. E. Andreev, L. M. Gorbunov, V. I. Kirsanov, *et al.*, Pis'ma Zh. Éksp. Teor. Fiz. **55**, 551 (1992) [JETP Lett. **55**, 571 (1992)]; Pis'ma Zh. Éksp. Teor. Fiz. **60**, 694 (1994) [JETP Lett. **60**, 713 (1994)].
7. T. M. Antonsen and P. Mora, Phys. Rev. Lett. **69**, 2204 (1992); Phys. Fluids B **5**, 1440 (1993).
8. P. Sprangle, E. Esarey, J. Krall, and G. Joyce, Phys. Rev. Lett. **69**, 2200 (1992); E. Esarey, P. Sprangle, J. Krall, *et al.*, Phys. Fluids B **5**, 2690 (1993).
9. W. B. Mori, C. Decker, D.E. Hinkel, and T. C. Katsouleas, Phys. Rev. Lett. **72**, 1482 (1994); Phys. Rev. E **50**, R3338 (1994); C. D. Decker, W. B. Mori, K.-C. Tzeng, and

T. C. Katsouleas, IEEE Trans. Plasma Sci. **24**, 379 (1996).

10. N. E. Andreev, L. M. Gorbunov, V. I. Kirsanov, *et al.*, Phys. Scr. **49**, 101 (1994); Phys. Plasmas **2**, 2573 (1995); IEEE Trans. Plasma Sci. **24**, 363 (1996); Fiz. Plazmy **21**, 872 (1995) [Plasma Phys. Rep. **21**, 824 (1995)]; Fiz. Plazmy **22**, 419 (1996) [Plasma Phys. Rep. **22**, 379 (1996)].
11. T. C. Chiou, T. C. Katsouleas, C. Decker, *et al.*, Phys. Plasmas **2**, 310 (1995); G. Shvets, J. S. Wurtele, T. C. Chiou, and T. C. Katsouleas, IEEE Trans. Plasma Sci. **24**, 351 (1996).
12. N. E. Andreev, L. M. Gorbunov, V. I. Kirsanov, *et al.*, Phys. Plasmas **4**, 1145 (1997); N. E. Andreev, E. V. Chizhonkov, A. A. Frolov, and L. M. Gorbunov, Nucl. Instrum. Methods Phys. Res. A **410**, 469 (1998); N. E. Andreev, L. M. Gorbunov, and A. A. Frolov, Fiz. Plazmy **24**, 888 (1998) [Plasma Phys. Rep. **24**, 825 (1998)].
13. E. Esarey, P. Sprangle, J. Krall, and A. Ting, IEEE Trans. Plasma Sci. **24**, 252 (1996).
14. N. E. Andreev and L. M. Gorbunov, Usp. Fiz. Nauk **169**, 53 (1999).
15. Y. Ehrlich, C. Cohen, A. Zigler, *et al.*, Phys. Rev. Lett. **77**, 4186 (1996).
16. M. V. Chegotov, Izv. Akad. Nauk, Ser. Fiz. **63**, 1088 (1999); M. V. Chegotov, Proc. SPIE **3683**, 33 (1998).
17. V. B. Gildenburg, M. D. Chernobrovtseva, A. V. Kim, *et al.*, in *Proceedings of the International Conference Lasers'97, New Orlean, LA, 1997* (STS, McLean, VA, 1998), p. 853.
18. W. B. Mori and T. Katsouleas, Phys. Rev. Lett. **69**, 3495 (1992).
19. D. L. Fisher and T. Tajima, Phys. Rev. E **53**, 1844 (1996).
20. N. E. Andreev, M. V. Chegotov, M. E. Veĭsman, *et al.*, Pis'ma Zh. Éksp. Teor. Fiz. **68**, 566 (1998) [JETP Lett. **68**, 592 (1998)].
21. L. V. Keldysh, Zh. Éksp. Teor. Fiz. **47**, 1945 (1964) [Sov. Phys. JETP **20**, 1307 (1964)].
22. P. B. Corkum, N. H. Burnett, and F. Brunel, Phys. Rev. Lett. **62**, 1259 (1989).
23. N. B. Delone and V. P. Krainov, J. Opt. Soc. Am. B. **8**, 1207 (1991).
24. N. E. Andreev, M. V. Chegotov, M. E. Veisman, *et al.*, in *Proceedings of ICONO'98. Ultrafast Phenomena and Interaction of Superstrong Laser Fields with Matter: Nonlinear Optics and High-Field Physics* (Moscow, 1998), p. 234; Proc. SPIE **3735**, 234 (1999).
25. S. P. Goreslavsky and S. V. Popruzhenko, Laser Phys. **7**, 700 (1997).
26. V. T. Tikhonchuk and V. Yu. Bychenkov, Laser Phys. **2**, 525 (1992).
27. P. Mulser, F. Cornolty, and D. Bauer, Phys. Plasmas **5**, 4466 (1998).
28. B. M. Smirnov, *Atomic Collisions and Elementary Processes in Plasmas* (Atomizdat, Moscow, 1968).
29. V. P. Silin, *Introduction into Kinetic Theory of Gases* (Nauka, Moscow, 1971).
30. M. V. Ammosov, N. B. Delone, and V. P. Kraĭnov, Zh. Éksp. Teor. Fiz. **91**, 2008 (1986) [Sov. Phys. JETP **64**, 1191 (1986)].
31. N. B. Delone and V. P. Kraĭnov, Usp. Fiz. Nauk **168**, 531 (1998) [Phys. Usp. **41**, 469 (1998)].
32. V. P. Kandidov, O. G. Kosareva, and S. A. Shlenov, Kvantovaya Élektron. (Moscow) **21**, 971 (1994).
33. A. V. Borovskiĭ and A. L. Galkin, Zh. Éksp. Teor. Fiz. **108**, 426 (1995) [JETP **81**, 230 (1995)].
34. F. Brunel, J. Opt. Soc. Am. B **7**, 521 (1990).
35. E. V. Vanin, M. S. Downer, A. V. Kim, and A. M. Sergeev, Pis'ma Zh. Éksp. Teor. Fiz. **58**, 964 (1993) [JETP Lett. **58**, 900 (1993)].
36. S. C. Rae and K. Burnett, Phys. Rev. A **46**, 2077 (1992).
37. V. B. Gil'denburg, A. V. Kim, and A. M. Sergeev, Pis'ma Zh. Éksp. Teor. Fiz. **51**, 91 (1990) [JETP Lett. **51**, 104 (1990)]; V. B. Gil'denburg, V. I. Pozdnyakova, and I. A. Shereshevskii, Phys. Lett. A **203**, 214 (1995).
38. M. V. Chegotov, Fiz. Plazmy **26** (10) (2000) [Plasma Phys. Rep. **26** (10), 881 (2000)].
39. Ch. K. Birdsall and A. B. Langdon, *Plasma Physics via Computer Simulation* (McGraw-Hill, New York, 1985; Énergoatomizdat, Moscow, 1989).

Translated by O. Khadin

Plasma Physics Reports, Vol. 26, No. 11, 2000, pp. 960–964. Translated from Fizika Plazmy, Vol. 26, No. 11, 2000, pp. 1024–1029.

CHARGED PLASMA

Thermodynamic Equilibrium of Pure Electron Plasmas in a Malmberg–Penning Trap

I. A. Kotelnikov*, R. Pozzoli, and M. Romé****

**Budker Institute of Nuclear Physics, Siberian Division, Russian Academy of Sciences, Novosibirsk, 630090 Russia*

***Universitä degli Studi di Milano, via Celoria 16, 20133 Milan, Italy*

Received May 12, 2000

Abstract—A new class of annular confinement configurations of a single-charged plasma corresponding to global thermodynamic equilibria in a cylindrical Malmberg–Penning trap with an axial conductor is investigated both numerically and analytically. In the case of an infinite plasma length, the density turns out to be essentially constant inside a surface of revolution and to fall off abruptly outside of it. Analytical limiting cases are calculated explicitly in the limit of small Debye lengths. In the case of a finite plasma length, the self-consistent solution to Poisson's equation describing thermodynamic equilibrium is obtained numerically and the dependence of the plasma density distribution on the various parameters of the system is investigated. © *2000 MAIK "Nauka/Interperiodica"*.

A peculiar characteristic of single-charged plasmas is that they can approach thermodynamic equilibrium while remaining confined by static electric and magnetic fields, as is the case of a Malmberg–Penning trap [1, 2]. The long confinement times obtained experimentally suggest that the equilibrium states in which a single-charged plasma fills a simply connected region of space are indeed achievable [3, 4]. For the confinement geometry of these experiments, a class of equilibrium density distributions that are consistent with Poisson's equation was determined in [5, 6] and was extensively discussed in [7]. Here, we consider a different thermodynamic equilibrium: a hollow plasma column in a Malmberg–Penning trap with an axial charged (biased) rod. This system shows the existence of a new class of axisymmetric plasma configurations ranging from long thin-wall structures to ringlike (doughnut) structures.

For definiteness, we consider a pure electron plasma confined in a conducting cylinder (of radius R) divided into three sections, the two end-plug sections being biased negatively relative to the central section. A uniform magnetic field **B** is directed along the cylinder axis, where a central rod (of radius r_d) is located. The confinement geometry is shown in Fig. 1.

Since the system is steady-state and has cylindrical symmetry, the equilibrium distribution function f depends on the electron energy $h = m_e v^2/2 - e\varphi$ and the electron canonical angular momentum $p_\theta = m_e v_\theta r - m_e \Omega r^2/2$ as [8]

$$f = n_0 (m_e/2\pi T)^{3/2} \exp[-(1/T)(h - \omega p_\theta)]. \quad (1)$$

Here, $\Omega = eB/mc$ is the electron-cyclotron frequency, ω is the azimuthal plasma rotation frequency, and the rest of the notation is standard. The constant parameters n_0, T, and ω are determined by the total number of particles, the total energy, and the total canonical angular momentum. The plasma density n obeys the Maxwell–Boltzmann distribution law

$$N = n_0 \exp\left[-\frac{1}{T}\left(-e\varphi + \frac{m}{2}\omega(\Omega - \omega)r^2\right)\right]. \quad (2)$$

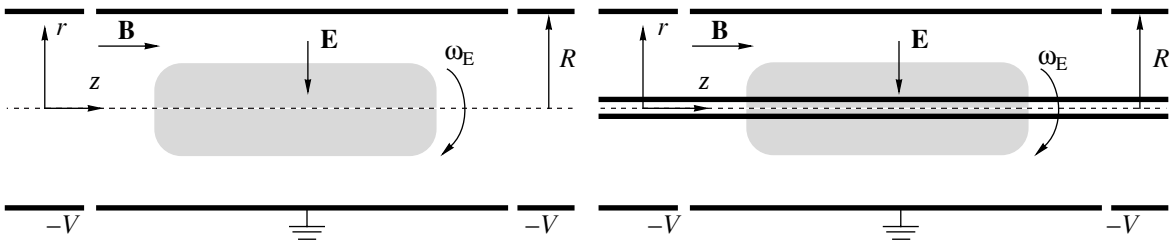

Fig. 1. Schematics of a Malmberg–Penning trap without a central rod (on the left) and with a central rod (on the right).

1063-780X/00/2611-0960$20.00 © 2000 MAIK "Nauka/Interperiodica"

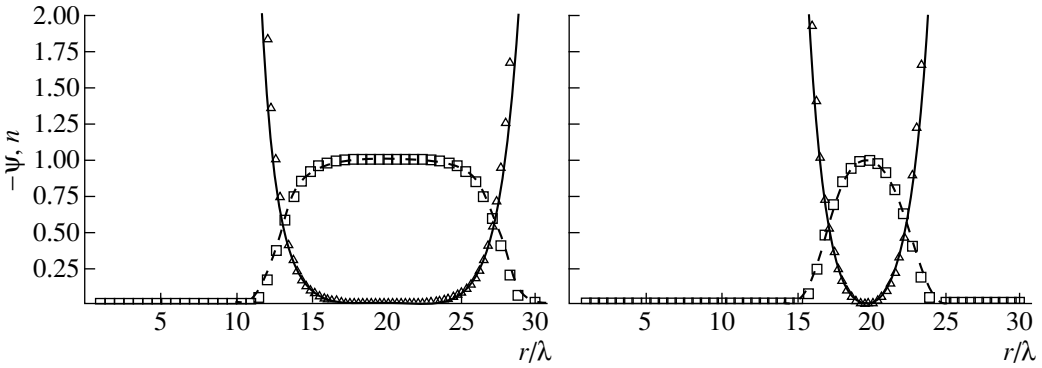

Fig. 2. Effective potential $-\psi$ (solid line) and electron density $n = \exp\psi$ (dashed line) vs. the normalized radius for $\bar{\rho} = 20$ and $\gamma = 10^{-3}$ (on the left) and for $\bar{\rho} = 20$ and $\gamma = 10^{-1}$ (on the right). The approximate solution (7) to Eq. (4) for the effective potential and the corresponding electron density are shown by triangles and squares, respectively.

The self-consistent electric potential is described by Poisson's equation

$$\frac{1}{r}\frac{\partial}{\partial r}r\frac{\partial\varphi}{\partial r} + \frac{\partial^2\varphi}{\partial z^2} = 4\pi en. \tag{3}$$

This equation must be supplemented by the boundary conditions on the walls of the cylinder and central rod. The solution depends on several parameters; however, with a proper scaling of Eq. (3), the number of parameters can be reduced. In terms of the dimensionless potential

$$\psi = \frac{e\varphi}{T} - \frac{m\omega(\Omega-\omega)r^2}{2T}$$

and dimensionless coordinates

$$\rho = \frac{r}{\lambda_D}, \quad \zeta = \frac{z}{\lambda_D},$$

Eq. (3) takes the form

$$\frac{1}{\rho}\frac{\partial}{\partial\rho}\rho\frac{\partial\psi}{\partial\rho} + \frac{\partial^2\psi}{\partial\zeta^2} = [e^{\psi} - 1 - \gamma], \tag{4}$$

where

$$\lambda_D = \sqrt{\frac{T}{4\pi e^2 n_0}},$$

$$\gamma = \frac{2\omega(\Omega-\omega)}{\omega_p^2} - 1,$$

$$\omega_p = \sqrt{\frac{4\pi e^2 n_0}{m}}.$$

Since the density is given by $n = n_0\exp(\psi)$, the plasma resides near the maximum of the effective potential ψ. This maximum value can be set equal to zero because ψ is defined up to an unimportant constant addend. In this case, the parameter n_0 is equal to the maximum plasma density.

We first consider the one-dimensional equilibrium, neglecting the dependence of ψ on ζ. We will look for an annular plasma configuration; hence, we assume that the density profile is peaked at a certain radius $\bar{\rho} > 0$ and that $\psi' = 0$ (where the prime stands for the derivative with respect to ρ) at the same radius. Taking $\psi(\bar{\rho}) = 0$ and $\psi'(\bar{\rho}) = 0$ as the boundary conditions for the potential inside the radial interval of interest, we can find the solution to Poisson's equation. A localized solution exists for $\gamma > 0$. It is governed by the two dimensionless parameters: γ and $\bar{\rho}$. Numerical solutions for given values of γ and $\bar{\rho}$ are presented in Fig. 2. As $\gamma \longrightarrow 0$, the density profile becomes steplike; in contrast, as γ increases, the density profile becomes smoother.

The other parameters can be expressed through ψ and dimensional inputs such as n_0, T, R, and r_d. For example, the charge of the central rod (in terms of $en_0\lambda_D^2$) is equal to

$$q = -\pi[2\rho_d\psi'(\rho_d) + (1+\gamma)\rho_d^2], \tag{5}$$

where $\rho_d = r_d/\lambda_D$, and the potential difference between the external cylinder and internal conductor (in terms of T/e) is given by

$$V = [\psi(\rho) + (1+\gamma)\rho^2/4]_{\rho = r_d/\lambda_D}^{\rho = R/\lambda_D}. \tag{6}$$

Density profiles with an annulus width much larger than the Debye lengths λ_D correspond to $\gamma \longrightarrow 0$. For $\gamma \ll 1$, the annulus parameters relevant to the experimental conditions can be found analytically. Indeed, inside the plasma at $|\psi| \ll 1$, we have $e^{\psi} - 1 \approx \psi$; thus, we obtain

$$\psi \approx \gamma\left[1 - \frac{K_1(\bar{\rho})I_0(\rho) + I_1(\bar{\rho})K_0(\rho)}{K_1(\bar{\rho})I_0(\bar{\rho}) + I_1(\bar{\rho})K_0(\bar{\rho})}\right]. \tag{7}$$

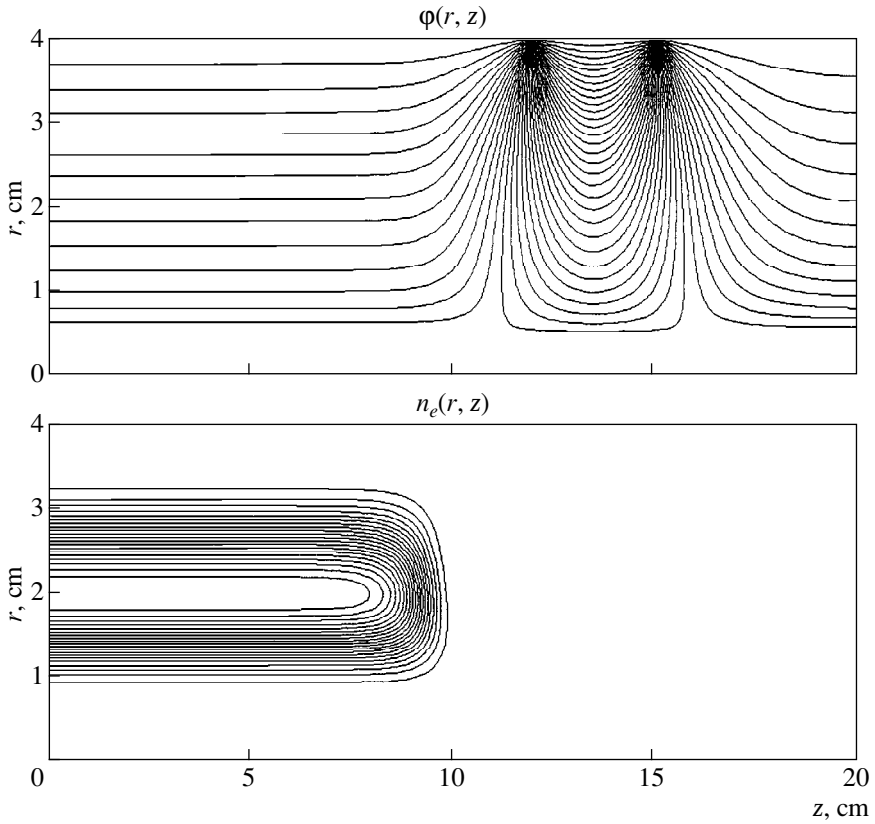

Fig. 3. Contour plots of the electric potential φ (top) and plasma density (bottom) for $\lambda_D = 0.35$ cm, $T = 1.0$ eV, $\gamma = 0.3$, $r_d = 0.5$ cm, $R = 4.0$ cm, $z_{plug1} = 12$ cm, $z_{plug2} = 15$ cm, $V_{wall} = 32.16$ V, $V_{rod} = -8.3$ V, and $V_{plug} = -100$ V.

For $\bar{\rho} \longrightarrow 0$, this solution recovers the result of [6] (see also [7, 9]):

$$\psi \approx \gamma[1 - I_0(\rho)]. \quad (8)$$

In the opposite case ($\bar{\rho} \gg 1$), solution (7) reduces to

$$\psi \approx \gamma[1 - \cosh(\rho - \bar{\rho})]. \quad (9)$$

In this case, the annulus width 2Δ at the density level $n = n_0/e$ can be evaluated as

$$\Delta \approx \ln(2/e\gamma).$$

It is interesting to note that the thermodynamic equilibrium of a plasma with a step density profile can be continuously transformed into the thermodynamic equilibrium of an annular plasma by gathering the entire charge inside the inner radius $\bar{\rho} - \Delta$ on the central rod. Hence, we have

$$q \approx -\pi(\bar{\rho} - \Delta)^2.$$

In the case of a finite plasma length, a two-dimensional thermodynamic equilibrium was obtained by solving Eq. (4) numerically using the finite-difference overrelaxation method. Starting with a certain initial approximation $\psi_0(\rho, \zeta)$ for the effective potential, the solution $\psi_j(\rho, \zeta)$ obtained at the jth iteration step was substituted into the right-hand side of Eq. (4) to yield the next approximate solution $\psi_{j+1}(\rho, \zeta)$ at the $(j + 1)$th step. For simplicity, we assumed that the axisymmetric equilibrium was also symmetric about the midplane $z = 0$. The electrostatic potential was assumed to satisfy the following boundary conditions: $\varphi(r_d, z) = V_{rod}$ on the central rod and $\partial\varphi/\partial z = 0$ at the midplane ($z = 0$) and at the end plate ($z = b$). On the conducting external wall (except the plug section), the potential is equal to $\varphi(R, z) = V_{wall}$; in the plug section, we set $\varphi(R, z) = V_{plug}$. The iteration procedure appeared to be insensitive to the choice of the initial approximation. For a required accuracy better than 10^{-7}, it converges after several hundred iterations.

Results of calculations are shown in Figs. 3–6. As is seen in Fig. 4, the one-dimensional solution provides a good approximation to the density profile $n(r, 0)$ in the midplane of the trap. Excellent agreement is found to be valid even for relatively short plasma clouds. It is seen from Figs. 5 and 6 that the central density profile differs appreciably from that predicted by the one-dimensional theory only for very short (doughnut) plasma clouds.

A nonneutral plasma that is in global thermodynamic equilibrium must be stable against any type of small perturbations. This is valid in particular for the diocotron instability. Earlier experiments found an

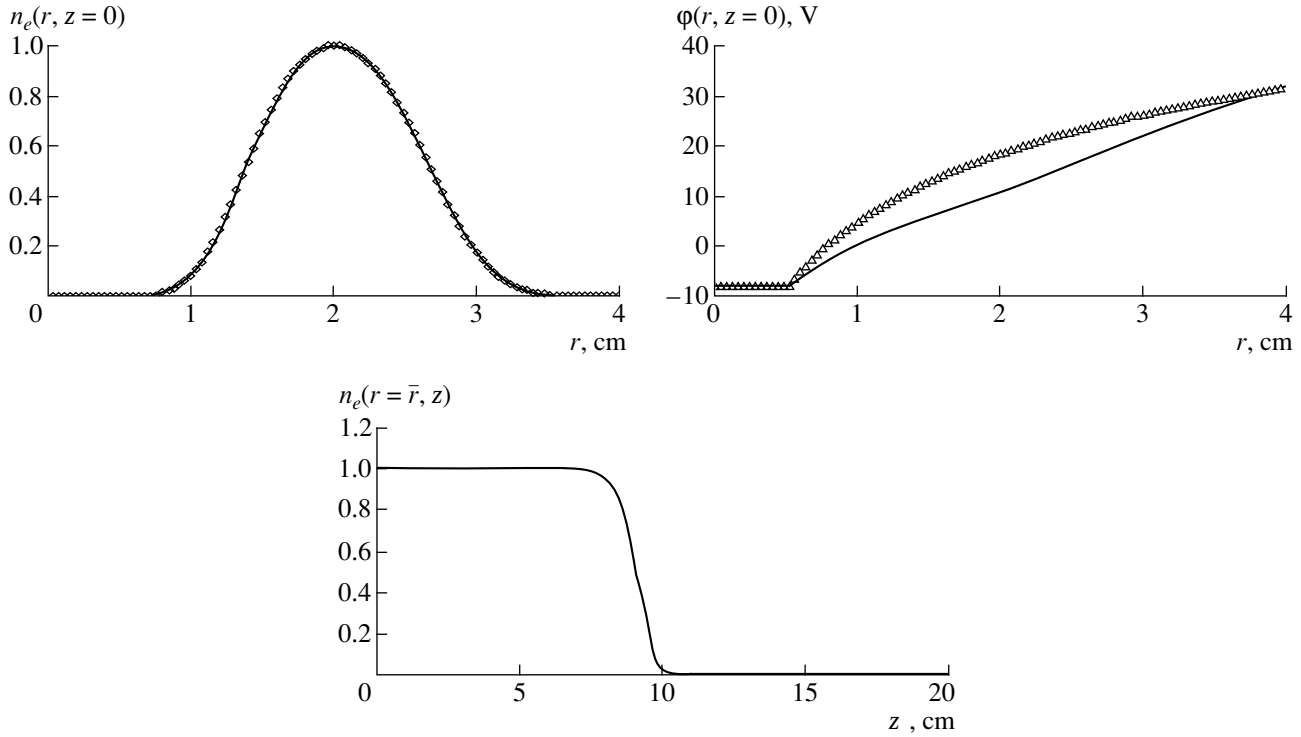

Fig. 4. Radial profiles of the density (top) and potential (middle) in the midplane $z = 0$ and the axial density profile (bottom) at the radius corresponding to the maximum density, $r = \bar{r}$. The parameters are the same as in Fig. 3. The solid line shows the numerical two-dimensional solution, rhombuses (on the top) indicate the numerical one-dimensional solution for the density profile, and the triangles (in the middle) show the two-dimensional vacuum potential profile.

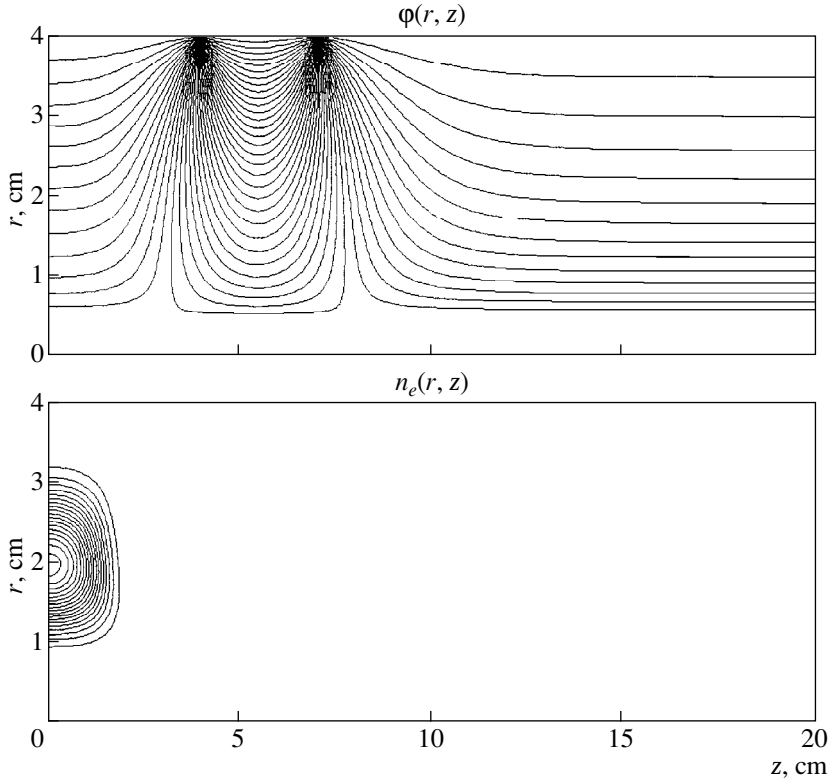

Fig. 5. Contour plots of the electric potential φ (top) and plasma density (bottom) for $z_{plug1} = 4$ cm and $z_{plug2} = 7$ cm; the other parameters are the same as in Fig. 3.

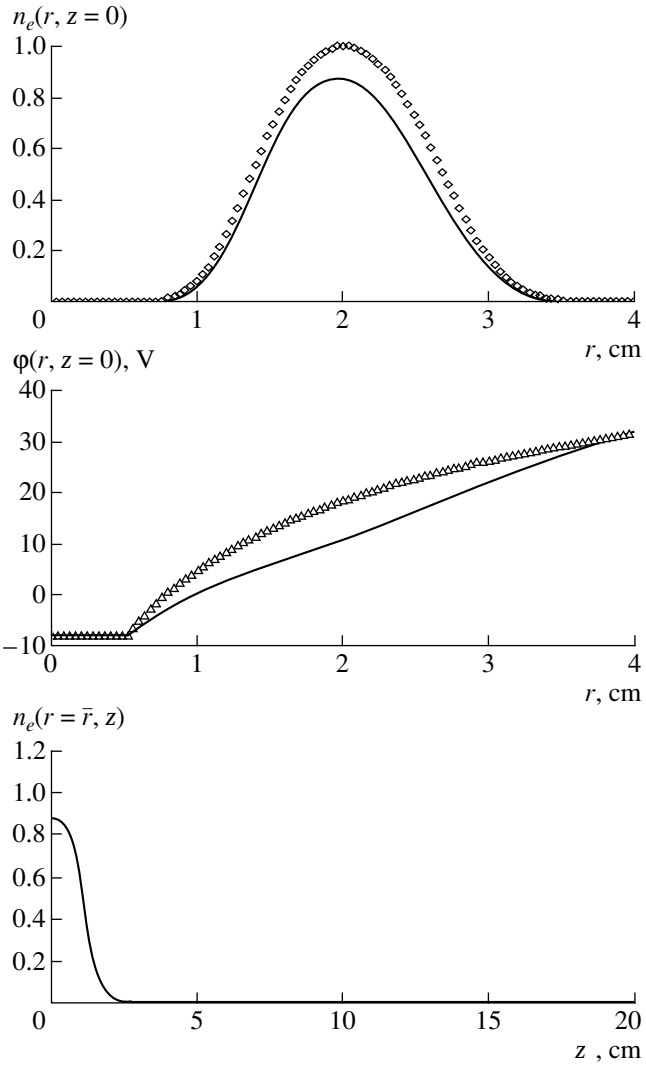

Fig. 6. Radial profiles of the density (top) and potential (middle) in the midplane $z = 0$ and the axial density profile (bottom) at the radius corresponding to the maximum density, $r = \bar{r}$. The parameters are the same as in Fig. 5. The solid line shows the numerical two-dimensional solution, rhombuses (on the top) indicate the numerical one-dimensional solution for the density profile, and the triangles (in the middle) show the two-dimensional vacuum potential profile.

exponentially unstable $m = 1$ diocotron mode for a hollow electron column [10]. We suggest here that adding a central biased rod to the standard configuration of a Malmberg–Penning trap allows one to obtain thermodynamic equilibria with hollow density profiles that are stable against the $m = 1$ diocotron mode.

In fact, a detailed study of the diocotron instability in nonneutral annular plasmas [11] confined in a trap with a biased central electrode has already established the parameter domain where all azimuthal modes are stable. The global thermodynamic equilibrium of the annular nonneutral plasma studied here turns out to be located well inside this domain (to the left of the unstable region shown in Fig. 7 of [11]). Confinement studies of nonneutral annular plasmas were also recently reported in [12]. It was shown in particular that the plasma lifetime was limited by the transport across the magnetic field, although the nature of the transport process remained unclear. We believe that global thermodynamic equilibrium was not achieved in those experiments, because, for the plasma parameters reported in [12], the equilibrium plasma annulus would be much wider than the radial size of the confinement system.

Finally, in view of future applications, it worth noting that our results also apply to the case where the central rod carries a steady longitudinal current, thus changing the magnetic field configuration. Although the plasma dynamics is affected by the presence of the azimuthal magnetic field produced by the longitudinal current, the global thermodynamic equilibrium remains the same as in the zero-current case [8].

ACKNOWLEDGMENTS

This work was supported by the Ministry of University and Scientific Research of Italy according to the agreement between Milan University and Novosibirsk State University.

REFERENCES

1. T. M. O'Neil, Phys. Scr. T **59**, 341 (1995).
2. D. H. E. Dubin and T. M. O'Neil, Phys. Plasmas **5**, 2163 (1998).
3. J. H. Malmberg and C. F. Driscoll, Phys. Rev. Lett. **44**, 654 (1980).
4. T. M. O'Neil, Comm. Plasma Phys. Control. Fusion **5**, 213 (1980).
5. T. M. O'Neil and C. F. Driscoll, Phys. Fluids **22**, 266 (1979).
6. S. A. Prasad and T. M. O'Neil, Phys. Fluids **22**, 278 (1979).
7. D. H. E. Dubin and T. M. O'Neil, Rev. Mod. Phys. **71**, 87 (1999).
8. L. D. Landau and E. M. Lifshitz, *Statistical Physics* (Nauka, Moscow, 1976; Pergamon, Oxford, 1980).
9. T. M. O'Neil and D. H. E. Dubin, Phys. Plasmas **5**, 2163 (1998).
10. C. F. Driscoll, Phys. Rev. Lett. **64**, 645 (1990).
11. G. Rosenthal, G. Dimonte, and A. Y. Wong, Phys. Fluids **30**, 3257 (1987).
12. D. L. Eggleston, Phys. Plasmas **4**, 1196 (1997).
13. T. M. O'Neil and R. A. Smith, Phys. Plasmas **1**, 2430 (1994).

Translated by the authors

Plasma Physics Reports, Vol. 26, No. 11, 2000, pp. 965–971. Translated from Fizika Plazmy, Vol. 26, No. 11, 2000, pp. 1030–1037.

PLASMA DYNAMICS

Steady-State Vortex Structure in a Plasma with a Strong Magnetic Field

A. V. Gordeev* and T. V. Losseva**

**Russian Research Centre Kurchatov Institute, pl. Kurchatova 1, Moscow, 123182 Russia*

***Institute of Geosphere Dynamics, Russian Academy of Sciences, Leninskiĭ pr. 38-6, Moscow, 117979 Russia*

Received February 17, 2000; in final form, June 1, 2000

Abstract—A study is made of nonquasineutral vortex structures in a plasma with a magnetic field B_z in which the charges separate on a spatial scale equal to the magnetic Debye radius $r_B = B_z/4\pi en_e$. The electric field arising due to charge separation leads to radial expansion of the ions, thereby destroying the initial electron vortex. It is shown that the ion pressure gradient stops ion expansion in a nonquasineutral electron vortex and gives rise to a steady structure with a characteristic scale on the order of r_B. With the electron inertia taken into account in the hydrodynamic approximation, the magnetic vortex structure in a hot plasma manifests itself in the appearance of a "hole" in the plasma density. *© 2000 MAIK "Nauka/Interperiodica".*

1. Recent studies of electron vortices in a plasma in a magnetic field have shown that Abrikosov's model [1] fails to correctly describe vortices with a nonquasineutral plasma in the axial region [2, 3]. In addition to the already existing model in which the ions are assumed to be accelerated by the ponderomotive force of a laser pulse, subsequent numerical investigations of the dynamics of such vortices have made it possible to construct an alternative model in which the ion acceleration in a laser pulse is attributed to the space charge–driven expansion (Coulomb explosion) of the vortex [4]. Since the plasma in an electron vortex in a strong magnetic field ($B^2 \gg 4\pi n_e m_e c^2$) is highly nonquasineutral, the ions expand at fairly high velocities on time scales of approximately the reciprocal of the ion plasma frequency. This result is confirmed quite well by experiments and can serve to model a Coulomb explosion in a laser-produced plasma [4–6]. Notably, as early as 1994, Askar'yan *et al.* [7] pointed out that it is necessary to take into account the effects of a quasistatic magnetic field in a laser plasma. Considering the dimensions of the region where the magnetic field is localized and treating the electrons in the relativistic approximation, they, in fact, obtained an order-of-magnitude estimate of the magnetic Debye radius r_B. However, they used a different method with different notation and did not completely clarify the physical meaning of the spatial scale on which the magnetic field is localized. Later, Bulanov *et al.* [8] pointed out that the onset of magnetic vortex structures may significantly affect the evolution of a laser plasma. However, they used Abrikosov's model and neglected the ion dynamics; i.e., they considered static vortices. Note that it is precisely the model proposed in [2–4] to describe electron vortices in a laser plasma that made it possible to develop an alternative model of ion acceleration resulting from the Coulomb explosion of electron vortices in addition to the model of ion acceleration by the ponderomotive force.

In our paper [4], we modeled electron vortices by treating the electrons in the quasistatic approximation, which was adopted because of the slow ion motion during the expansion of a vortex. However, the parameter that is responsible for the quasistatic character of the electrons is small only in the case of moderate magnetic fields, $B^2 \ll 4\pi n_i m_i c^2$. As a result, the magnetic field should lie in the range

$$4\pi n_e m_e c^2 \ll B^2 \ll 4\pi n_i m_i c^2, \qquad (1)$$

which corresponds to the characteristic vortex dimensions [3]

$$c/\omega_{pe} \ll \Delta \ll c/\omega_{pi}. \qquad (2)$$

As Δ approaches c/ω_{pi}, the magnetic field in a vortex increases and the parameter $\epsilon \sim \sqrt{B^2/4\pi n_i m_i c^2}$ that ensures adiabaticity in the motion of the electrons approaches unity, in which case the model of electron vortices in a magnetic field should be constructed with consideration of the ion motion. As the vortex dimension Δ approaches c/ω_{pi}, the ion velocity increases and, at $\Delta \sim c/\omega_{pi}$, it becomes as high as the speed of light [3]. That the ion velocity increases with increasing characteristic vortex dimension was also revealed by Esirkepov *et al.* [9], who simulated ion acceleration by the ponderomotive force of a laser pulse. In a sufficiently weak magnetic field ($\epsilon \ll 1$), the ion velocity in the r-direction is much higher than the ion velocity caused by the inductive electric field, which is directed along the θ-axis, so that we can speak of the radial ion expansion under the action of the electric field of a vortex. In a sufficiently strong magnetic field, the inductive ion

1063-780X/00/2611-0965$20.00

velocity in the θ-direction is also high and the total ion velocity is close to the speed of light.

Simulations of ion expansion under the influence of the electric field revealed the excitation of a collisionless shock wave [4]. During plasma expansion, the electron and ion densities behind the shock front are equalized, but, near the vortex axis, they are both significantly lower than the constant electron and ion densities in a plasma ahead of the front. Consequently, the Coulomb explosion of an electron vortex gives rise to ion motion in the radial direction and causes the formation of a hole in the plasma density around the axis. If the electric field force in a vortex is counterbalanced, e.g., by the ion pressure gradient, then the ions stop expanding and the vortex evolves into a steady state with a reduced plasma density in the axial region. It is the equilibrium vortex structure that will be the subject of our investigations. The plan of the paper is as follows. In Section 2, we present some of the results of [2, 3] in order to make further analysis more clear. In Section 3, we derive the full set of equations describing the dynamics of an electron vortex with the ion pressure taken into account. In Section 4, we describe the vortex structure obtained by numerically solving these dynamic equations by the relaxation method. In Section 5, we calculate the same structure in the steady-state approximation and analyze how the equilibrium structure of the vortex is affected by its dimensions. In Section 6, we summarize the main conclusions of our study.

2. We start with the model of electron vortices that was proposed by Gordeev and Levchenko [2], who showed that the vortex structure is completely governed by the shape of the profile of the Lagrangian invariant I, which is defined as the ratio of the electron vorticity to the electron density: $I = \Omega/n_e$. In our approach, the plasma is assumed to be nonquasineutral on a spatial scale equal to the magnetic Debye radius $r_B \simeq B/4\pi e n_e$.

Simple and consistent equations for electron vortices in a plasma were derived in [10–12]. In those papers, it was shown that taking into account the short spatial scale $r_B \simeq B/4\pi e n_e$ makes it possible to construct a correct model of electron vortices in a plasma. Note that, in previous papers, it was assumed that the vortices exist in the range

$$B^2 \ll 4\pi n_e m_e c^2 \tag{3}$$

corresponding to the spatial scales $r_B \ll c/\omega_{pe}$, in which case the magnetic Debye radius is small and the plasma is only slightly nonquasineutral.

However, the general equations derived in [10–12] are also valid when r_B and c/ω_{pe} satisfy the opposite condition $r_B \gg c/\omega_{pe}$, which corresponds to the range

$$B^2 \gg 4\pi n_e m_e c^2. \tag{4}$$

In [10–12], the equations for electron vortices were obtained using the approximation of cold relativistic electrons without allowance for collisions. In this approximation, the main equation of electron motion has the form

$$\frac{\partial \mathbf{p}_e}{\partial t} + \frac{1}{4\pi e n_e c}\frac{\partial \mathbf{E}}{\partial t} \times \boldsymbol{\Omega} + \nabla \gamma m_e c^2 + \frac{\Omega}{4\pi n_e}\nabla B = -e\mathbf{E}, \tag{5}$$

where Ω is the z-component of the electron vorticity in the magnetic field $\mathbf{B}$ directed along the z-axis ($\Omega = B_z - (c/e)\,(\mathrm{curl}\,\mathbf{p}_e)_z$), $\gamma = (1 - \mathbf{v}_e^2/c^2)^{-1/2}$, $\mathbf{p}_e = \gamma m_e \mathbf{v}_e$, and the electron velocity $\mathbf{v}_e$ is equal to

$$\mathbf{v}_e = -\frac{c}{4\pi e n_e}\nabla \times \mathbf{B} + \frac{1}{4\pi e n_e}\frac{\partial \mathbf{E}}{\partial t}. \tag{6}$$

In deriving Eq. (5), we assumed that the electrons move in the (x, y) plane.

The main difference between the model under consideration and Abrikosov's widely used model [1] is that, along with the equation for the electron vorticity Ω, we use Poisson's equation

$$\mathrm{div}\,\mathbf{E} = 4\pi e(Zn_i - n_e), \tag{7}$$

where n_e and n_i are the electron and ion densities. In other words, the electron density n_e is no longer assumed constant, but should be found from Poisson's equation.

In a steady state, Eqs. (5)–(7) yield the following equations for a cylindrically symmetric vortex [2]:

$$\frac{1}{r}\frac{d}{dr}r\left(m_e c^2 \frac{d\gamma}{dr} + \frac{\Omega}{4\pi n_e}\frac{dB}{dr}\right) = 4\pi e^2(n_e - Zn_i), \tag{8}$$

$$\Omega = B - \frac{m_e c^2}{4\pi e^2}\frac{1}{r}\frac{d}{dr}r\left(\frac{\gamma}{n_e}\frac{dB}{dr}\right). \tag{9}$$

It is important that these equations give the electron density n_e in an explicit form:

$$4\pi\gamma m_e c^2 n_e + \Omega\left(G + \gamma^3 F\frac{m_e c}{e}\right) = G^2 + \gamma^4 F^2\left(\frac{m_e c}{e}\right)^2 + 4\pi m_e c^2 \gamma^3 Z n_i, \tag{10}$$

where the quantities

$$G = B + \gamma F\frac{m_e c}{e}, \quad F = -\frac{v_{e\theta}}{r} > 0$$

satisfy the equations

$$\frac{dG}{dr} = \frac{\Omega - G}{r} - \frac{m_e c}{e}\gamma\frac{F}{r} - \frac{4\pi e n_e}{c}rF, \tag{11}$$

$$\frac{dF}{dr} = \frac{e}{m_e c}\frac{\Omega - G}{\gamma^3 r} - \frac{F}{r}. \quad (12)$$

Relationship (10), which follows from the momentum conservation law, implies that, as the electron vorticity Ω increases, the electron density n_e decreases, because the magnetic field is finite. However, relationship (10) is difficult to apply, because the condition $n_e \geq 0$ imposes restrictions on Ω. For this reason, it is convenient to introduce the quantity $I = \Omega/n_e$ in order for the ion density n to be positive definite regardless of the value of I. The quantity I has an even deeper physical meaning: one can readily see that I is a Lagrangian invariant, because it satisfies the equation

$$\frac{\partial I}{\partial t} + \mathbf{v}_e \cdot \nabla I = 0. \quad (13)$$

Hence, the profile of I is "frozen" in the electron fluid and is carried with it.

Of course, for the electron vortex described by Eqs. (8) and (9), we have $\partial I/\partial t = 0$, because the only nonzero electron velocity component in such a vortex is $v_{e\theta}$ and the condition $\partial I/\partial\theta = 0$ holds. However, with the ion motion taken into account, we have $v_{er} \neq 0$ and $\partial I/\partial t \neq 0$. Therefore, incorporating perturbations into time-independent equations (8) and (9) makes it possible to describe the transport and deformations of the Lagrangian invariant I, which is frozen in the electron fluid, and thereby the evolution of the vortex structure. Note that, in the non-steady-state case, the magnetic field changes at the expense of the induction electric field (in the problem as formulated, this is the electric-field component E_θ) and we can show that Eq. (13) is equivalent to Faraday's law of induction $-(1/c)\partial\mathbf{B}/\partial t = \mathrm{curl}\mathbf{E}$.

We introduce the dimensionless coordinate $\rho = r\sqrt{4\pi e^2 n_{e\infty}/m_e c^2}$ and the dimensionless functions

$$\nu = \frac{n_e}{n_{e\infty}}, \quad g = \frac{G}{\sqrt{4\pi n_{e\infty} m_e c^2}}, \quad f = \frac{F}{\sqrt{4\pi n_{e\infty} e^2/m_e}},$$

$$i = I\sqrt{n_{e\infty}/4\pi m_e c^2}, \quad v = \frac{v_{e\theta}}{c}$$

in order to write the equations for an electron vortex in the final form:

$$\frac{dg}{d\rho} = \frac{\nu i - g}{\rho} - \frac{\gamma f}{\rho} - \nu\rho f, \quad (14)$$

$$\frac{df}{d\rho} = \frac{\nu i - g}{\rho\gamma^3} - \frac{f}{\rho}, \quad (15)$$

where the dimensionless electron density ν is equal to

$$\nu = \frac{\gamma^3 n + g^2 + \gamma^4 f^2}{\gamma + i(g + \gamma^3 f)}, \quad (16)$$

and the rest of the notation is $g = b + \gamma f$, $v = -\rho f$, where $\gamma = (1 - v^2)^{-1/2}$. In contrast to [2], our expression (16) for ν contains the time-varying ion density $n = n_i/n_{i\infty}$. We thus take into account the effect of ion motion on the evolution of the structure of an electron vortex. We can say that Eqs. (14)–(16) define an effective adiabatic functional $b \equiv b[n(\rho)]$ for the ions, which makes it possible to close the ion equations. An approach based on Eqs. (14)–(16) applies to electrons treated in the quasi-static approximation $r_B/ct_0 < 1$, which corresponds to the range $B^2 < 4\pi n_i m_i c^2$.

Note that we are not going to introduce the electron temperature, although its effects are analogous to the effects of the ion temperature.

Recall that the structure of an electron vortex is completely governed by the shape of the profile of the Lagrangian invariant i, in which case the only physical boundary condition is that the electron velocity vanishes at infinity, $v(\rho = \infty) = 0$. This boundary condition enables us to determine the actual eigenvalue of the problem—the magnetic field at the vortex axis. Also, our problem assumes an obvious boundary condition at the vortex axis: $v(\rho = 0) = db/d\rho|_{\rho=0} = 0$.

3. The above set of equations describes a so-called Coulomb explosion—the radial expansion of ions in the radial electric field E_r [4]. Note that, for laser filaments in a plasma, the Coulomb explosion concept (which implies that the ions expand under the action of electrostatic forces on time scales of approximately the inverse ion plasma frequency) was developed as early as 1990 by Burnett and Enright [13]. It is interesting to note that they obtained a quite reliable estimate for the characteristic energy of the expanding ions: $\varepsilon_i \sim m_e c^2$.

According to [2–4], the structure of an electron vortex during such an expansion is affected by the nonuniform ion density, which acts to change the magnetic field structure and destroy the vortex. Note that, since the ion dynamics is much slower than the electron dynamics, the equations for the vortex structure do not contain the ion velocity.

We describe the ions by the hydrodynamic equations

$$m_i\frac{d\mathbf{v}_i}{dt} = Ze\mathbf{E} + \frac{Ze}{c}\mathbf{v}_i \times \mathbf{B} - \frac{\nabla p_i}{n_i}, \quad (17)$$

$$\frac{\partial n_i}{\partial t} + \mathrm{div}(n_i\mathbf{v}_i) = 0. \quad (18)$$

Unlike in [4], these equations contain the ion pressure (which is described here by the conventional adiabatic equation of state with an adiabatic index equal to 2). We emphasize that the ion currents play no role in the formation of vortices whose dimensions obey conditions (2), so that, in analogy with [4], the vortex equations contain the ion density and do not include the ion currents (see [14]).

Note also that the gradient of the kinetic ion pressure can counterbalance the radial electric force acting on the ions, thereby ensuring that the vortex is in equilibrium.

We will say a few words about the importance of Eq. (13) for the Lagrangian invariant. By virtue of the cylindrical symmetry of the problem, the only parameter in Eq. (13) is the radial electron velocity:

$$\frac{\partial I}{\partial t} + v_{er}\frac{\partial I}{\partial r} = 0. \tag{19}$$

The Maxwell equations imply that, by virtue of the axial symmetry, the term with the magnetic field drops out of the expression for the radial electron velocity,

$$v_{er} = \frac{Zn_i}{n_e}v_{ir} + \frac{1}{4\pi e n_e}\frac{\partial E_r}{\partial t}; \tag{20}$$

as a result, the radial dynamics of the Lagrangian invariant I is determined by the characteristic ion velocity.

Note that, in the non-steady-state case, the symmetry properties of the problem are responsible for the appearance of the induction electric field E_θ, which changes the magnetic field B_z. However, as will be seen from the following considerations, our equations do not explicitly include E_θ and Faraday's law of induction turns out to be equivalent to Eq. (13) for the electron Lagrangian invariant I. Hence, Eq. (13) for the Lagrangian invariant I provides a convenient tool for describing the evolution of vortex structures.

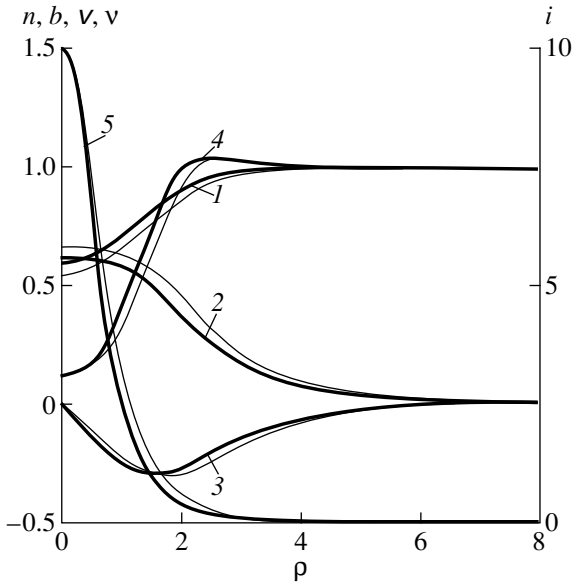

Fig. 1. Profiles of (*1*) the ion density n, (*2*) the magnetic field b, (*3*) the azimuthal electron velocity v, (*4*) the electron density ν, and (*5*) the Lagrangian invariant i calculated by the relaxation method (light curves) and obtained from the time-independent equations (heavy curves).

We introduce the characteristic time t_0 and the characteristic ion velocity v_0,

$$t_0 = \sqrt{\frac{m_i}{4\pi e^2 Z n_{e\infty}}}, \quad v_0 = c\sqrt{\frac{Zm_e}{m_i}}, \tag{21}$$

in order to convert Eqs. (17)–(19) into dimensionless form:

$$\frac{\partial u}{\partial \tau} + u\frac{\partial u}{\partial \rho} = -\frac{\partial \gamma}{\partial \rho} - i\frac{\partial b}{\partial \rho} - \lambda\frac{\partial n}{\partial \rho},$$
$$\frac{\partial n}{\partial \tau} + \frac{1}{\rho}\frac{\partial}{\partial \rho}(\rho n u) = 0, \tag{22}$$

$$\frac{\partial i}{\partial \tau} + \left\{\frac{n}{\nu}u + \frac{1}{\nu}\frac{\partial}{\partial \tau}\left(\frac{\partial u}{\partial \tau} + u\frac{\partial u}{\partial \rho} + \lambda\frac{\partial n}{\partial \rho}\right)\right\}\frac{\partial i}{\partial \rho} = 0, \tag{23}$$

where $\tau = t/t_0$, $u = v_{ir}/v_0$, $b = B/\sqrt{4\pi n_{e\infty} m_e c^2}$, and $n_{e\infty} = Zn_{i\infty}$ is the electron density at infinity.

In analogy with [4], we can neglect slow ion motion in the θ-direction, because, for magnetic fields satisfying conditions (1), the induction effects are insignificant.

The above set of equations describes an electron vortex in the quasistatic approximation [Eqs. (14)–(16)] and the evolution of the ions and electron Lagrangian invariant during slow ion motion [Eqs. (22), (23)]. When the ion pressure is neglected, the expanding ions give rise to a collisionless shock wave, which was considered in [4]. The ion pressure gradient acts to decelerate the expanding ions; as a result, an electron vortex evolves into a steady state.

The boundary conditions for the ion equations imply that the radial ion velocity vanishes at the vortex axis, $u(\rho = 0) = 0$, and, at infinity, $u(\rho = \infty) = 0$. At infinity, the ion density should be constant, $n(\rho = \infty) = 1$, and, at $\lambda \neq 0$, it should satisfy the condition $\partial n/\partial \rho|_{\rho = 0} = 0$. The initial conditions for the ions along the ρ-axis are $n(\tau = 0) = 1$ and $u(\tau = 0) = 0$.

The initial structure of an electron vortex is assumed to correspond to that against the background of the immobile ions.

4. In calculations, we normalized the ion pressure as $p_i = n_{e\infty} m_e c^2 \lambda n^2/2$. It is seen that the characteristic ion temperature at $n \sim 1$ is equal to $m_e c^2$ and the factor λ can be varied in a certain range. A steady electron vortex was simulated by numerically solving the above set of equations by the relaxation method. The initial vortex structure was assumed to correspond to that of a purely electron vortex at a constant ion density n_i = const. The resulting vortex structure for $\lambda = 1$ is illustrated by the light curves in Fig. 1. We can see a dip in the plasma density profile in the axial region (in other words, a hole forms in the plasma density); moreover, in the vicinity of the vortex axis, the ion density n is higher than the

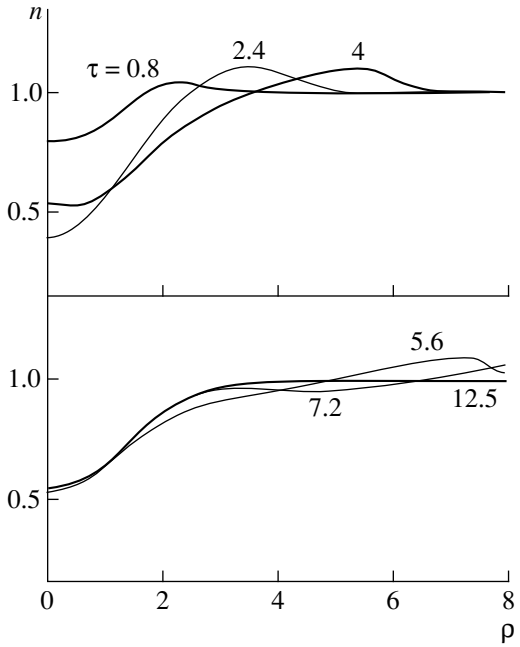

Fig. 2. Relaxation to a steady vortex structure. Profiles of the dimensionless ion density n are shown at subsequent times τ.

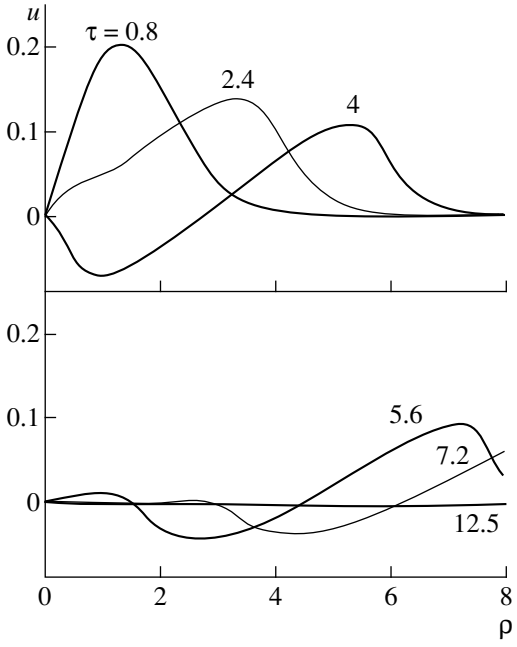

Fig. 3. Relaxation to a steady vortex structure. Profiles of the dimensionless radial ion velocity u are shown at subsequent times τ.

electron density ν. The results of calculations allow us to trace the process of gradual relaxation to a steady vortex structure. The values of the ion density n and ion velocity u at different times are presented in Figs. 2 and 3. The profiles in these figures were obtained with the help of a modified nonlinear monotonic algorithm for calculating transport processes by the flux correction method [15]. We can see that, during the transient relaxation process, the perturbations of n and u are damped.

5. In this section, we calculate a steady vortex structure from the time-independent equations (14)–(16) with the ion density found from the first equation in (22). In this equation, we set $\partial/\partial t \equiv 0$ and $u = 0$ and integrate the resulting equation to obtain

$$\lambda n = \lambda + 1 - \gamma + \int_{\rho}^{\infty} i\frac{\partial b}{\partial \rho} d\rho. \qquad (24)$$

In Fig. 1, the heavy curves, which were calculated for $\lambda = 1$, illustrate the vortex structure determined by solving the time-independent equation for the typical vortex dimension $\delta = 1$ (here, the dimension δ characterizing the initial profile of the Lagrangian invariant i is expressed in units of c/ω_{pe} for an unperturbed state). We find a good agreement between the profiles obtained using the above two methods. Note that the vortex structure with such a profile of the Lagrangian invariant $i(\rho)$ can be in equilibrium in a certain range of λ values. However, there exists a minimum possible value of λ, which corresponds to the lowest ion density at the center of the "vortex hole"; at $\delta = 1$, this minimum value of λ is equal to 0.7. It is of interest to analyze how the shapes of the profiles change as the characteristic dimension δ for the Lagrangian invariant i increases. The larger the dimension δ, the higher the magnetic field in the vortex. Figure 4 shows how the difference between the electron and ion densities at the vortex axis varies as a function of the characteristic dimension for the Lagrangian invariant i. One can see that, as the char-

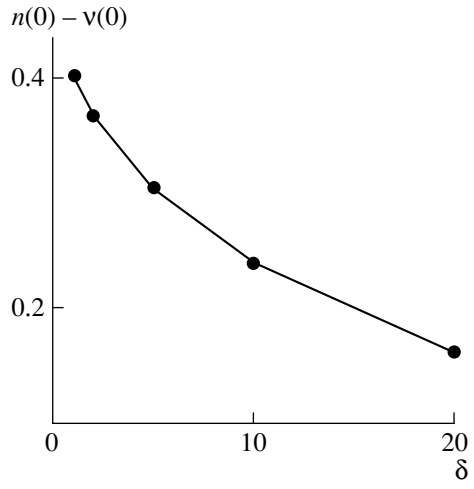

Fig. 4. Difference between the ion and electron densities at the vortex axis, $n(0) - \nu(0)$, vs. the dimension δ characterizing the initial profile of the Lagrangian invariant i.

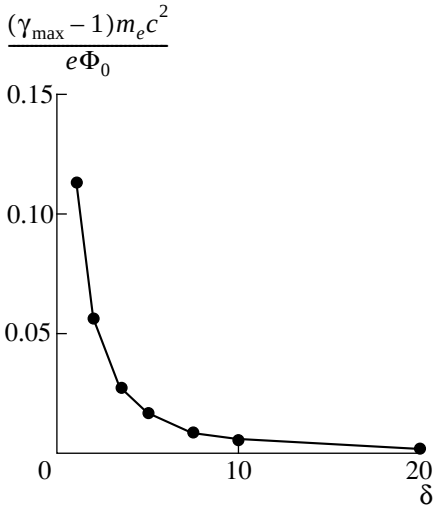

Fig. 5. Ratio of the maximum electron kinetic energy $(\gamma_{max} - 1)m_ec^2$ to the maximum (at the vortex axis) electron potential energy $e\Phi_0$.

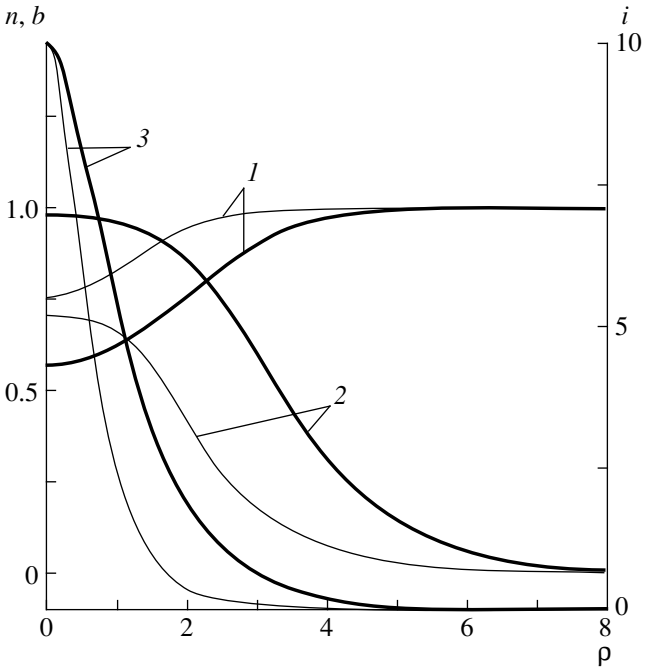

Fig. 6. Profiles of (*1*) the ion density *n*, (*2*) the magnetic field *b*, and (*3*) the Lagrangian invariant *i* in a steady vortex configuration at $\rho \longrightarrow \infty$ for a profile $i(\rho)$ decreasing according to a power law (light curves) and for an exponentially decreasing profile $i(\rho)$ (heavy curves).

acteristic dimension increases, the difference $n(0) - \nu(0)$ decreases. Hence, for large dimensions δ, the hole that forms in the ion density is almost quasineutral. Note that, in calculating the equilibrium vortex structure, we used the minimum possible value of λ for each value of δ.

Our steady-state model makes it possible to analyze the role of electron inertia in the formation of electron vortices of different dimensions. Let us consider strong magnetic fields and, accordingly, high electric potentials; i.e., we assume that $B_z^2 \gg 4\pi n_e m_e c^2$. In accordance with the relationship between the Hall electric potential Φ and the magnetic field, this inequality can also be written as

$$e\Phi \sim \frac{B_z^2}{4\pi n_e} \gg m_e c^2. \qquad (25)$$

We can see that electron inertia can be neglected. However, we do not rule out the possibility that the factor γ may grow without bound. For this reason, we must exactly determine the maximum value of γ. Our calculations based on the hydrodynamic equations show that the factor γ does not grow excessively with increasing vortex dimensions.

Figure 5 displays the quantity $(\gamma_{max} - 1)m_ec^2/e\Phi_0$ versus the vortex dimension. Here, γ_{max} is the maximum value of γ over the electron vortex and Φ_0 is the highest value of the electric potential (at the vortex axis). We can see that electron inertia plays a particularly important role in the formation of small-size vortices (which are characterized by low electric potentials) and can be completely neglected for larger-size vortices such that $\delta \gg 1$.

It is interesting to note that the situation with ion diodes is essentially the same: the higher the potential in a diode, the smaller the role of the electron inertia [16]. We stress that, when electron inertia is neglected, the overall vortex structure changes radically: a peak (rather than a dip) forms in the ion density profile at the vortex axis.

In [2–4], the radial profile of the Lagrangian invariant was chosen to decrease sharply according to a power law: $i = i_0/(1 + \rho^2)^2$. However, the asymptotic behavior of the magnetic field in a real electron vortex is better described by the invariants $i(\rho)$ that decrease exponentially at infinity. This circumstance is not of fundamental importance for numerical integration over finite radial intervals. However, in some time-dependent problems in which a perturbation in the form of a nonlinear wave can propagate over large distances in the radial direction, exponentially decreasing profiles can yield far more exact results than the profiles decreasing according to a power law. To illustrate this point, Fig. 6 shows the results of computations for the exponentially decreasing profile $i = i_0 (1 + \rho)/(1 + \rho \exp\rho)$ of the Lagrangian invariant. At the same value $i(0)$, the exponential profile $i(\rho)$ yields a wider vortex and leads to larger equilibrium values of λ in comparison with those calculated for the power-law profile. The profiles shown in Fig. 6 are characteristic of steady vortex structures with $\lambda = 2$ and with the power-law and exponential profiles of *i*.

6. Our investigations demonstrate the possibility of the formation of steady plasma vortices in which the plasma electrons drift in crossed electric and magnetic

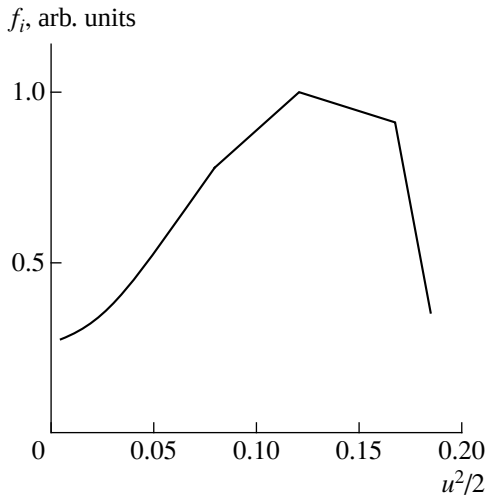

Fig. 7. Resulting ion distribution function in a collisionless shock wave during the formation of a nonquasineutral shock front. The abscissa is the characteristic ion energy normalized to Zm_ec^2.

fields in the θ-direction and the ion plasma component is in equilibrium because of the balance between the electric force and the ion pressure gradient. In calculating such equilibrium vortices, we assume that the ions start to expand in an unsteady fashion under the action of the radial electric field. The radial profile of the velocity acquired by the ions accelerated at the front of an expanding shock wave corresponds to the ion velocity distribution function at the shock front (see Fig. 7). In constructing the steady-state vortex solution, we determined the ion pressure from the "temperature" that is characteristic of this distribution function. In the hydrodynamic approximation, taking into account electron inertia leads to a decrease in the plasma density in the axial region; in other words, we can say that a hole appears in the plasma density around the vortex axis.

We have shown that, although the electron kinetic energy in such vortices is low, a self-consistent steady-state solution should be constructed with allowance for electron inertia. In fact, neglecting electron inertia leads to a radically different equilibrium solution: at a constant electron density, the ion density profile is peaked at the vortex axis, in which case the plasma charge at the axis remains positive.

The electron vortices under discussion should form as a result of the onset of the Buneman electromagnetic instability [17]. The study of such vortices may prove to be useful for investigating the magnetic field evolution in a plasma. Thus, the equilibrium vortex structure analyzed above may correspond to a hot plasma with a "floating" magnetic vortex in which the plasma density is reduced.

The most important result of our study is the demonstration that a steady vortex structure may form in a magnetic field in a plasma with a nonzero ion pressure.

ACKNOWLEDGMENTS

A.V. Gordeev is grateful to I.A. Ivonin for fruitful discussions. This work was supported in part by the Russian Foundation for Basic Research, project nos. 97-02-16980, 00-02-16305, and 98-02-17174.

REFERENCES

1. A. A. Abrikosov, Zh. Éksp. Teor. Fiz. **32**, 1442 (1957) [Sov. Phys. JETP **5**, 1174 (1957)].
2. A. V. Gordeev and S. V. Levchenko, Pis'ma Zh. Éksp. Teor. Fiz. **67**, 461 (1998) [JETP Lett. **67**, 482 (1998)].
3. A. V. Gordeev and S. V. Levchenko, Electromagn. Waves Electron. Syst. **3** (2–3), 25 (1998).
4. A. V. Gordeev and T. V. Losseva, Pis'ma Zh. Éksp. Teor. Fiz. **70**, 669 (1999) [JETP Lett. **70**, 684 (1999)].
5. G. S. Sarkisov, V. Yu. Bychenkov, V. T. Tikhonchuk, *et al.*, Pis'ma Zh. Éksp. Teor. Fiz. **66**, 787 (1997) [JETP Lett. **66**, 828 (1997)]; G. S. Sarkisov, V. Yu. Bychenkov, V. N. Novikov, and V. T. Tikhonchuk, Phys. Rev. E **59**, 7042 (1999).
6. G. S. Sarkisov, V. Yu. Bychenkov, and V. T. Tikhonchuk, Pis'ma Zh. Éksp. Teor. Fiz. **69**, 20 (1999) [JETP Lett. **69**, 20 (1999)].
7. G. A. Askar'yan, S. V. Bulanov, F. Pegoraro, and A. M. Pukhov, Pis'ma Zh. Éksp. Teor. Fiz. **60**, 240 (1994) [JETP Lett. **60**, 251 (1994)]; Fiz. Plazmy **21**, 884 (1995) [Plasma Phys. Rep. **21**, 835 (1995)].
8. S. V. Bulanov, M. Lontano, T. Zh. Esirkepov, *et al.*, Phys. Rev. Lett. **76**, 3562 (1996); S. V. Bulanov, V. A. Vshivkov, G. I. Dudnikova, *et al.*, Fiz. Plazmy **23**, 284 (1997) [Plasma Phys. Rep. **23**, 259 (1997)].
9. T. Zh. Esirkepov, Y. Sentoku, K. Mima, *et al.*, Pis'ma Zh. Éksp. Teor. Fiz. **70**, 80 (1999) [JETP Lett. **70**, 82 (1999)].
10. A. V. Gordeev, Preprint No. 5928/6 (Institute of Nuclear Fusion, Russian Research Centre Kurchatov Institute, Moscow, 1995).
11. A. V. Gordeev, Fiz. Plazmy **23**, 108 (1997) [Plasma Phys. Rep. **23**, 92 (1997)].
12. A. V. Gordeev and S. V. Levchenko, in *Proceedings of the 18th Symposium on Plasma Physics and Technology, Prague, 1997*, p. 74.
13. N. H. Burnett and G. D. Enright, IEEE J. Quantum Electron. **26**, 1797 (1990).
14. A. V. Gordeev, A. S. Kingsep, and L. I. Rudakov, Phys. Rep. **243**, 215 (1994).
15. E. S. Oran and J. P. Boris, *Numerical Simulation of Reactive Flow* (Elsevier, New York, 1987; Mir, Moscow, 1990).
16. A. V. Gordeev and S. V. Levchenko, Fiz. Plazmy **25**, 217 (1999) [Plasma Phys. Rep. **25**, 193 (1999)].
17. A. V. Gordeev, Fiz. Plazmy **20**, 955 (1994) [Plasma Phys. Rep. **20**, 855 (1994)].

Translated by O. Khadin

Plasma Physics Reports, Vol. 26, No. 11, 2000, pp. 972–979. Translated from Fizika Plazmy, Vol. 26, No. 11, 2000, pp. 1038–1045.

LOW-TEMPERATURE PLASMA

Nonlocal Nature of the Electron Energy Spectrum in a Glow Discharge in Pure O_2: I. Nonlocal Character of the Electron Distribution Function

V. V. Ivanov, K. S. Klopovskiĭ, D. V. Lopaev, A. T. Rakhimov, and T. V. Rakhimova

Skobeltsyn Institute of Nuclear Physics, Moscow State University, Vorob'evy gory, Moscow, 119899 Russia

Received April 3, 2000

Abstract—A study is made of the nonlocal nature of the electron energy distribution function in the positive column of a glow discharge in a tube filled with pure oxygen. The distribution function and the axial (E_z) and radial (E_r) electric fields as functions of radius are measured using an array of mobile probes. The experimentally obtained spatial profiles of the distribution function are used to test the applicability of the two-term approximation to the distribution function of the electrons with a nonlocal energy spectrum. The distribution function in a specified electric field $\mathbf{E} = \mathbf{E}_z + \mathbf{E}_r$ (where $\mathbf{E}_z \perp \mathbf{E}_r$) is calculated by solving the coordinate-dependent Boltzmann equation in the two-term approximation and by directly integrating the equations of electron motion using the Monte Carlo method. A comparison between the experimental data and the results of simulations carried out for a broad parameter range shows that, in the case of a highly nonlocal electron energy spectrum, the two-term approximation makes it possible to calculate the electron distribution function with a fairly good accuracy, in which case, however, in imposing the boundary conditions, the electron losses at the plasma surface should be treated in the kinetic approximation. It is shown that using the reflection coefficient of the plasma surface for electrons instead of the loss cone in space makes it possible to accurately calculate the electron energy distribution function over the entire parameter range under consideration, including the transient region in which the electron-energy relaxation length is comparable to the characteristic plasma dimension.

1. INTRODUCTION

Present-day plasma technologies related to microelectronics and the production of thin films deal mainly with large-area dense homogeneous plasmas created by alternating electric field–driven low-pressure discharges. This circumstance has stimulated increased interest in studying such discharges. The development of discharge models is a key problem in theoretical investigations aimed at searching for new technological applications and further technological developments.

Calculation of the electron distribution function (EDF), which determines the rate constants of the most important elementary processes and transport coefficients in a plasma, is a central issue in modeling gas-discharges. In a spatially nonuniform electric field $F(\mathbf{v}, \mathbf{r}, t)$, the EDF $\mathbf{E}(\mathbf{r}, t)$ generally depends on seven variables and can be found from the Boltzmann kinetic equation

$$\frac{\partial F(\mathbf{v}, \mathbf{r}, t)}{\partial t} + \mathbf{v} \cdot \frac{\partial F(\mathbf{v}, \mathbf{r}, t)}{\partial \mathbf{r}} + \frac{e\mathbf{E}(\boldsymbol{r}, t)}{m_e} \cdot \frac{\partial F(\mathbf{v}, \mathbf{r}, t)}{\partial \mathbf{v}} = Q, \quad (1)$$

where $\mathbf{r}$ is the position vector; $\mathbf{v}$ is the electron velocity; the collision integral Q determines how $F(\mathbf{v}, \mathbf{r}, t)$ changes in elastic and inelastic collisions; $\mathbf{E}(\mathbf{r}, t)$ is the electric field; and e and m_e are the charge and mass of an electron, respectively. Since an efficient general algorithm for solving Eq. (1) is lacking, various simplifying approaches and approximations are used for this purpose. This naturally brings up the question of the accuracy of the solution method and its applicability range. In solving certain problems, it is often difficult to determine with considerable confidence the degree of accuracy of specific approaches. The reason for this is that the EDF is affected by a variety of factors (from "microparameters," such as the structure of the electron flow scattered by gas particles, to "macroparameters," such as the way in which the discharge is initiated and the presence of active particles). That is why there is some uncertainty regarding the applicability ranges of discharge models. However, to some extent, all approaches for calculating the EDF and, accordingly, for modeling discharges can be compared from the standpoint of their ability to describe the effects of anisotropic processes and nonlocal electron energy spectra. Figure 1 illustrates the applicability ranges of the most widely used approaches in the plane of the parameters F_1/F_0 and Λ_ε/L, where F_0 and F_1 are the isotropic and anisotropic parts of the EDF; L is the scale length on which the plasma density varies; and Λ_ε is the electron-energy relaxation length defined as $\Lambda_\varepsilon = \sqrt{\lambda_m \lambda^*}$ [1], with λ_m and λ^* being the electron mean

1063-780X/00/2611-0972$20.00 © 2000 MAIK "Nauka/Interperiodica"

free paths with respect to elastic and inelastic collisions. Of course, since Fig. 1 merely illustrates the applicability ranges of different models, the boundaries are fairly arbitrary.

One of the most widely used approximations, specifically, the approximation in which the "local" distribution function is evaluated under the assumption that the plasma is homogeneous, is valid when $L \gg \Lambda_\varepsilon$. However, the dimensions of real discharge devices operating at reduced pressures satisfy the opposite inequality; consequently, in solving the Boltzmann equation, we cannot assume that the plasma is spatially homogeneous. In an inhomogeneous plasma, the EDF is not determined by the local electric fields, so that, in this sense, it is "nonlocal." The spatial profiles of the EDF can be evaluated by solving the kinetic equation (1) using different approaches. Physically, the most insightful approach [1–5] is that based on the assumption that the total electron energy in a weakly collisional plasma is approximately conserved; this approach makes it possible to calculate the spatial profiles of the EDF treated as a function of the total electron energy. Approaches in which the coordinate-dependent Boltzmann equation is solved directly by various numerical methods are more involved and, accordingly, require large amounts of computer time [6–11]. The most exact solutions can be obtained by directly integrating the equations of electron motion in a prescribed potential by the Monte Carlo (MC) method [12–14] or in a self-consistent potential by the combined particle-in-cell–Monte Carlo (PIC–MC) method [15–18]. (Various approaches to determining EDFs in plasmas were considered in detail in the collection of articles [19].) In order to calculate EDFs whose anisotropy is so high that the applicability of approximate models is questionable, it is especially important to employ exact numerical methods. However, at present, the applicability of the MC method is restricted because of the enormous computational resources required and lack of experimental data on the differential scattering cross sections. In this connection, it becomes relevant to develop simpler methods for calculating EDFs with allowance for spatial nonlocal effects. The "hybrid" models based on such methods (see, e.g., [20, 21]) extend the applicability ranges of particular approaches (Fig. 1) and make it possible to develop much faster computer codes.

A low-pressure glow discharge in a long cylindrical tube with a longitudinal electric field is one of the most convenient objects for experimental and theoretical analyses of the nonlocal and anisotropic nature of the EDF and also various plasmochemical processes. The main feature of such discharges is that they are, on the one hand, highly nonequilibrium and spatially inhomogeneous in the radial direction and, on the other hand, isotropic and homogeneous along the tube axis. In electronegative gases, glow discharges are usually stable in the parameter range $pd > 0.1$ torr cm (where p is the pressure and d is the characteristic plasma column diameter). In many cases, the radial electric field E_r is only incorporated into the macroscopic electrodynamic equations and is neglected in the kinetic equation for the EDF, which is assumed to depend only on the longitudinal uniform field E_z. In this paper, we analyze the applicability of the two-term approximation (TTA) for the EDF in a spatially nonuniform field $\mathbf{E} = \mathbf{E}_z + \mathbf{E}_r$ (where $\mathbf{E}_z \perp \mathbf{E}_r$) by comparing the results of MC simulations with experimental data on dc discharges in pure oxygen in the range $pd \approx 0.15$–1.5 torr cm (where d is the tube diameter), for which we have $\Lambda_\varepsilon > L$ at $pd = 0.15$ torr cm and $\Lambda_\varepsilon < L$ at $pd \approx 1.5$ torr cm. Note that the cross sections for electron scattering by oxygen molecules are such that the EDF is nearly isotropic everywhere except for a high-energy range corresponding to electron-impact ionization. Consequently, we can hope that, in solving Eq. (1), the EDF can be evaluated in the TTA. However, we must keep in mind that for many polyatomic gases (CF_4, SF_6, etc.) the TTA may become inapplicable even in the range of moderate

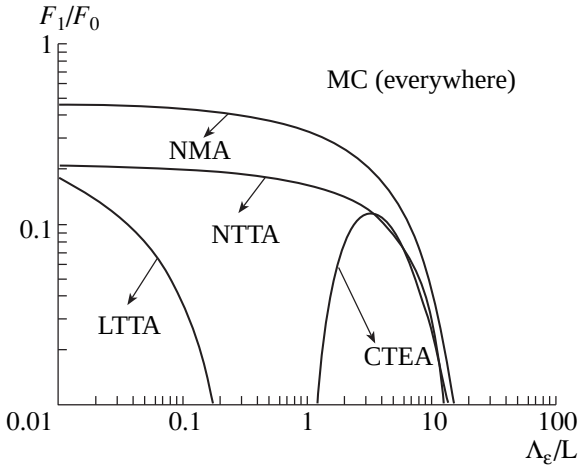

Fig. 1. Approximate applicability ranges of the approaches that are most widely used in solving the Boltzmann kinetic equation (1) for the EEDF in the plane of the parameters F_1/F_0 and Λ_ε/L, where F_0 and F_1 are the isotropic and anisotropic parts of the EDF, L is the scale length on which the plasma density varies, and Λ_ε is the electron-energy relaxation length defined as $\Lambda_\varepsilon = \sqrt{\lambda_m \lambda^*}$ [1], with λ_m and λ^* being the electron mean free paths with respect to elastic and inelastic collisions. The applicability ranges are bounded by the coordinate axes and the curves. The arrows mark the applicability ranges of the following approaches: the local two-term approximation (LTTA), which is based on solving the coordinate-independent Boltzmann equation; the nonlocal two-term approximation (NTTA), which is based on solving the coordinate-dependent Boltzmann equation; the nonlocal multiterm approximation (NMA), which is based on solving the set of coupled coordinate-dependent kinetic equations; the "conserved total energy" approximation (CTEA), which is based on solving the generalized Boltzmann equation that is homogeneous in the total energy; and the MC method, which implies direct integration of the equations for electron motion.

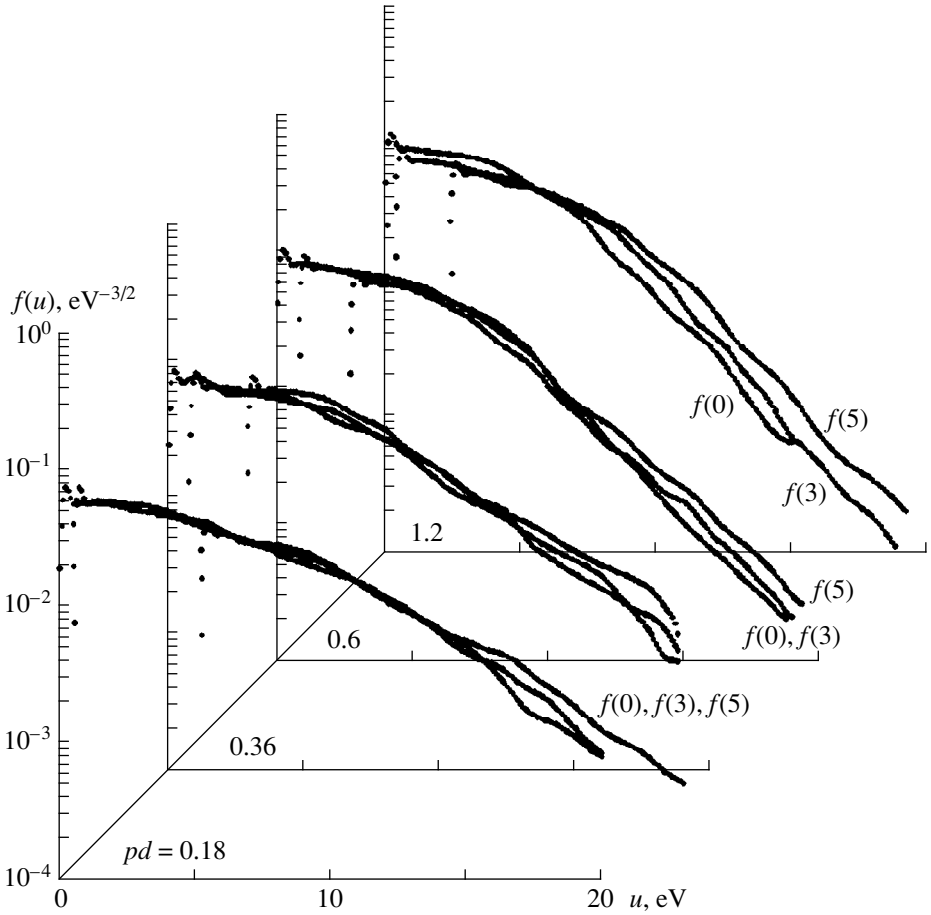

Fig. 2. Experimentally measured EEDFs vs. the total electron energy $u = \varepsilon + e\varphi$ (where ε is the kinetic energy of the electrons and $e\varphi$ is their potential energy) at a fixed discharge current density of 5 mA/cm ^{2} for pd = 0.18, 0.36, 0.6, and 1.2 torr cm. The curves $f(0)$, $f(3)$, and $f(5)$ refer to the radial positions r = 0 (the discharge axis), 3, and 5 mm.

energies because of the large inelastic losses corresponding to the high anisotropy of the EDF [22].

In an O_2 plasma, the discharge electrodynamics is strongly affected by active particles (oxygen atoms and metastable molecules) [23–26]. In addition, the radial plasma potential is largely governed by the heating of negative ions in strong longitudinal electric fields and also ion–molecule charge-exchange and detachment reactions [22, 25]. Therefore, a complete self-consistent discharge model should incorporate all of the above processes. In simulations, we used the experimentally measured fields $E_r(r)$ and E_z in order to simplify matters and to analyze the applicability of the TTA more correctly.

2. EXPERIMENT

We carried out a comprehensive study of a glow discharge in a glass tube (with the inner diameter d = 12 mm and an interelectrode distance of 490 mm) filled with pure O_2 over the pressure range from 0.15 to 6 torr at current densities of 3–40 mA/cm^2. In experiments, we measured the following parameters: the longitudinal electric field, the EDF as a function of radius, the radial profile of the plasma potential (the radial field profile $E_r(r)$ was calculated from the plasma potential gradient), the densities of negative ions, the plasma temperature at the axis of the positive discharge column, the temperature of the wall of the discharge tube, and the densities of such active particles as $O(^3P)$ atoms and oxygen molecules in the two lowest metastable states $a^1\Delta_g$ and $b^1\Sigma_g^+$. Below, we will describe only the results of measurements of spatial variations in the EDF and electric fields. The radial profiles of the EDF were recorded by a specially designed array of mobile probes with the help of the conventional method of modulation of the probe potential [27]. The second probe in the feedback loop was used to suppress plasma noises and to stabilize the operating point of the device. The plasma potential was determined from the point in the current-voltage characteristic of the probe at which the second derivative of the probe current vanishes. In [27], one can find a more detailed description of our experiments.

The nonlocal nature of the EDF can be revealed experimentally in gas-discharge plasmas at low pressures [3–5, 28], when the spatial profiles of the electron energy distribution function (EEDF) are governed primarily by the potential energy of the electrons in the space charge field. The EDFs measured at two different points should coincide (to within the potential difference between the points, which corresponds to a shift along the energy axis). Figure 2 shows the EEDF obtained experimentally for different values of the parameter pd versus the total electron energy $u = \varepsilon + e\varphi$, where ε is the kinetic energy of the electrons and $e\varphi$ is their potential energy. The EEDF was measured at a discharge current density of 5 mA/cm^2 at three radial positions: $r = 0$ (the discharge axis), 3, and 5 mm. We can see that, at a pressure such that $pd = 0.18$ torr cm, the spatial profiles of the EEDF are well approximated by functions of only the total electron energy; i.e., $F(\varepsilon, r) = F(u(r))$. Up to the energy $\varepsilon \sim 13$ eV, the EEDFs at different radial positions coincide as functions of the total electron energy. The electron energy spectrum at a given radius is governed exclusively by the electrons whose kinetic energy is higher than the potential energy at this point. Hence, the shape of the EEDF is as if its low-energy part were "truncated." For larger values of the parameter pd, the EEDFs measured at different points do not coincide, so that the EEDF can no longer be approximated by a function of only the total energy $u(r)$. Our calculations (see below) show that, even in the range $pd \approx 1$ torr cm at $\Lambda_\varepsilon < d$, the radial electric fields still have a significant impact on the electron energy spectrum. In this sense, the EEDF remains nonlocal.

Figure 3 shows radial profiles of the mean electron energy $\langle\varepsilon\rangle_r = \int \varepsilon^{3/2} F(\varepsilon, r) d\varepsilon$ for $pd = 0.18$, 0.36, 0.6, and 1.2 torr cm at a current density of 5 mA/cm^2. The presence of a fairly long radial interval in which the mean energy is decreasing can be attributed to the specific energy dependence of the EEDF. The slope of the EEDF increases with increasing energy (Fig. 2), which means that the mean energy of the electrons decreases with increasing the distance from the discharge axis. This leads to the effect of "cooling" of the electrons by the radial charge-separation electric field, which is ignored in the local approximation.

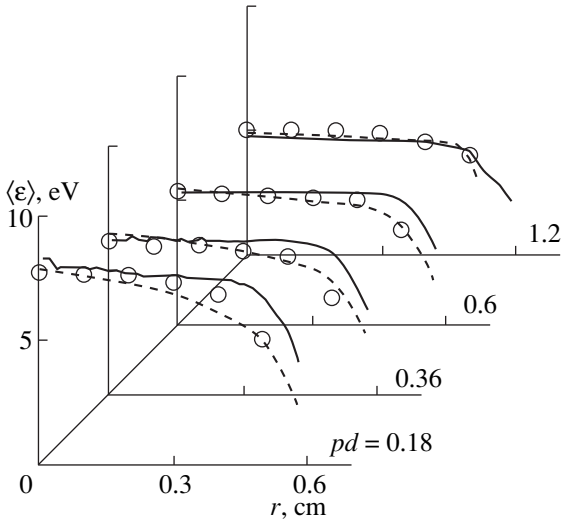

Fig. 3. Radial profiles of the mean electron energy $\langle\varepsilon\rangle$ defined as $\langle\varepsilon\rangle_r = \int \varepsilon^{3/2} F(\varepsilon, r) d\varepsilon$ (where the subscript r indicates the radial position with respect to the discharge axis) for $pd = 0.18$, 0.36, 0.6, and 1.2 torr cm at a fixed discharge current density of 5 mA/cm^2. The circles show the experimental data, and the solid and dashed curves illustrate the results obtained from the discharge models in which the EEDF was calculated by the MC method and in the TTA, respectively. The longitudinal field E_z was taken from the experiment and was assumed to be fixed.

3. DISCUSSION

In the TTA, the electron velocity distribution function $F(\mathbf{v}, \mathbf{r}, t)$ is represented as

$$F(\mathbf{v}, \mathbf{r}, t) = F_0(v, \mathbf{r}, t) + F_1(v, \mathbf{r}, t)\cos\theta, \qquad (2)$$

where $F_0(v, \mathbf{r}, t)$ and $F_1(v, \mathbf{r}, t)$ are the symmetric and antisymmetric parts of the distribution function such that $F_1 \ll F_0$, v is the absolute value of the velocity vector, and θ is the angle between the electric field and the velocity vector. Substituting expression (2) into Eq. (1) yields the following equation for the symmetric part $F_0(\varepsilon, r, t)$ of the distribution function in cylindrical geometry [29, 30]:

$$\frac{\partial}{\partial t}(F_0\sqrt{\varepsilon}) = \frac{\partial}{\partial\varepsilon}\left(D_\varepsilon\frac{\partial}{\partial\varepsilon}F_0\right)N + \frac{1}{r}\frac{\partial}{\partial\varepsilon}\left(rD_{r\varepsilon}\frac{\partial}{\partial\varepsilon}F_0\right) + \frac{1}{r}\frac{\partial}{\partial r}\left(rD_r\frac{\partial}{\partial r}F_0\right) + Q. \qquad (3)$$

Here, ε is the electron kinetic energy and the coefficients D_r, D_ε, and $D_{r\varepsilon}$ have the form

$$D_r = \sqrt{\frac{2}{m}}\left(\frac{\varepsilon}{3N\sigma(\varepsilon)}\right),$$

$$D_\varepsilon = \sqrt{\frac{2}{m}}\frac{\varepsilon}{3\sigma(\varepsilon)}\left[\left(\frac{eE_r(r)}{N}\right)^2 + \left(\frac{eE_z}{N}\right)^2\right], \qquad (4)$$

$$D_{r\varepsilon} = \sqrt{\frac{2}{m}}\left(\frac{\varepsilon}{3\sigma(\varepsilon)}\frac{eE_r(r)}{N}\right),$$

where E_r and E_z are the radial and longitudinal components of the electric field in a plasma, $\sigma(\varepsilon)$ is the transport scattering cross section, and N is the neutral density. In writing (3) and (4), we assumed that the plasma column is homogeneous along the z-axis. In numerical modeling, the symmetric part $F_0(\varepsilon, r, t)$ of the EDF for a steady discharge was calculated using the relaxation method, i.e., by integrating Eq. (3) in time. Following [30], we chose the boundary conditions in such a way

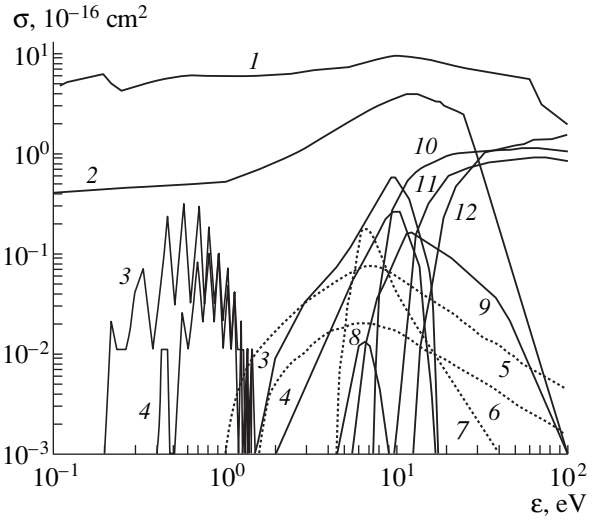

Fig. 4. The set of cross sections for electron scattering by O_2 molecules that was used to calculate the EEDF: (*1*) elastic scattering cross section; (*2*) integral cross section for the excitation of rotational states; (*3*) cross section for the excitation of the first vibrational level of the ground state; (*4*) cross section for the excitation of the second vibrational level of the ground state; (*5*) cross section for the excitation of the $a^1\Delta_g$ electron state; (*6*) cross section for the excitation of the $b^1\Sigma_g^+$ electron state; (*7*) integral cross section for the excitation of the electron states $A^3\Sigma_u^+$, $c^1\Sigma_u^-$, and $A'^3\Delta_u$; (*8*) dissociative attachment cross section; (*9*) dissociative cross section with a threshold of 5.58 eV; (*10*) dissociative cross section with a threshold of 7.34 eV; (*11*) dissociative cross section with a threshold of 9.74 eV; and (*12*) ionization cross section.

that the electrons were not reflected from the tube wall and escaped freely from the plasma volume.

In MC simulations, the equation of electron motion in the prescribed field $\mathbf{E} = \mathbf{E}_z + \mathbf{E}_r$,

$$m_e \frac{d\mathbf{v}}{dt} = e\mathbf{E} \qquad (5)$$

was solved by a finite-difference scheme of second-order accuracy. At each time step, we modeled a statistical process that might involve electrons with the specified energy. The time step was determined from the requirement for the equation of motion (5) to be solved with the desired accuracy and from the condition that the total probability for all of the processes to occur at each time step be small compared to unity.

Recall that, in a discharge plasma, the radial electric field acts to cool the electrons and to equalize the effective electron and ion diffusion coefficients. Consequently, in simulations, it is extremely important to know the wall potential U_W, which governs the fraction of electrons that can overcome the ambipolar potential barrier and leave the plasma (the escape of electrons toward the wall is the main channel of electron losses). Unfortunately, in our experiments, we failed to determine the plasma potential drop near the wall. For this reason, in simulations, we adjusted the wall potential so that the computed EDF was steady. In simulations with higher or lower values of U_W, the plasma electron density increased or decreased exponentially in time. In this connection, the value of the wall potential U_W used to calculate the EEDF in the TTA differed from that used in MC simulations.

In order to make a comparison between the results obtained in the TTA and MC simulations correct, we used the same set of cross sections for electron scattering by O_2 molecules (see Fig. 4). Using the same set is justified because, in our experiments, the total scattering cross section is only slightly anisotropic up to high electron energies of about 20–30 eV.

In Figs. 5a and 5b, which were obtained for pd = 0.18 and 1.2 torr cm, respectively, and illustrate the dependence of the electron distribution function on the electron kinetic energy ε, we compare the local EEDF obtained by solving the spatially homogeneous Boltzmann equation with both the EEDF measured experimentally and the EEDFs calculated in the TTA and by the MC method. Since, in Fig. 5b, $\Lambda_\varepsilon < d$, we can naturally expect that the EEDF will be close to the local distribution function over the entire plasma cylinder except for a narrow wall layer. In fact, Fig. 5b shows that the EEDFs obtained experimentally and computed for a spatially nonuniform field are close to the local EEDF everywhere except for a wall layer with a thickness of about Λ_ε. As can be seen from Fig. 5a, the lower the pressure, the more important the effects of the nonlocal nature of the electron distribution: the experimental and calculated EEDFs deviate from the local EEDF over the entire plasma column. In the high-energy range, the nonlocal nature of the electron energy spectrum obtained in the TTA is seen to be more pronounced than in the case of EEDFs measured experimentally and calculated by the MC method. This discrepancy is associated with the boundary conditions imposed in the TTA. Although the TTA can be used to describe the electron flux in coordinate space, it fails to hold in a fairly narrow wall layer (with a thickness of about the electron mean free path). Since Eq. (3) does not describe the real electron motion in velocity space, the electron flux to the wall turns out to be overestimated. Such an electron flux can be corrected by introducing a nonzero reflection coefficient of the plasma surface for electrons. In other words, in the total electron flux, we must take into account only the electrons whose velocity vector lies inside the loss cone $\delta\Omega$. To do this, we incorporate the loss cone into the boundary condition for Eq. (3) through a relationship analogous to that presented in [5, 14]:

$$\delta\Omega = 2\pi\left(1 - \sqrt{\frac{e(U(r) - U_W)}{\varepsilon(r)}}\right)\Bigg|_{r=R}. \qquad (6)$$

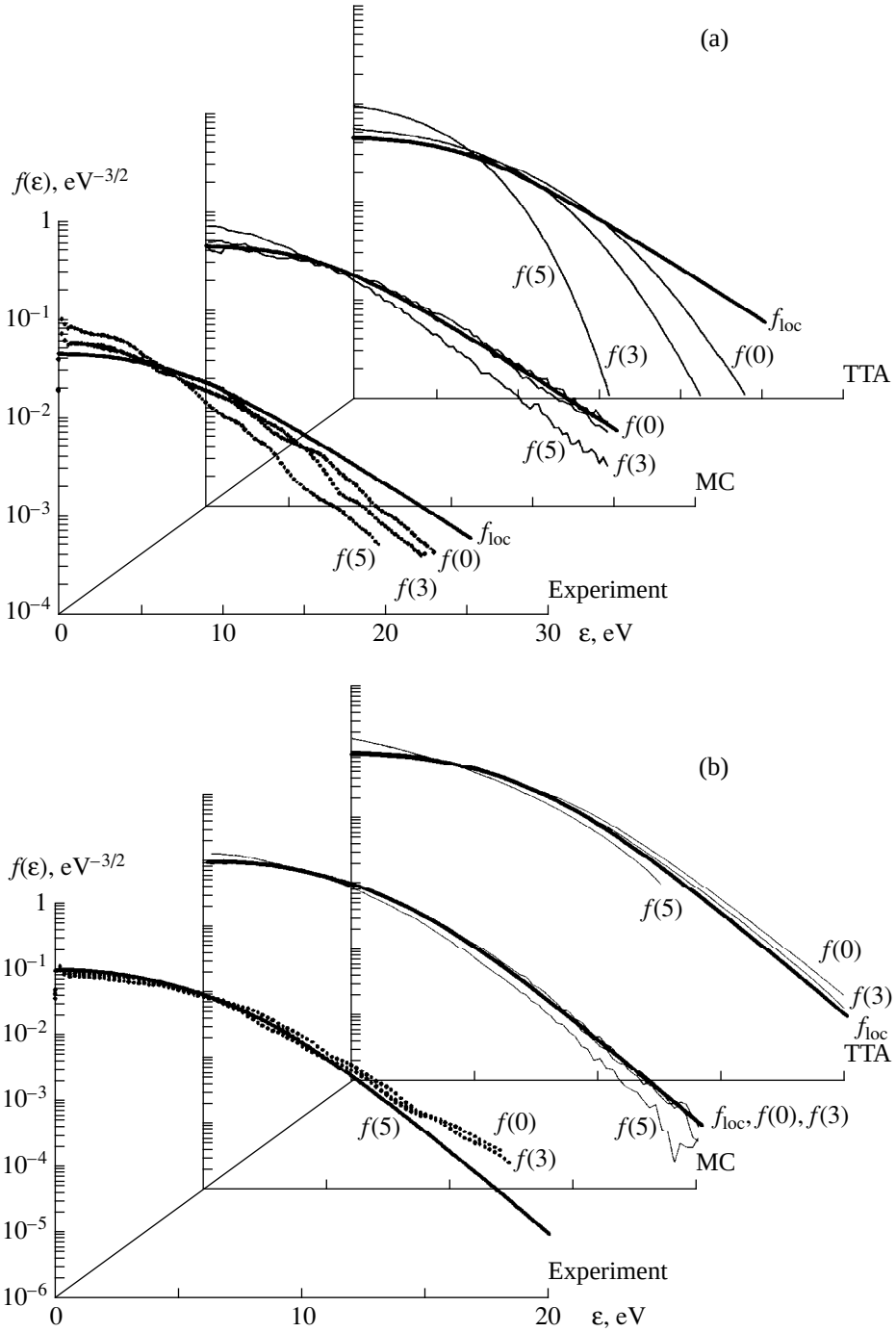

Fig. 5. Comparison of the local EEDF calculated as a function of the kinetic energy by solving the coordinate-independent Boltzmann equation with both the experimentally measured EEDF and the EEDFs computed by the MC method and in the TTA. The profiles $f(0)$, $f(3)$, and $f(5)$ refer to the radial positions r = 0, 3, and 5 mm. The heavy solid curve shows the local EEDF f_{loc}. The calculations were carried out for pd = (a) 0.18 and (b) 1.2 torr cm.

Condition (6) differs from the corresponding expression for $\delta\Omega$ in [5, 14] in that it describes the reflection of electrons from the plasma surface with the probability $\frac{1}{2}\sqrt{\frac{e(U(R)-U_W)}{\varepsilon(R)}}$ rather than the loss cone in the plasma volume. Kortshagen *et al.* [14] showed that the electron losses can be described as an electron flux to the wall through the loss cone only when $\Lambda_\varepsilon \gg L$. Condition (6) assumes that there is a jump $U_W - U(R)$ in the plasma potential near the wall. Physically, this corresponds to a plasma-wall layer whose thickness is of about the electron mean free path and in which the

space charge is unneutralized. In this case, the wall potential U_W should again be found self-consistently from the condition that the EEDF be steady. According to (6), taking into account electron reflection from the plasma surface makes it possible to achieve good agreement between the radial profiles of the EEDF calculated in the TTA and by the MC method, except, of course, for a narrow wall region where the EDF is still highly anisotropic. That the values of U_W obtained by the two calculation methods approximately coincide is, in our opinion, additional evidence of the applicability of the TTA to the problem under discussion.

We emphasize that the above discrepancy between the EEDF obtained in the TTA without allowance for electron reflection from the plasma surface and the EEDF calculated by the MC method weakly affects the ionization rate and other global kinetic coefficients of the discharge plasma. In fact, the EEDFs computed on the basis of the above approaches differ strongly only in the energy range $\varepsilon \geq 20$ eV, which is far above the thresholds for all inelastic processes, including the threshold 12.07 eV for ionization of O_2 molecules. That is why simulations of the discharge plasma kinetics carried out by different approaches for determining the spatially inhomogeneous EEDF yield essentially the same results. This is illustrated in Fig. 3, which presents, in addition to the experimentally measured profiles of $\langle\varepsilon\rangle$, the radial profiles of the mean electron energy calculated using a unified discharge model in which the EEDF was computed in different ways at a fixed axial electric field E_z. Figure 3 shows good agreement between the profiles corresponding to the EEDFs obtained in the TTA and by the MC method. The radius-averaged ionization rates $\overline{\langle\sigma v\rangle_{\text{ion}}} = \overline{\langle\sigma v\rangle_{\text{ion}} n_e}/\overline{n_e}$ obtained from the EEDFs computed in these ways are nearly the same over the entire range of the parameter pd (here, the angular brackets denote averaging over the EEDF and the overbar stands for averaging over radius). A slight discrepancy in the range $pd < 0.2$ torr cm stems from the physical reasons that we have discussed above. However, a comparison between the mean ionization rates obtained from the nonlocal and local models shows that, even in the range of large values of the parameter pd ($pd > 1$ torr cm), the local model gives a somewhat overestimated rate $\overline{\langle\sigma v\rangle_{\text{ion}}}$. In other words, the electric field obtained from the discharge models in which the EEDF is calculated in the local approximation is lower than the real electric field in a discharge plasma.

To construct a completely self-consistent discharge model that would be valid for the entire range of values of the parameter pd requires a self-consistent solution of the Boltzmann kinetic equation (1) supplemented with the continuity equations for charged particles and Poisson's equation for the electric field. More exact approaches (e.g., the PIC–MC method) make it possible to determine various spatial characteristics of the discharge in a broad parameter range, but they involve a considerable expenditure of computational resources. Our work makes it possible to carry out simulations using an algorithm that is much faster than that based on the PIC–MC method. For dc discharges in pure oxygen, such a simplified approach was developed in our paper [25], which allowed us to investigate the kinetics of negative oxygen ions in detail.

4. CONCLUSION

We have studied the nonlocal nature of the EEDF in a positive column of a glow discharge in a tube filled with pure oxygen. The experimentally measured radial profiles of the EEDF were used to analyze whether the TTA is applicable for determining the EEDF in a discharge with a nonlocal electron energy spectrum. With this purpose, we calculated the EEDF in the specified field $\mathbf{E} = \mathbf{E}_z + \mathbf{E}_r$ with the E_z and E_r components taken from the experiment. The EEDF was computed by solving the coordinate-dependent Boltzmann equation in the TTA and by the MC method for direct integration of the equations for electron motion. A comparison between the experimental and numerical results shows that, even when the electron energy spectrum is highly nonlocal, the TTA makes it possible to calculate the EEDF quite accurately over a broad parameter range, in which case, however, the boundary conditions should reflect the kinetic nature of electron losses at the plasma surface.

ACKNOWLEDGMENTS

This work was supported in part by the Russian Foundation for Basic Research, project nos. 00-15-96554 and 00-02-16508.

REFERENCES

1. L. D. Tsendin, Zh. Éksp. Teor. Fiz. **66**, 1638 (1974) [Sov. Phys. JETP **39**, 805 (1974)].
2. I. B. Bernstein and T. Holstein, Phys. Rev. **94**, 1475 (1954).
3. U. Kortshagen, Phys. Rev. E **49**, 4369 (1994).
4. V. I. Kolobov and V. A. Godyak, IEEE Trans. Plasma Sci. **23**, 503 (1995).
5. U. Kortshagen, I. Pukrovski, and L. D. Tsendin, Phys. Rev. E **51**, 6063 (1995).
6. V. N. Volynets, A. V. Lykyanova, A. T. Rakhimov, *et al.*, J. Phys. D **26**, 647 (1993).
7. V. A. Feoktistov, A. M. Popov, O. B. Popovicheva, *et al.*, IEEE Trans. Plasma Sci. **19**, 163 (1991).
8. P. M. Meijer, W. J. Goedheer, and J. D. P. Passchier, Phys. Rev. A **45**, 1098 (1992).
9. C. Busch and U. Kortshagen, Phys. Rev. E **51**, 280 (1995).
10. L. L. Alves, G. Gousset, and C. M. Ferreira, Phys. Rev. E **55**, 890 (1997).

11. M. Schmidt, D. Uhrlandt, and R. Winkler, IEEE Trans. Plasma Sci. **27**, 1271 (1999).
12. M. J. Kushner, J. Appl. Phys. **54**, 4958 (1983).
13. T. J. Sommerer and M. J. Kushner, J. Appl. Phys. **71**, 1654 (1992).
14. U. Kortshagen, G. J. Parker, and J. E. Lawler, Phys. Rev. E **54**, 6746 (1996).
15. V. V. Ivanov, A. M. Popov, and T. V. Rakhimova, Fiz. Plazmy **21**, 548 (1995) [Plasma Phys. Rep. **21**, 516 (1995)].
16. R. W. Boswell and I. J. Morey, Appl. Phys. Lett. **52**, 21 (1988).
17. C. K. Birdsall, IEEE Trans. Plasma Sci. **19**, 102 (1991).
18. M. Surendra and D. B. Graves, IEEE Trans. Plasma Sci. **19**, 144 (1991).
19. *Electron Kinetics and Applications of Glow Discharges* (Plenum, New York, 1998); NATO ASI Ser., Ser. B **367** (1998).
20. A. Bogaerts and R. Gijbels, IEEE Trans. Plasma Sci. **27**, 1406 (1999).
21. U. Kortshagen and B. G. Heil, IEEE Trans. Plasma Sci. **27**, 1297 (1999).
22. V. A. Feoktistov, V. V. Ivanov, A. M. Popov, *et al.*, J. Phys. D **30**, 423 (1997).
23. G. Gousset, C. M. Ferreira, M. Pinheiro, *et al.*, J. Phys. D **24**, 290 (1991).
24. V. A. Feoktistov, D. V. Lopaev, K. S. Klopovsky, *et al.*, J. Nucl. Mater. **200**, 309 (1993).
25. V. V. Ivanov, K. S. Klopovskiy, D. V. Lopaev, *et al.*, IEEE Trans. Plasma Sci. **27**, 1279 (1999).
26. E. Stoffels, W. W. Stoffels, D. Vender, *et al.*, Phys. Rev. E **51**, 2425 (1995).
27. V. V. Ivanov, K. S. Klopovskiĭ, D. V. Lopaev, *et al.*, Pis'ma Zh. Éksp. Teor. Fiz. **63**, 511 (1996) [JETP Lett. **63**, 537 (1996)].
28. V. A. Godyak, R. B. Piejak, and B. M. Alexandrovich, Plasma Sources Sci. Technol. **1**, 36 (1992).
29. V. L. Ginzburg and A. V. Gurevich, Usp. Fiz. Nauk **60**, 201 (1960) [Sov. Phys. Usp. **3**, 115 (1960)].
30. A. M. Popov, A. T. Rakhimov, and T. V. Rakhimova, Fiz. Plazmy **19**, 1241 (1993) [Plasma Phys. Rep. **19**, 651 (1993)].

Translated by O. Khadin

Plasma Physics Reports, Vol. 26, No. 11, 2000, pp. 980–990. Translated from Fizika Plazmy, Vol. 26, No. 11, 2000, pp. 1046–1056.

LOW-TEMPERATURE PLASMA

Nonlocal Nature of the Electron Energy Spectrum in a Glow-Discharge in Pure O_2: II. Actinometry of $O(^3P)$ Atoms in a Plasma at Low Gas Pressures

V. V. Ivanov, K. S. Klopovskiĭ, D. V. Lopaev, A. T. Rakhimov, and T. V. Rakhimova

Research Institute of Nuclear Physics, Moscow State University, Vorob'evy gory, Moscow, 119899 Russia

Received April 3, 2000

Abstract—Results are presented from measurements of the density of oxygen atoms in the positive column of a dc discharge in pure oxygen by the actinometric technique using Ar atoms. Based on the excitation rate constants calculated using two different approaches (namely, the two-term approximation and the Monte Carlo method) to solving the Boltzmann equation for a spatially inhomogeneous electron distribution function, the applicability of the actinometric technique is analyzed. The effects of the discharge kinetics and the nonlocal character of the electron energy spectrum on the accuracy of actinometric measurements are studied. It is shown that the results of measurements depend only slightly on the accuracy with which the electron energy distribution function is described. Over a wide range of the reduced electric field $E/N \approx 40$–250 Td, the oxygen atom density calculated using the spatially homogeneous distribution function differs by several percent from that calculated accurately, taking into account the nonlocal character of the electron energy spectrum. It is shown that using the actinometric technique to measure the absolute concentration of oxygen atoms in a plasma requires a detailed description of the discharge plasmochemical kinetics, including a thorough analysis of all possible processes (particularly, surface heterogeneous reactions) that determine the density of active particles at low pressures. At the same time, the use of the actinometric technique for monitoring the behavior of the density of oxygen atoms in a plasma is justified over a wide range of reduced electric fields up to ~200 Td when the $O(3p^3P$–$3p^3S)$ transition ($\lambda = 844.6$ nm) is used and the degree of dissociation is $[O]/[O_2] > 0.02$. © *2000 MAIK "Nauka/Interperiodica".*

1. INTRODUCTION

At present, low-temperature plasmas of molecular gases are attracting wide scientific interest. This is primarily due to the great importance of active particles (first of all, atoms and radicals) formed via the electron-impact dissociation of molecules in a gas-discharge plasma of molecular gases. In fact, the role that plasma technology plays in modern microelectronics, engineering, ecology, medicine, etc., is mostly determined by the possibility of efficiently producing and using active particles

In many cases, the concentrations of atoms and radicals are so high that they not only significantly affect particular elementary processes in a plasma, but also govern the electrodynamics and macroscopic parameters of a discharge as a whole. This is most pronounced in plasmas of electronegative gases, in which, due to the efficient production of negative ions, their density can significantly exceed the electron density [1–5]. Under conditions typical of various applications of such plasmas (e.g., oxygen and hydrogen gas-discharge plasmas [5–7]), the kinetics of negative ions is governed largely by the atomic kinetics. Therefore, knowledge of the absolute concentrations of oxygen and hydrogen atoms is of great importance for understanding the physics of discharges in O_2 and H_2.

Currently, the most powerful and relatively universal method for detecting atoms and small molecular radicals in the ground and long-lived excited states is laser-induced fluorescence (LIF), including its various modifications, e.g., the method of two-photon LIF and the detection of nonspontaneous (laser-stimulated) emission [8–12]. The advantages of this method are obvious: it does not disturb the plasma and has high space and time resolution and high sensitivity. However, the implementation of this diagnostics requires not only a rather complicated and expensive laser technique necessary to generate high-power narrow-band radiation in the far UV region, but also an accurate (and frequently very complicated) calibration of the LIF signals referring to the density of atoms in the ground state (in other words, the adaptation of LIF diagnostics to the discharge plasma). For this reason, the multiphoton LIF diagnostics is used only at major scientific centers and, most frequently, only when the problem itself requires it. However, the necessity to know the absolute concentrations of atoms in molecular-gas plasmas is of primary importance for a wide class of problems, especially, for those related to various applications. For this reason, simple methods to diagnose atoms and radicals at the ground state are of considerable interest.

In our opinion, the most advantageous among these methods is the actinometric technique. It is most often

1063-780X/00/2611-0980$20.00

used to detect atoms in a chemically active plasma when other methods are difficult to use. The actinometric technique has already been widely used to measure the densities of various radicals in discharge plasmas [13–16] (in particular, O atoms [17–22]). However, we note that the accuracy of the actinometric technique and thus its potentiality are completely determined by the extent to which the discharge model used is adequate to the actual situation in the plasma. Let us briefly explain this.

According to the concept of the actinometry technique, the electronic states X_i^* and Z_l^* of a radical and an actinometer atom (usually, the actinometer is an atom of a noble gas, most frequently, argon) in a discharge are chosen such that they are mainly populated via electron impact, whereas deactivation occurs via radiative decay [processes (1) and (2), respectively]:

$$e + X \xrightarrow{k_e^{X_i}} e + X_i^*, \tag{1a}$$

$$e + Z \xrightarrow{k_e^{Z_l}} e + Z_l^*, \tag{1b}$$

$$X_i^* \xrightarrow{A_{ij}^X} X_j^* + h\nu_{ij}, \tag{2a}$$

$$Z_l^* \xrightarrow{A_{lm}^X} Z_m^* + h\nu_{lm}. \tag{2b}$$

Here, $k_e^{X_i}$ and $k_e^{Z_l}$ are the electron-impact ionization rate constants of the X_i^* and Z_l^* excited states and A_{ij}^X and A_{lm}^Z are the Einstein coefficients for spontaneous radiative decay of the X_i^* and Z_l^* states through the $X^*(i \longrightarrow j)$ and $Z^*(l \longrightarrow m)$ channels, respectively. However, there may be other channels for populating and quenching the X_i^* and Z_l^* states. Among them, the main processes are nonradiative quenching of the excited states by plasma particles (primarily, neutrals) and dissociative excitation of the X_i^* state during the scattering of electrons by XY molecules [processes (3) and (4), respectively]:

$$X_i^* + M_q \xrightarrow{k_q^{X_i}} X + M_q, \tag{3a}$$

$$Z_l^* + M_q \xrightarrow{k_q^{Z_l}} Z + M_q, \tag{3b}$$

$$e + XY \xrightarrow{k_{de}^{X_i}} X_i^* + Y + e, \tag{4}$$

where $k_q^{X_i}$ and $k_q^{Z_l}$ are the quenching rate constants of the X_i^* and Z_l^* states by M particles and $k_{de}^{X_i}$ is the constant of X_i^* production during the dissociative excitation of XY molecules. Hence, in a steady-state discharge, the emission intensity of X^* excited states due to the $(i \longrightarrow j)$ transition can be written in the form [22]

$$I_{ij} = h\nu_{ij}A_{ij}^X n_e \frac{k_e^{X_i}[X] + k_{de}^{X_i}[XY]}{\sum_j A_{ij}^X + \sum_q k_q^{X_i}[M_q]}, \tag{5}$$

where n_e is the electron density and $\sum_j$ and $\sum_q$ are the sums over the processes of radiative and nonradiative decay of the X_i^* state. A similar expression can also be written for the emission intensity of the actinometer atom in a discharge:

$$I_{lm} = h\nu_{lm}A_{lm}^Z n_e \frac{k_e^{Z_l}[Z]}{\sum_m A_{lm}^Z + \sum_q k_q^{Z_l}[M_q]}. \tag{6}$$

Hence, from relations (5) and (6), it follows that

$$[X] = \frac{I_{ij}}{I_{lm}} \frac{C_X^Z[Z]}{1 + \dfrac{k_{de}^{X_i}[XY]}{k_e^{X_i}[X]}}, \tag{7}$$

$$C_X^Z = \frac{h\nu_{ij}A_{ij}^X}{h\nu_{lm}A_{lm}^Z} \frac{k_e^{X_i}}{k_e^{Z_l}} \frac{\sum_m A_{lm}^Z + \sum_q k_q^{Z_l}[M_q]}{\sum_j A_{ij}^X + \sum_q k_q^{X_i}[M_q]}. \tag{8}$$

The rate constants $k_e^{X_i}$, $k_{de}^{X_i}$, and $k_e^{Z_l}$ are determined by the cross sections σ_e for the corresponding electron-scattering processes and the electron energy distribution function (EEDF) $f(\varepsilon)$ in a plasma:

$$k_e = \left(\frac{2e}{m_e}\right)^{1/2} \int_{\varepsilon^*}^{\infty} v(\varepsilon)\sigma_e(\varepsilon) f(\varepsilon) d\varepsilon,$$
$$\int_0^{\infty} f(\varepsilon)\varepsilon^{1/2} d\varepsilon = 1, \tag{9}$$

where ε^* is the threshold energy of the process; $v(\varepsilon)$ is the velocity of electrons with energy ε; and e and m_e are the electron mass and charge, respectively. It is evident from formula (7) that the actinometric method is applicable (i.e., the radical density can be derived from the ratio of two line intensities and a known value of the actinometer concentration) if, under certain experimental conditions, we have $C_X^Z \approx$ const and the inequality $k_{de}^{X_i}/k_e^{X_i} \ll [X]/[XY]$ holds. As applied to actual experiments, the verification of the validity of these relationships means that the values of all the coefficients entering formula (7) should be accurately determined. However, in this case, it is necessary to know both the

excitation cross sections of the excited states and their quenching rate constants and to rather accurately describe the EEDF in a plasma because the inequality $\varepsilon^* \gg \varepsilon_m$ (where ε_m is the mean electron energy) almost always holds. Hence, in order to use the actinometric technique to not only monitor the behavior of atoms and radicals in a plasma, but also to accurately measure their densities, it is necessary that all the quantities contributing to the actinometer signal be measured with a high accuracy.

The applicability of the actinometric technique in particular to the detection of O atoms using argon atoms was verified in [17–22]. However, the accuracy of the method was determined in an indirect way, namely, by detecting atoms in the ground state by another (more direct) method (e.g., by the two-photon LIF or resonant VUV absorption). The factors governing the applicability of the actinometric method were not analyzed in detail. Among these factors, the electron-excitation rate constants are the most important because the emitting states have high excitation thresholds. Therefore, such an analysis must include the following:

(i) Determination of the electronic excitation cross sections near the threshold, where these cross sections are usually known with an insufficient accuracy.

(ii) Determination of the EEDF, which means either accurate spatial measurements of the EEDF or a sufficiently accurate calculation of the EEDF based on the model including all of the basic processes governing the EEDF formation. Depending on the discharge conditions, these may be either effects related to the nonlocal nature of the electron energy spectrum [23, 24] or the processes of ion and chemical kinetics [5, 6, 25]. The influence of the latter can be very strong; for example, in an O_2 plasma at pressures of a fraction of torr to several torr, due to the high density of metastable particles, the field in the plasma and, thereby, the EEDF and electron density [5, 6] are governed by electron detachment from negative ions.

(iii) Comparison of experimental results with calculations over a wide range of the discharge conditions.

The problems mentioned in the first item (i.e., analyzing and testing the electron-impact cross sections for radiative transitions of oxygen atoms, including the dissociative excitation of O_2 and argon molecules) were studied in [22]. Our study is devoted to items (ii) and (iii). In this paper, we present the results from actinometric measurements of the density of O atoms using Ar atoms in a positive column of a dc discharge in pure oxygen. The method and results obtained are analyzed based on a self-consistent model of a discharge using different approaches to determining the EEDF: (a) the two-term approximation (TTA), involving the solution of the kinetic Boltzmann equation for the spatially inhomogeneous EEDF, and (b) the particle-in-cell method combined with the Monte Carlo technique (PIC–MC technique). The effect of nonlocal electron kinetics on the accuracy of the actinometric technique is analyzed for the first time. In addition, the influence of the dissociative excitation of O* on the results of measurements of the O atom density by the actinometric technique is also examined.

2. EXPERIMENT

A dc discharge in pure O_2 was ignited in a 12-mm-diameter molybdenum glass tube. The distance between two profiled molybdenum electrodes was 490 mm. The experiments were carried out at pressures of 0.15–6 torr and gas discharge currents of 3–40 mA/cm^2. In the experiment, the following discharge characteristics were determined:

(i) The radial profiles of the plasma potential (and, correspondingly, the electric field) in the positive column of a discharge were measured using three movable electric probes [23].

(ii) The radial profiles of the EEDF were measured using the second harmonic technique and a newly elaborated system of movable probes with optical reception–transmission channels and a feedback system for active suppression of plasma noise [23].

(iii) The spatial profiles of the negative-ion density were measured using the laser photodetachment technique [5].

(iv) The molecular oxygen density in two lower ($a^1\Delta_g$ and $b^1\Sigma_g^+$) excited states was measured using IR emission spectroscopy at 1268- and 762-nm wavelengths, respectively.

(v) The temperature of the discharge tube wall was determined using chromel–alumel thermocouples.

(vi) The gas temperature near the axis of the positive discharge column was determined using the spectroscopy of the vibrationally resolved ^QP-branch of the band $O_2(b^1\Sigma_g^+,\ v = 0) \longrightarrow O_2(X^3\Sigma_g^-,\ v = 0)$ λ = 762 nm).

(vii) The density of O atoms in the ground state was measured with the help of the actinometric technique using argon atoms and the optical transitions $O(3p^3P–3p^3S)$ (λ = 844.6 nm) and $Ar(2p_9 – 1s_5)$ (λ = 811.5 nm).

(viii) The recombination rate of O atoms on the tube wall under discharge conditions was measured using the actinometric technique for recording the decay dynamics of the nonequilibrium oxygen atom density, which was modulated by slightly modulating the discharge current [26].

In this paper, we only present the results of measurements referring to items (vii) and partly (viii), although it is evident that all of the above measurements are related to each other: when analyzing the results of each particular experiment, we must invoke the data from at least several other experiments. The block diagram of the experiment is shown in Fig. 1.

In the experiment, we used an O_2 : Ar = 98 : 2 mixture. The radiation emitted by electronically excited oxygen and argon atoms from the axial region of the discharge tube (with a diameter of about 0.5–0.6 of the tube diameter) was separated using a set of diaphragms. Then, the radiation was focused on the slit of a monochromator and was detected by either a photomultiplier with a GaAs photocathode or a 512-channel silicon CCD array. In the latter case, an OMA system based on an IBM PC was used. In the scheme using a photomultiplier, the discharge emission was modulated with a mechanical shutter and the radiation in the 750- to 850-nm spectral region was recorded by a synchronous detector (a PAR-5209 lock-in amplifier interface-connected to the computer). Simultaneously, the synchronous detector (with the help of a program-controlled channel of a 16-bit ADC) recorded the electric probe signal corresponding to the electric field strength in the plasma.

To determine the loss rate of O atoms at the tube wall during the discharge, the following method was used. It is known that, for weak perturbations of the discharge parameters, the time required for the steady-state EEDF to be established in a gas-discharge plasma at a pressure of ~1 torr and $E/N > 10$ Td is shorter than 1 μs. Experiments showed (see, e.g., [27, 28]) that the time required for the electron density in O_2 plasmas to reach a steady-state value is also short (on the order of several tens of microseconds). Under the same conditions, the characteristic time required for the density of oxygen atoms to reach a steady-state value is longer than 1 ms because this time is determined by the loss of oxygen atoms at the discharge tube wall (for a tube diameter of 10–20 mm) [20, 29, 30]. This fact was used to determine the rate of heterogeneous loss of O atoms on glass under conditions of a discharge in pure O_2. To do this, the discharge current was modulated by varying the ballast resistance within several percent of its nominal value. In this case, variations in the electric field in the positive column of the discharge did not exceed several percent. The current was modulated with a frequency of several tens of Hz; in this case, the relative increase in the steady-state concentration of oxygen atoms (Δ[O]) in the higher current phase was no more than 2–3%. Therefore, one steady-state concentration of oxygen atoms [O] changed to another: [O] + Δ[O]. In contrast, when going to the lower current phase, the steady-state concentration of oxygen atoms [O] + Δ[O] changed to [O]. The characteristic time of these transitions corresponded to the time during which the steady-state oxygen atom concentration in the discharge was reached; in turn, this time was determined by the recombination rate of O atoms on the tube wall. The experiments showed that, nearly 0.1 ms after the additional current was switched on or off, it was possible to observe an increase or decrease in the oxygen atom concentration by the value Δ[O] using the actinometric technique. In other words, the discharge electrons, whose density rapidly reached a steady-state value after switching the additional discharge current, "highlighted" the process of establishing the steady-state atomic oxygen concentration. In this experiment, the signals from the photomultiplier anode were fed to a preamplifier and then to a digital oscillograph synchronized with the modulation pulse. The oscillograph was interface-connected to an IBM PC for data acquisition and processing.

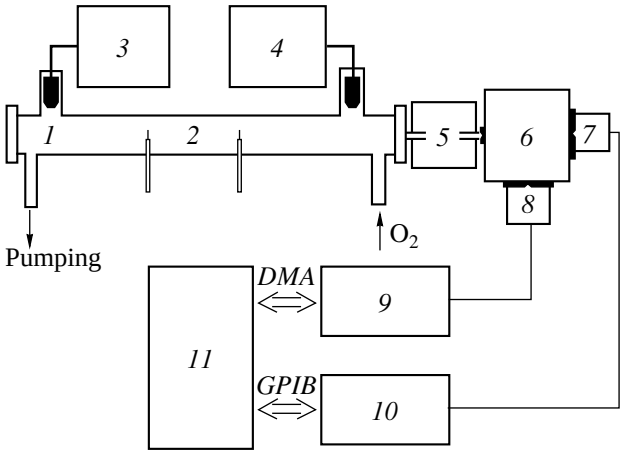

Fig. 1. Schematic of the experiment: (*1*) discharge tube, (*2*) movable probes, (*3*) high-voltage power supply, (*4*) discharge-current modulation circuit, (*5*) optical system for spatial separation of emission, (*6*) monochromator, (*7*) photomultiplier, (*8*) silicon CCD array, (*9*) CCD controller plate, (*10*) synchronous detector or digital oscillograph, and (*11*) computer.

3. MODEL. CALCULATION OF THE ELECTRONIC EXCITATION RATES, INFLUENCE OF THE NONLOCAL CHARACTER OF THE ELECTRON SPECTRUM

According to the scheme (1)–(4), the following basic processes of excitation and deactivation of $O(3p^3P)$ and $Ar(2p_9)$ atoms are possible:

$$e + \mathrm{Ar}(1p_0) \xrightarrow{k_e^{2p_9}} e + \mathrm{Ar}(2p_9), \tag{10}$$

$$e + \mathrm{O}(2p^4\,{}^3P) \xrightarrow{k_e^{3P}} e + \mathrm{O}(3p\,{}^3P), \tag{11}$$

$$\mathrm{Ar}(2p_9) \xrightarrow{A_{811}^{2p_9}} \mathrm{Ar}(1s_5) + h\nu_{811}, \tag{12}$$

$$\mathrm{O}(3p\,{}^3P) \xrightarrow{A_{844}^{3P}} \mathrm{O}(3s^3S) + h\nu_{844}, \tag{13}$$

$$e + \mathrm{O}_2 \xrightarrow{k_{de}^{3P}} e + \mathrm{O} + \mathrm{O}(3p^3P), \tag{14}$$

$$\mathrm{O}(3p^3P) + \mathrm{O}_2 \xrightarrow{k_q^{3P}} \mathrm{O} + \mathrm{O}_2, \tag{15}$$

$$\mathrm{Ar}(2p_9) + \mathrm{O}_2 \xrightarrow{k_q^{1p_9}} \mathrm{Ar} + \mathrm{O}_2. \tag{16}$$

According to (5)–(8), the degree of dissociation of oxygen in a plasma can be represented as

$$\frac{[O]}{[O_2]} = D_{^3P}^{2p_9}\frac{I_{844}}{I_{811}} - \frac{k_{de}^{^3P}}{k_e^{^3P}}, \quad (17)$$

where

$$D_{^3P}^{2p_9} = \frac{[Ar]}{[O_2]}\frac{h\nu_{811}A_{811}^{2p_9}}{h\nu_{844}A_{844}^{^3P}}\frac{k_e^{2p_9}}{k_e^{^3P}}\frac{\sum_m A_m^{^3P} + \sum_q k_q^{^3P}[O_2]}{\sum_j A_j^{2p_9} + \sum_q k_q^{2p_9}[O_2]}. \quad (18)$$

A detailed analysis of the processes of radiative decay (12) and (13) and collisional quenching (15) and (16) was performed in [21, 22], where it was found that $A_{844}^{^3P} = \sum_m A_m^{^3P} = 2.98\times10^7\ s^{-1}$, $A_{811}^{2p_9} \approx \sum_j A_j^{2p_9} = 4.6\times10^7\ s^{-1}$ (the $O(3p^3P - 3p^3S)$ and $Ar(2p_9 - 1s_5)$ transitions are the main processes of radiative decay of the corresponding excited atomic levels), and $k_q^{^3P} = 8\times10^{-10}\sqrt{T/300}$ cm^3/s. We note that accurate data on the rate constant for process (16) are not available; for this reason, we used the value $k_q^{2p_9} \approx 2.2\times10^{-10}\sqrt{T/300}$ cm^3/s for the total rate constant of quenching the $2p_9$ level by argon [23] because, for most of the $4p$ levels of Ar, the cross sections for quenching by argon and oxygen have nearly the same values. The chosen value agrees with the data from [22] on the rate constant for quenching the $Ar(2p_1)$ level by O_2 molecules. The influence of process (16) becomes significant at pressures above ~3 torr; therefore, inaccuracy in determining its rate constant can lead to a certain inaccuracy of actinometric measurements.

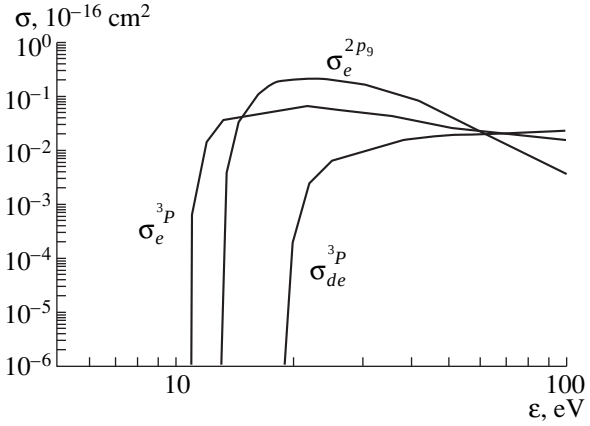

Fig. 2. Electron-impact excitation cross sections for $O(3p^3P)$ and $Ar(2p_9)$ atoms as functions of the electron energy: $\sigma_e^{^3P}$ is the direct-impact excitation cross section for $O(3p\ ^3P)$, $\sigma_{de}^{^3P}$ is the dissociative excitation cross section for $O(3p\ ^3P)$, and $\sigma_e^{2p_9}$ is the excitation cross section for $Ar(2p_9)$.

As for the processes of electronic excitation (10), (11), and (14), the calculation of the corresponding rate constants $k_e^{^3P}$, $k_e^{2p_9}$, and $k_{de}^{^3P}$ requires not only a detailed consideration of the cross sections of these electronic processes, but also a thorough analysis of all the processes involved in the formation of the EEDF in a plasma (including the calculation of the full set of scattering cross sections for electrons). The latter, in turn, includes an analysis of the correctness of the approach used to calculate the EEDF for the given experimental conditions. Therefore, the choice of the electronic-excitation cross sections and methods for calculating the EEDF is of key importance for the problem of the applicability limits and accuracy of the actinometric technique.

The cross sections that are necessary to calculate the rate constants must be chosen based on independent measurements of the atomic oxygen concentration. Since we did not conduct such measurements, we used a set of cross sections for the direct and dissociative excitation of $O(3p^3P)$ atoms by electron impact from [21, 22]. These cross sections were tested by measuring the density of O atoms in a dc discharge in pure O_2 with the help of resonant UV absorption spectroscopy. When choosing the excitation cross sections for the $2p_9$ level, we used the results of an analysis of electron-impact excitation cross sections for heavy noble gases [24]. The chosen energy profiles of the excitation cross section for $Ar(2p_9)$ [31] also allowed for cascade excitation processes. The obtained cross section corresponds to a similar cross section from the set [25] also used in [22] to calculate the excitation rate constant for the transition $Ar(2p_1 - 1s_2)$ (λ = 750.3 nm). The energy profiles of the excitation cross sections used to calculate the corresponding electronic states of oxygen and argon atoms are shown in Fig. 2.

The following approaches were used to analyze how the methods for determining the EEDF affect the accuracy of actinometry. The first approach (which is commonly used) is to use a discharge model in the local approximation; i.e., the EEDF is calculated by solving the coordinate-independent Boltzmann equation. The second approach consists in using a nonlocal model of a discharge. In this case, two methods were used to determine the spatially inhomogeneous EEDF:

(i) The EEDF is determined by solving the coordinate-dependent kinetic equation for the radial electric field using the two-term approximation for the EEDF (see Part I of this paper dedicated to the nonlocal character of the EEDF) [5, 26, 27].

(ii) The EEDF is calculated by the PIC–MC technique, which allows one to accurately take into account the spatial inhomogeneity of the EEDF [4, 5, 28]. In all cases, we used the same set of electron-scattering cross sections for O_2 (see Fig. 4 in Part I of this paper). This set of cross sections was tested in many experiments. The basic processes determining the electrodynamics of a glow discharge in pure O_2 are listed in [5].

The EEDF was calculated self-consistently at pressures of 0.15–6 torr and currents of 5–40 mA/cm^2. In the approach using the PIC–MC technique, we used the fast numerical code developed in [28].

The electron motion was described by a time-dependent equation for the distribution function $F(\mathbf{v}, r, t)$ in one-dimensional coordinate space and three-dimensional momentum space [see Eq. (1) in Part I of this paper]. Here, r is the radial coordinate and $\mathbf{v} = (v_r, v_\varphi, v_z)$ is the velocity. The electric field was assumed to have radial and axial coordinates only: $\mathbf{E} = (E_r, 0, E_z)$. The radial density profiles of positive and negative ions were determined from the continuity equation in which a diffusion–drift model was used to describe positive- and negative-ion flows [5, 27]. The densities of active particles were obtained from experimental data. The set of equations was closed by Poisson's equation for the radial component of the electric field. The axial component E_z of the electric field was assumed to be independent of r; consequently, its value could be found from the condition that the total axial current is equal to that measured experimentally.

The importance of the nonlocal character of the EEDF in the plasma of O_2 is demonstrated in Part I of this paper, where, by comparing the experiment with the MC calculations, we analyze the applicability of the two-term approximation to the solution of the coordinate-dependent Boltzmann equation. It is shown that the two-term approximation correctly takes into account the effects associated with the nonlocal character of the EEDF in the range of plasma parameters where the anisotropy of the EEDF is still relatively small. However, for sufficiently small values of the parameter RN (where R is the tube radius and N is the neutral density at the axis of the positive column) and a relatively high reduced electric field ($RN < 10^{16}$ cm^{-2} and $E/N > 150$ Td), only rigorous approaches to calculating the EEDF (such as the PIC–MC method) permit one to accurately take into account the spatial inhomogeneity of the EEDF and, consequently, the atom emission intensity. Thus, the use of the PIC–MC technique is well justified for pressures below 0.5 torr (see Fig. 3).

In addition to the effects associated with the nonlocal character of the EEDF, a correct description of the electron kinetics in a pure oxygen plasma requires a self-consistent description of the ion–molecule kinetics, which strongly affects the EEDF through the redistribution of the electric field in the plasma due to nonequilibrium ion diffusion and detachment from negative ions [4, 5, 29, 30, 32, 33]. The importance of taking into account the ion kinetics in the accurate description of the EEDF and the large role of nonequilibrium heating of ions by the longitudinal electric field were demonstrated in [4, 5]. Figure 3 shows the experimentally measured and calculated reduced electric fields in the center of the positive column of a dc discharge in pure oxygen as functions of the parameter RN. Calculations were carried out with and without taking into account both detachment from oxygen atoms and singlet oxygen molecules and ion diffusion due to nonequilibrium heating of plasma ions. From a comparison with the experiment, it is evident that detachment and nonequilibrium ion diffusion significantly affect the value of the electric field in the discharge, thus also affecting the excitation coefficients of atoms and molecules (especially the excitation of higher levels). However, these processes (first of all, ion heating by the longitudinal electric field) also change the radial density profiles of charged particles. In [5], from a comparison of the calculated and measured radial profiles of the negative-ion density by the laser-detachment technique, it was found that nonequilibrium ion diffusion significantly affects the density profile of negative ions. This leads to the

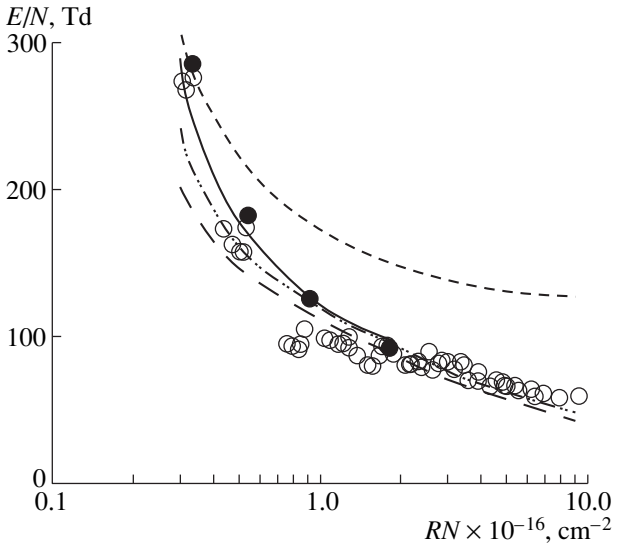

Fig. 3. Reduced electric field at the axis of a dc discharge in pure O_2 as a function of the parameter RN, where R is the tube radius and N is the gas density at the discharge axis. Open circles show the experimental data in the current range 10–30 mA/cm^2. Closed circles show the experimental data for $J = 5$ mA/cm^2. The solid curve corresponds to calculation by the PIC–MC technique taking into account detachment and nonequilibrium ion diffusion. The dashed-and-dotted curve corresponds to the EEDF calculated using the two-term approximation for solving the coordinate-dependent Boltzmann equation. The dashed curve corresponds to the latter calculation, but without taking into account ion heating in an external electric field. The dotted curve corresponds to the same calculation, but without taking into account the detachment from negative ions and nonequilibrium ion diffusion. All of the calculations were performed for a current density of 5 mA/cm^2.

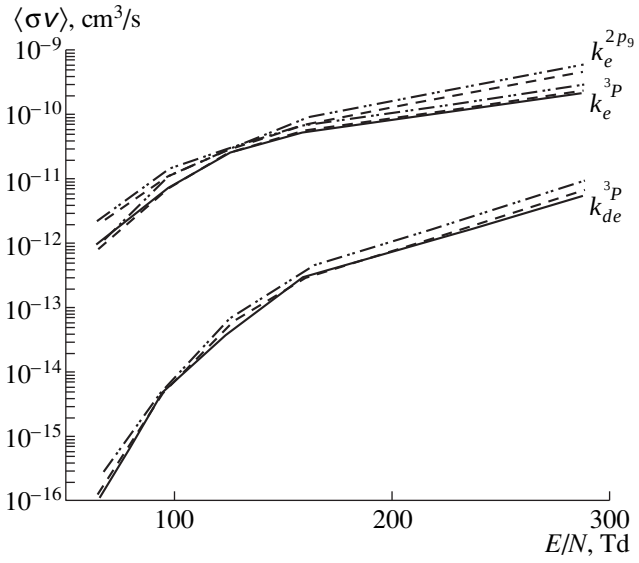

Fig. 4. Averaged (over the discharge tube cross section) rate constants $k_e^{^3P}$, $k_e^{2p_9}$, and $k_{de}^{^3P}$ for direct electron-impact excitation of O($3p^3P$) and Ar($2p_9$) atoms and dissociative excitation of O($3p^3P$) atoms, respectively, as functions of the reduced electric field. The solid curves show the rate constants calculated by the PIC–MC technique. The dashed curves show the rate constants calculated from the EEDF with the use of the two-term approximation for solving the coordinate-dependent Boltzmann equation. The dashed-and-dotted curves correspond to the rate constants obtained from the EEDF calculated using the "local" (coordinate-independent) approximation for solving the Boltzmann equation.

spatial redistribution of the field in the plasma and, consequently, the emission intensity.

Figure 4 illustrates the averaged (over the discharge tube cross section) rate constants $k_e^{^3P}$, $k_e^{2p_9}$, and $k_{de}^{^3P}$ for the direct electron-impact excitation of O($3p^3P$) and Ar($2p_9$) atoms and dissociative excitation of O($3p^3P$) atoms, respectively, as functions of the reduced electric field. The solid curves show the rate constants obtained from the EEDFs calculated by the MC technique, the dashed curves show the rate constants calculated from the EEDFs using the two-term approximation, and the dashed-and-dotted curves correspond to the rate constants obtained from the EEDFs calculated using the local approximation.

The study of the process of establishing the steady-state oxygen atom concentration by modulating the discharge current with the use of the actinometric technique allowed us to determine how the contribution from dissociative excitation to the actinometric signal depends on the discharge parameters. By virtue of the fact that the contribution to the emission intensity related to the transition O($3p^3P - 3p^3S$) comes from the direct electron-impact excitation of O atoms (11) and the dissociative excitation of O_2 molecules (14), the characteristic times of these processes are determined by the time it takes for the steady-state hydrogen-atom and electron densities, respectively, to be established. The contribution from each of these processes can be derived from the emission intensity of oxygen atoms. Figure 5 shows the typical time behavior of the ratio between the emission intensities at wavelengths of 844.6 and 811.5 nm (I_{844}/I_{811}) in the course of discharge-current modulation. It is clearly seen that there are two components in the signal. The first component varies synchronously with the current modulation and produces a certain constant level of the signal. This component is associated with the dissociative excitation of oxygen molecules. The second component varies much more slowly and has a characteristic time on the order of several milliseconds. This component can be associated with the direct excitation of oxygen atoms; thus, it reflects the time evolution of their density. From a comparison of these two components in the modulated signal, we could determine the contribution from processes (11) and (14) to the total intensity of the 844.6-nm line.

4. DISCUSSION

It is seen from Fig. 4 that taking into account the nonlocal character of the EEDF can lead to a significant change even in the averaged (over the cross section of the tube) values of the excitation rate constants for the atomic and molecular levels. This effect is more pronounced near the tube wall. It is obvious that, for the higher states of oxygen and argon atoms, this effect is more significant at higher values of the reduced electric field, i.e., at lower pressures ($RN < 10^{16}$ cm^{-2}). As follows from (7) and (8) or (17) and (18), the actinometric technique does not use the electronic excitation rate constants, but their ratio instead. Figure 6 shows the ratios of the rate constants $k_e^{2p_9}/k_e^{^3P}$ and $k_{de}^{^3P}/k_e^{^3P}$ calculated using the above approaches to solving the Boltzmann equation: the two-term approximation and the PIC–MC technique. It is seen that, although the calculated values of the rate constants $k_e^{^3P}$, $k_e^{2p_9}$, and $k_{de}^{^3P}$ depend on the accuracy with which the effect of spatial inhomogeneity on the electron kinetics in the discharge is described, their ratio does not need such a detailed analysis even in the region where the EEDF has a strongly nonlocal character (in the case at hand, at higher values of E/N corresponding to lower pressures). This is the reason why the actinometric technique has been successfully used in discharges of different configurations and over a wide range of discharge parameters. Figure 6 also shows the values of the ratio $k_{de}^{^3P}/k_e^{^3P}$ derived from the contribution of the dissociative excitation to the intensity of the 844.6-nm line in the experiments with discharge current modulation. It is seen that

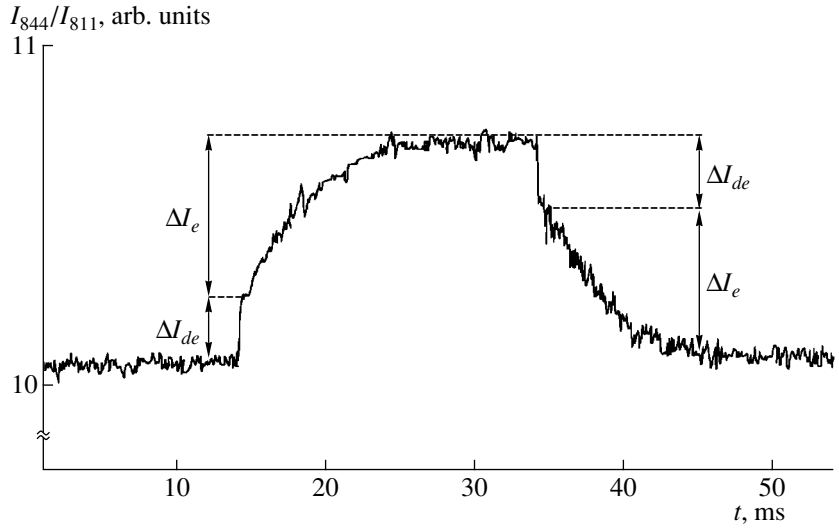

Fig. 5. Time behavior of the ratio between the emission intensities at wavelengths of 844.6 and 811.5 nm (I_{844}/I_{811}) in the course of the discharge current modulation; ΔI_{de} and ΔI_e denote the fractions of the emission intensity related to dissociative and electron-impact excitation of $O(3p^3P)$, respectively. The degree of oxygen dissociation is $\frac{[O]}{[O_2]} = D_{^3P}^{2p_9}\frac{I_{844}}{I_{811}}\frac{\Delta I_e}{\Delta I_{844}}$.

the experimental values of $k_{de}^{^3P}/k_e^{^3P}$ lie nearly one-half lower than the calculated curve. A plausible explanation of this fact will be given below.

Figure 7 shows the degree of dissociation $[O]/[O_2]$ as a function of the discharge current J for different pressures; the curves are calculated using expressions (17) and (18) and the experimentally measured intensity ratio I_{844}/I_{811}. It is seen that the degree of dissociation increases with increasing both the pressure and discharge current. The increase in $[O]/[O_2]$ with increasing the discharge current is caused by an increase in the dissociation rate, which, in turn, is caused primarily by an increase in the electron density. An increase in $[O]/[O_2]$ with increasing pressure (which was also observed in [22]) can be only be explained by a decrease in the loss rate of O atoms, because the rate constants of electron-impact dissociation decrease as the pressure increases (i.e., as the reduced electric field E/N decreases). Since the recombination of oxygen atoms on the tube wall is the main process leading to their loss under these conditions [34], it is reasonable to assume that the probability of the recombination of O atoms on the surface of the discharge tube increases with decreasing pressure. A similar result was obtained experimentally in [35] when the loss of O atoms on Pyrex was studied by the resonant UV absorption technique. Therefore, the oxygen atom density in a low-pressure discharge (and, consequently, the structure of the discharge, because the balance of charged particles is governed by detachment processes, among which the detachment from O atoms is one of the main processes) is determined by the loss of O atoms on the discharge chamber wall. Since this loss depends on many factors (e.g., the chamber material and the methods for processing and cleaning the chamber wall surface), it is possible to obtain different discharge structures for different coatings of the discharge chamber wall at the same discharge parameters, which is of scientific and practical interest.

Note that, as the pressure decreases (i.e., E/N increases), the obtained degree of dissociation $[O]/[O_2]$ does not vanish at $J \longrightarrow 0$, but approaches a certain negative value. Presumably, this is due to the fact that the calculated contribution of dissociative excitation to the emission intensity of oxygen atoms I_{844} is somewhat overestimated. This is also evidenced by the data represented in Fig. 6. As a plausible explanation of such an "artefact," we can suggest that either the dissociative excitation cross section is incorrectly evaluated or the EEDF is incorrectly described near the threshold (in the energy range of 16–20 eV). In principle, both situations are possible. In a low-pressure glow discharge, when recombination on the tube wall is the dominating electron-loss process, the EEDF at electron energies higher than the ionization energy of the gas (12.06 eV for O_2 molecules) is determined by the value of the wall potential [36], which is a very complicated function of the plasma parameters and boundary conditions. An accurate description of the electron loss on the wall is a rather complicated problem calling for knowledge of the coefficients of loss and reflection of electrons from the wall material; moreover, these coefficients may depend on the state of this surface. At low pressures, when the kinetic regime of electron loss is realized, we should know the differential loss and reflection coefficients. Note that, with the set of cross sections normal-

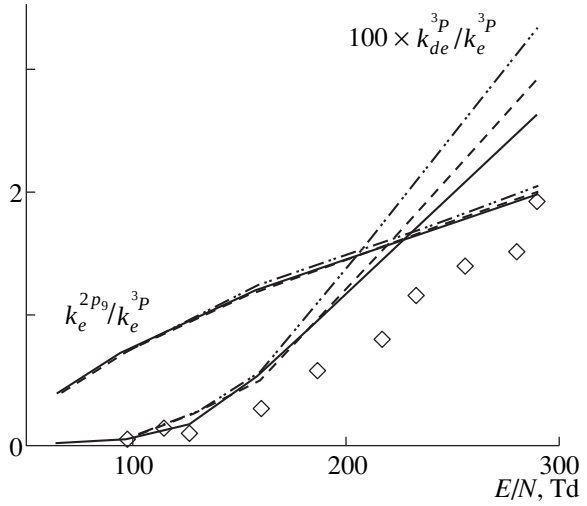

Fig. 6. Ratios of the rate constants $k_e^{2p_9}/k_e^{^3P}$ and $k_{de}^{^3P}/k_e^{^3P}$ (the ratio $k_{de}^{^3P}/k_e^{^3P}$ is increased by a factor of 100) calculated using the PIC–MC technique (solid curves) and the two-term approximation (dashed curves) for solving the coordinate-dependent Boltzmann equation. The dashed-and-dotted curves show the results obtained using the "local" (coordinate-independent) approximation for solving the Boltzmann equation. Symbols show the ratio $k_{de}^{^3P}/k_e^{^3P}$ obtained from the current-modulation experiments: $\dfrac{k_{de}^{^3P}}{k_e^{^3P}} = D_{^3P}^{2p_9}\dfrac{I_{844}}{I_{811}}\dfrac{\Delta I_{de}}{\Delta I_{844}}$.

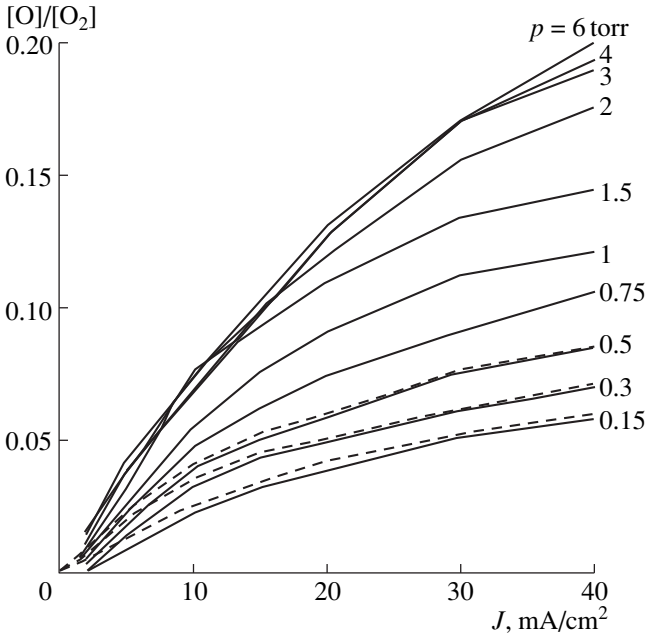

Fig. 7. Degree of dissociation $[O]/[O_2]$ as a function of the discharge current for different pressures. The curves are calculated using expressions (17) and (18) and the experimentally measured intensity ratio I_{844}/I_{811}. The dashed curves show the results of calculations for pressures 0.15, 0.3, and 0.5 torr for the dissociative-excitation threshold energy [process (14)]shifted by 2 eV toward higher energies. For pressures above 0.75 torr, the contribution from dissociative excitation is negligibly small and the dashed and solid curves coincide.

ized to transport coefficients (in particular, to the ionization coefficient for O_2), the self-consistent calculation by the PIC–MC technique yields a value of the reduced electric field close to that observed experimentally at a given discharge current. This means that the calculated EEDF is also close to the real distribution function. However, this assertion is true only in the case of an absolutely precise description of the ion kinetics. In our calculations, the ions were described in the hydrodynamic approximation. However, as the pressure decreases below 1 torr, this approximation is no longer sufficiently accurate in the region of the wall potential jump because the ion mean free path becomes comparable with the size of this region. The hydrodynamic approximation overestimates the ion flow toward the wall, thereby overestimating the wall potential and the high-energy part of the EEDF. The latter, in turn, leads to overestimating the calculated excitation coefficients for higher levels of atoms and molecules in comparison with the experiment, which is reflected in Fig. 6.

It should be noted that reliable experimental data on the dissociative excitation cross section for $O(3p^3P)$ in the near-threshold region are still lacking. Usually, the adiabatic energy of the dissociation products $O(3p^3P) + O$ equal to ~16 eV is taken as the threshold energy for this process, but the actual threshold energy may be different because of the relative positions of the ground and excited terms of O_2 molecules (which, however, is not definitely established in experiments). In principle, the positions of the terms of O_2^* molecules in the energy range of 16–19 eV permit the existence of a certain threshold. For this reason, to avoid the above "artefact" in the *J*-profiles of the degree of dissociation $[O]/[O_2]$, the threshold energy for process (14) of dissociative excitation of $O(3p^3P)$ atoms was increased by ~2 eV. This allowed us to decrease the contribution of this process at high values of the parameter *E*/*N* by a factor of about 2 and to achieve satisfactory agreement between the calculated and experimental values of the ratio $k_{de}^{^3P}/k_e^{^3P}$. The results of calculations of $[O]/[O_2]$ for this case are shown by the dashed curves in Fig. 7. It is seen that the decrease in the dissociative excitation rate by shifting the threshold energy for this process toward higher energies leads to a physically reasonable behavior of the dependence of the degree of oxygen dissociation on the discharge current at low pressures: $[O]/[O_2] \longrightarrow 0$ as $J \longrightarrow 0$.

Thus, along with the fact that the nonlocal character of the EEDF does not significantly influence the acti-

nometry of atomic oxygen, it is also of importance that, for $E/N < 200$ Td and a degree of oxygen dissociation higher than ~0.02, there is no need to take into account the dissociative excitation of $O(3p^3P)$ atoms when using the transition $O(3p^3P) \longrightarrow O(3p^3S)$.

5. CONCLUSION

In this paper, we have presented the results from measurements of the oxygen atom density in the positive column of a dc discharge in pure oxygen by the actinometric technique using Ar atoms. This technique and the results obtained are analyzed using two different approaches to solving the Boltzmann equation for a spatially inhomogeneous EEDF: the two-term approximation and the Monte Carlo method. Based on a detailed consideration of the processes governing the behavior of the EEDF in the discharge, the influence of both the nonlocal nature of the electron energy spectrum and the discharge kinetics on the accuracy of such measurements is examined. It is shown that the nonlocal character of the EEDF can appreciably affect the intensity of the emission lines of oxygen and argon atoms, but has little effect on the actinometric signal as compared to the case where a spatially homogeneous EEDF is used to calculate the electronic excitation coefficients for the emitting states of O and Ar atoms (the difference does not exceed 1–3%). The reason for this is that the excitation thresholds of the O* and Ar* states are close to each other and the energy profiles of the cross sections for the excitation of these states are similar in shape. The effect of the discharge kinetics is more pronounced because it significantly influences the plasma parameters. Over a wide range of parameters, the electric field in a pure O_2 discharge is determined by electron detachment from negative ions by active particles, O atoms, and metastable O_2 molecules. Therefore, because of the very sharp dependence on the field, an incorrect description of these processes leads to large errors in determining the rate constants for the atom excitation. Hence, the use of the actinometric technique for measuring the absolute concentration of oxygen atoms in the ground state requires, first of all, a very detailed description of the discharge plasmochemical kinetics and a thorough analysis of all the possible processes. It should be emphasized that applying this technique to low-pressure discharges ($RN < 10^{17}$ cm^{-2}) requires that the processes of active-particle loss on the discharge chamber wall also be considered in detail because, in this case, these processes determine the active-particle density. However, the use of the actinometric technique for monitoring the behavior of the O atom density in a plasma is justified over a wide range of reduced electric fields (up to ~200 Td) when the $O(3p^3P - 3p^3S)$ transition ($\lambda = 844.6$ nm) is used and the degree of dissociation is $[O]/[O_2] > 0.02$.

ACKNOWLEDGMENTS

This work was supported by the Russian Foundation for Basic Research, project nos. 00-15-96554 and 00-02-16508.

REFERENCES

1. M. Haverlag, A. Kono, D. Passchier, *et al.*, J. Appl. Phys. **70**, 3472 (1991).
2. N. Takada, D. Hayashi, K. Sasaki, and K. Kadota, Jpn. J. Appl. Phys. **36**, L1702 (1997).
3. H. Amemiya and K. Ogawa, J. Phys. D **30**, 879 (1997).
4. V. A. Feoktistov, V. V. Ivanov, A. M. Popov, *et al.*, J. Phys. D **30**, 423 (1997).
5. V. V. Ivanov, K. S. Klopovskiy, D. V. Lopaev, *et al.*, IEEE Trans. Plasma Sci. **27**, 1279 (1999).
6. M. Shibata, N. Nakano, and T. Makabe, J. Appl. Phys. **80**, 6142 (1996).
7. J. Amorim, J. Loureiro, G. Baravian, and M. Touzeau, J. Appl. Phys. **82**, 2795 (1997).
8. J. Amorim, G. Baravian, M. Touzeau, and J. Jolly, J. Appl. Phys. **76**, 1487 (1994).
9. D. G. Fletcher, Appl. Phys. B **60**, 61 (1995).
10. A. D. Tserepi, J. R. Dunlop, B. L. Preppernau, and T. A. Miller, J. Appl. Phys. **72**, 2638 (1992).
11. B. N. Ganguly and P. Bletzinger, J. Appl. Phys. **82**, 4772 (1997).
12. K. Miyazaki, T. Kajiwara, K. Uchino, *et al.*, J. Vac. Sci. Technol. A **14**, 125 (1996).
13. R. A. Gottcho and V. M. Donelly, J. Appl. Phys. **56**, 245 (1984).
14. L. D. B. Kiss, J.-P. Nicolai, W. T. Conner, and H. H. Sawin, J. Appl. Phys. **71**, 3186 (1992).
15. M. K. Abachev, Kh. V. Gazarov, V. A. Galperin, *et al.*, Mikroélektronika **26**, 225 (1997).
16. Y. Kawai, K. Sasaki, and K. Kadota, Jpn. J. Appl. Phys. **36**, L1261 (1997).
17. F. W. Breithbarth, E. Ducke, and H. J. Tiller, Plasma Chem. Plasma Process. **10**, 377 (1990).
18. J. P. Booth, O. Joubert, J. Pelletier, and N. Sadeghi, J. Appl. Phys. **69**, 618 (1991).
19. R. E. Walkup, K. L. Saenger, and G. S. Selwyn, J. Chem. Phys. **84**, 2668 (1986).
20. J. P. Booth and N. Sadeghi, J. Appl. Phys. **70**, 611 (1991).
21. A. Granier, D. Chereau, K. Henda, *et al.*, J. Appl. Phys. **75**, 104 (1994).
22. D. Pagnon, J. Amorim, J. Nahorny, *et al.*, J. Phys. D **28**, 1856 (1995).
23. *Handbook of Constants of Elementary Processes Involving Atoms, Ions, Electrons, and Photons*, Ed. by A. G. Zhiglinskiĭ (S.-Peterburg. Gos. Univ., St. Petersburg, 1994).
24. M. V. Malyshev and V. M. Donnelly, J. Vac. Sci. Technol. A **15**, 550 (1997).
25. J. K. Ballou, C. C. Lin, and F. E. Fajen, Phys. Rev. A **8**, 1797 (1973).
26. V. V. Ivanov, K. S. Klopovskiĭ, D. V. Lopaev, *et al.*, Pis'ma Zh. Éksp. Teor. Fiz. **63**, 511 (1996) [JETP Lett. **63**, 537 (1996)].

27. V. V. Ivanov, K. S. Klopovskiy, D. V. Lopaev, *et al.*, in *Electron Kinetics and Applications of Glow Discharges* (Plenum, New York, 1998); NATO ASI Ser., Ser. B **367**, 37 (1998).
28. V. V. Ivanov, A. M. Popov, and T. V. Rakhimova, Fiz. Plazmy **21**, 731 (1995) [Plasma Phys. Rep. **21**, 692 (1995)].
29. G. Gousset, C. M. Ferreira, M. Pinheiro, *et al.*, J. Phys. D **24**, 290 (1991).
30. V. V. Ivanov, K. S. Klopovskiy, D. V. Lopaev, *et al.*, in *Proceedings of XIII European Sectional Conference on the Atomic and Molecular Physics of Ionized Gases, Poprad (Slovakia), 1996*, Vol. 20E, Part A, p. 77.
31. P. V. Fel'tsan and I. P. Zapesochnyĭ, Ukr. Fiz. Zh. **12**, 633 (1967).
32. J. L. Jauberteau, G. J. Meeusen, M. Haverlag, *et al.*, J. Phys. D **24**, 261 (1991).
33. E. Stoffels, W. W. Stoffels, D. Vender, *et al.*, Phys. Rev. E **51**, 2425 (1995).
34. B. Gordiets, C. M. Ferreira, J. Nahorny, *et al.*, J. Phys. D **29**, 1021 (1996).
35. L. Magne, H. Coitout, G. Gernogora, and G. Gousset, J. Phys. III **3**, 1871 (1993).
36. A. A. Kudryavtsev and L. D. Tsendin, Zh. Tekh. Fiz. **69** (11), 34 (1999) [Tech. Phys. **44**, 1290 (1999)].

Translated by N. Larionova